Diego Veneziano

Hydrogen embrittlement, microcracking and piezonuclear reactions in the metal electrodes of an electrolytic cell

Tesi per il conseguimento del titolo di Dottore di Ricerca
XXVII Ciclo (2012 - 2013 - 2014)

Dottorato di Ricerca in Ingegneria delle Strutture

Politecnico di Torino
Dicembre 2014

PhD in Structural Engineering

Politecnico di Torino, Corso Duca degli Abruzzi 24, 10129 Torino, Italy

Tutors: Prof. Alberto Carpinteri, Dr. Amedeo Manuello Bertetto
Coordinator: Prof. Alberto Carpinteri

ACKNOWLEDGEMENTS

SUMMARY

Formation and propagation of fractures in solid materials are main topics in the discipline of Fracture Mechanics. The study of the propagation of fractures is also vital in Structural Mechanics as an important indicator of the level of damage of a generic structure. When focusing on metal materials, hydrogen embrittlement (HE) is one of the most relevant factors making the material itself more sensitive to propagation of cracks. This is a remarkable issue also in metallurgic processes. Moreover, any environment rich in hydrogen is a risk for the metal: for instance, either electrolytic environments or any situation that leads to an increment in both cathodic and anodic polarizations. The effect of HE reduces the threshold stress intensity factor as free Hydrogen (H) atoms hosted in the metal lattice cause the solid to become more brittle and less resistant to crack formation and propagation. As regards to Ni- and Fe-based alloys, H absorption into the crack tip fracture process zone increases the stress intensity and the crack growth rate.

The knowledge of such features is the key to study the topics reported in this thesis. In fact, the first part of Chapter 1 will describe useful details about HE. The aim of this work is to investigate the mechanical features involved in crack propagation and arguing in what terms they are connected to nuclear effects observed during compression experiments and other failure phenomena involved in electrolysis. The second part of Chapter 1 reports some literature of experimental results about nuclear emissions detected during compression tests on brittle rocks, carried out in the Fracture Mechanics Laboratory at the Department of Structural, Geotechnical and Building Engineering (DISEG) of the Politecnico di Torino (Turin, Italy). From the experimental data collected and the nuclear emissions detected a hypothesis of piezonuclear fission reactions is drawn. Such would be the idea of specific nuclear reactions triggered by stress relief caused by cracks and fractures in the material under compression. Results of chemical composition analyses on external and fractured surfaces of the specimens are reported. Comparing the proportions of the chemical changes measured on the specimens to the evolution of the abundance of the Earth Crust elements, a connection between the laboratory scale and the Earth scale is presented. From a

different perspective, the piezonuclear effect could be interpreted as an original experimental proof of nuclear reactions induced in solid materials through mechanical processes. Features like this one are studied in the research field of Nuclear Science of condensed matter, also known as cold fusion research. That is, nuclear reactions are induced by means of processes involving relatively low energy, such as chemical electrolysis.

In Chapter 2, part of the literature concerning nuclear effects in condensed matter is presented. Various experimental data indicating the occurrence of anomalous nuclear reactions at relatively low energies are mentioned. Accordingly, the author of this thesis followed a two-year laboratory campaign, investigating possible nuclear effects occurring during electrolysis experiments.

Chapter 3 and 4 describe the experimental activity carried out using an electrolytic cell with different metal electrodes. In details, Chapter 3 describes the laboratory experiments conducted on nickel-iron anode and cobalt-chromium cathode. Chapter 4 reports details of the second part of the laboratory campaign: nickel anode and palladium cathode were used. The set-up of the laboratory rig is described as well as the equipment for the measurements. The measures were taken focusing on alpha particle and neutron emission, as well as on the chemical composition of the electrodes before and after the electrolysis. The appearance of micro-cracks on the surface of nickel and palladium electrodes is one of the key aspects observed after the experiments. After illustrating the results of the laboratory research, a strict connection between micro-cracks, neutron emission and compositional changes is considered as the evidence of non-traditional nuclear reactions implicating the fission of nickel and palladium into lighter elements. Numerous are the hypotheses behind the jungle of experimental data in the literature, nonetheless, a unified theory has not been established yet.

In the attempt of providing a contribution to the theoretical explanation, Chapter 5 focuses the attention on describing the nucleus of an atom through a lattice model. The model described in this chapter was proposed by Professor Norman D. Cook of the Kansai University (Osaka, Japan). In the latter the author of the thesis spent five months of his PhD course to study and broaden his knowledge of the model itself. Also numerical simulations are reported

considering the fission of different lattices corresponding to different elements. The results of the simulations provide a first attempt to predict what fragments would form from the geometrical rupture of the nuclear lattices investigated: that is iron, nickel, and palladium. Such prediction might be in support of the experimental activity related to fracture and electrochemical processes, when trying to reproduce nuclear effects in condensed matter.

This thesis intends to pose a closure to the research developed in a three year PhD course; thus, the conclusions outlined at the end are drawn under the light of what has been experienced by the author in the past three years. On the other hand, one of the purposes of what is written below is to provide the support to any further research intended to be developed in the field of Fracture Mechanics and Nuclear Science of Condensed Matter. For this reason a plausible mechanical interpretation to nuclear-like effects observed in fracture and electrolysis processes is considered.

X

CONTENTS

FIGURES AND TABLES

CHAPTER 1

1 INTRODUCTION

The work and the topics proposed in this thesis are to be considered in the context of Structure Mechanics and in particular in Fracture Mechanics. The research here developed finds its roots in the experimental work of professor Carpinteri and his research team [1]. Curious and interesting results came out from simple compression experiments carried out on natural rock specimens. They confirmed an energy release during the fracture, involving different forms of energies. In other words the fracture energy dissipated on the surface of a crack is not the only one involved in the process of crack formation and propagation. In fact, there is a release of energy due to the propagation of elastic waves, thus acoustic emissions (AE) and a release of electrons, thus electromagnetic emissions (EME). Most surprising is the release of neutrons detected from the specimen during the process of fracturing. The team of researchers, well aware of the very complex nature of fracturing and cracking processes, had to face a new aspect they have never considered before in their "milieu": nuclear effects were studied in structural mechanics or in general in civil engineering. It is a very difficult path trying to study diverse effects that belong to worlds of such a big scale difference. The study of the mechanics of solids and nuclear science come together to a multifaceted science: the nuclear science of condensed matter. It is about the study of nuclear effects in materials in their ordinary solid state. Also it is about studying how to induce nuclear effects without involving inaccessible energies: here the chemistry comes to assist. Thus numerous cases can be found in the literature of scientist attempting to reproduce nuclear effects by means of electrochemical processes.

1.1 Scope of the thesis

The previous paragraph was a brief introduction to the origin of the research developed in this thesis. The present chapter includes a description of the HE effects in different environments. It also provides a detailed description of the compression tests carried out in the Laboratory of Fracture Mechanics at Politecnico di Torino focusing on the results of neutron emission detection and chemical analysis of both the undamaged and cracked surfaces of the specimens

by means of the Energy Dispersive X-ray Spectroscopy (EDX) technique. The following chapter will provide the reader with an historical description of the literature of the most remarkable facts related to the "Cold Fusion" research. Such knowledge is essential in order to establish a connection between two worlds of different scale and characterized by very different approaches: Fracture Mechanics and Nuclear Science. This thesis aims to provide useful information and experimental data that could contribute to achieve a common answer to the many questions concerning cold fusion. In the following, it is proposed to study particular phenomena, say nuclear, from a different perspective and through a different approach. The research presented here in these pages find its roots in an experimental milieu and it is approached through a methodology that strongly depends on the author background. The perspective is that of the Structural Mechanics environment that comes to face the reality of a deep connection between scales of different order of magnitude: there is a relationship between what is labelled as "macro" or "meso" and what is as "micro" or "nano".

1.2   Fracture propagation and hydrogen embrittlement

In case of formation or propagation of microcracks, dynamic effects in the form of longitudinal waves of expansion and contraction (tension and compression) occur in addition to transverse or shear waves. Generally known as pressure waves, they travel at a speed strictly related to the medium: that is, for most of the solids and fluids the order of magnitude is 10^3 meters per second. The wavelength appears to be of the same order of magnitude of crack size or crack advancement length. Therefore, the wavelength of the pressure waves cannot exceed the maximum size of the body in which the crack is contained. In actual fact, it may vary from the nanometer scale up to the kilometer one, whether defects of a crystal lattice such as dislocations or vacancies are considered, or rather tectonic faults of the Earth's crust. Hence, considering the well-known relationship between frequency, speed and wavelength, nanocracks would involve a pressure wave frequency of 10^{12} oscillations per second (TeraHertz), while large scale tectonic dynamics implies frequencies of just some oscillations per second (Hertz) [2] [3].

Although the research of this thesis draws its roots from a study of rocky natural materials, interesting phenomena related to the propagation of fracture in metal material will be also considered. For the sake of understanding the features studied in this thesis, it is crucial to be aware of one of the most important phenomena that favor the propagation of fracture in metals. Such process, well-

known in Metallurgy and Fracture Mechanics, characterizes metals during forming or finishing operations [4]. During such activities the unintentional introduction of hydrogen into the metal is often likely to occur. Hydrogen effects are largely studied especially in metal alloys, where the presence of H free atoms in the host lattice causes the metal to become more brittle and less resistant to crack formation and propagation. In particular, hydrogen generates an internal stress that increases the fracture stress of the metal so that brittle crack growth can occur under a hydrogen partial pressure below 1 atm [5].

Hydrogen presence is known to assist cracking according to numerous phenomena: such as stress corrosion cracking SCC, hydrogen-environment-assisted cracking HEAC, internal hydrogen-assisted cracking IHAC, hydrogen-enhanced decohesion HEDE, etc. The mechanisms and parameters involved in such processes are numerous. What all the mechanisms of crack growth have in common is that they are localized at the crack tip. It is not always necessary for the entire material to become embrittled, even though hydrogen is often generated as a product of the crack tip corrosion reaction and crack growth may occur in correspondence of a HE process [5].

There are three important types of conditions for SCC to occur: electrochemical, mechanical, and chemical. Furthermore, it is known that, for metal alloys in high temperature water, the formation of oxides rich in Chromium (Cr) also allows, by hydrolysis reactions, to obtain high hydrogen fugacity at the crack tip, which make hydrogen-assisted cracking (HAC) mechanisms viable [5].

Slip dissolution is another phenomenon connected to HAC. This mechanism depends on chemical and physical factors such as oxide rupture, passivation, and liquid diffusion rates. They are very important, as they affect the charge transfer per unit time in the slip dissolution model and the hydrogen adsorbed atom coverage and hydrogen evolution rate in hydrogen-assisted cracking [5]. In particular, the oxide rupture plays a fundamental role in hydrogen-assisted cracking models, since it directly helps hydrogen entry into the metal. Unfortunately there is lack of quantitative knowledge of events such as hydrogen coverage at the crack tip, hydrogen diffusion ahead of the crack, preventing us to obtain a full comprehension on the matter [5].

The oldest of the HE mechanisms is the hydrogen-enhanced decohesion (HEDE) mechanism, which proposes that high, localized concentration of hydrogen can weaken the interatomic cohesive forces at or ahead of crack tips [5]. According to this mechanism hydrogen is thought to accumulate in regions of high triaxial stress ahead of the crack tip at a distance about twice the crack tip opening

displacement (CTOP). Moreover, high concentration of hydrogen can form also within a few atomic distances of crack tip or at several tens of nanometers ahead of the crack, where dislocation shielding effects result in higher stress. As the bond between metal atoms can be weakened by hydrogen effects on electron-charge density, crack growth can then occur along cleavage planes or along grain boundaries, weakened by segregation of metalloid impurities or by segregation of particle-matrix interfaces.

With particular attention to metal alloys, we would like to focus on Nickel-based environment. Although, nickel and nickel-based alloys are generally resistant to SCC, crack growth can occur in particular conditions. For instance, in high temperature water and gaseous hydrogen environment cracking is predominantly intergranular [6]. Having said this, it is important to emphasize that hydrogen uptake may occur in nickel-based alloys and, therefore, crack growth is possible. Also, hydrogen-assisted crack growth has been observed at ambient temperature up to ~100 °C in a number of hydrogen charging conditions [5].

Both nickel-based and iron-based superalloys are prone to severe hydrogen cracking. This was revealed by initial studies of the effects of exposure to high pressure H_2 on metals and by later research on H-assisted cracking in nickel alloys [7]. Additionally, ensuing results have shown that Fe-based alloys are susceptible to both IHAC and HEAC in high-pressure H_2 [5]. The tensile yield strengths of the materials, examined with regard to H cracking, are in the range from 800 MPa to 1100 MPa; however, yield strengths approaching 1400 MPa are possible. Hydrogen-free superalloys crack by microvoid processes at high K_{IC}, but IHAC and HEAC progress by a mixture of intergranular separation and transgranular cracking [4]. It is important to understand that each cracking mode depends on different variables, such as metallurgical factors, grain size, H concentration, temperature, CMOD-control mode. For instance, in some Fe-based alloys it has been proven that if H is introduced to the crack tip zone process, the stress intensity for H cracking is substantially reduced [8]. In other words, K_{IC} changes to a specific K_{IC-H} due to predissolved H interacting with the rising CMOD. This is also valid for both IHAC and HEAC in Ni-based superalloys [9].

With particular focus on IHAC, one of the most important chemical variables when studying the HE related phenomena is the hydrogen concentration in the material. Hydrogen is known to be trapped at various microstructural features in a complex alloy. Also, high tensile strength and H trapping are correlated because nanoscale features that strengthen an alloy might also provide sites for H segregation. Thus, the concentration of H, predissolved in a high-strength alloy

microstructure, critically affects the threshold stress intensity. In particular H concentration is defined either as total H concentration C_{H-TOT} or diffusible H concentration C_{H-DIFF} [5] [10]. The former is the sum of (i) H dissolved in the alloy lattice, (ii) H in dynamic equilibrium with one or more reversible trap states and (iii) H strongly trapped in irreversible sites. C_{H-DIFF} depends on temperature exponentially through the energies of H-lattice solution H_S and H-trap binding E_B [11]. Numerous studies show that K_{IIHAC} increases as C_{H-TOT} increases for low-alloy steels [5].

In relationship with the experimental activity concerning electrolytic cells, it is important to investigate what roles electrolytic and gaseous environments play. For both gases and electrolytic solutions, we must consider that the amount of atomic hydrogen absorbed on crack surfaces close to the tip affects HEAC as much as the predissolved H concentration does to IHAC. In gaseous environment, it is proven that increasing H_2 pressure promotes HEAC, thus, the stress intensity factor increases while the crack growth rate rises [5].

In electrolytes, cathodic polarization, decreasing pH and temperature variations have deleterious effects on high-strength alloys. Moreover, all the aqueous environmental conditions that favour increased H production and absorption into the crack tip fracture process zone increases the stress intensity factor and increase the crack growth rate.

One of the worst mechanisms in electrolytes is related to the effect of applied electrode potential. In particular, for HEAC in high-strength alloys, such as steel, the stress intensity factor increases with both increasing cathodic and anodic polarization resulting in a decrease of the resistance to cracking [5] [12]. As mentioned in the previous section, accounting for hydrogen concentration, temperature, electrolytic environments and cathodic polarization effects represents a very important requirement for investigating and interpreting the results of the experimental campaign described in chapter four and five.

1.3 Energy release from fracture processes: acoustic, electromagnetic, nuclear

When a solid material with specific boundary conditions is under compression or subjected to external forces strong enough to produce cracks, the failure process occurs. It is known that the fracture energy is not actually distributed over the entire volume of a body; it is, instead, localized around a specific zone or stream that turns into a fracture or crack. For instance, ductile materials behave as such

when "necking" occurs [2]. Part of the strain energy accumulated is released when the crack forms and propagates. Carpinteri et al. supposed also that shock waves due to compression rupture induce particularly sharp strain localization in the solids and then material interpenetration accompanied by an analogous formation of a high-density fluid or plasma [13] [14].

It is generally known that the brittle failure phenomena occur with mechanical energy release. However, they emit additional forms of energy related to the fundamental natural forces. The literature reports that different forms of energy are emitted during compressive failure of brittle materials. Three types of emissions have been identified: acoustic, electromagnetic and neutron emissions [14]. The most common energy release is the acoustic emission AE. This is a type of phenomenon due to transient elastic waves propagating in a medium and generated by rapid release of energy from localized sources such as developing cracks. The AE mechanism is equivalent also at different scales: from the micro-crack propagating in a rock to the large scale earthquake on the Earth crust. Specifically, crack growth is accompanied by acoustic emission ultrasonic waves [15]. The AE has been for the past five years and more increasingly used in Structural Engineering for non-destructive monitoring techniques to assess the damage progression. Monitoring structures by means of the AE technique proves possible to detect the occurrence of stress-induced cracks. This is possible thanks to transducers applied to the surface of structural elements. The transducers exploit the capability of certain crystals to produce electric signals whenever they are subjected to a mechanical stress. The damage of a structure is assessed by considering that the released energy is proportional to the number of AE events detected during the monitoring. In details, for a given specimen r, known its volume V, it is possible to calculate the critical number of acoustic emission N_{max} that the structure is able to bear before reaching the critical condition according to the equation $N_{\max} = N_{\max r} \left(V/V_r \right)^{D/3}$; D is a fractal exponent comprised between 2 and 3, that accounts for a size-scaling effect [15]. Investigating brittle materials, the AE technique allows one to characterize fracture and damage growth through the *b*-value of the Gutenberg-Richter law. This parameter is based on a statistical model and can be related to the value of the exponent of the power-law distribution of the crack size in a damaged medium. The b-value changes systematically during the evolution of the failure process and allowing to identify the modalities of energy dissipation in a structural element. The extreme cases of the b-value correspond respectively to D=3 (b=1.5) and D=2 (b=1) [14]. That is, the critical condition occurs when b is equal to 1.5 and the energy dissipates

thanks to small defects distributed throughout the structural element; on the other hand when b is equal to 1 the energy dissipates on the surface of the material. Carpinteri and his research team reported that energy release obeys a time-scaling law expressing the direct proportionality among released energy *W*, cumulative number of AE events *N* and a time parameter t^{β_t} , where β_t is a time-scaling exponent of the released energy and it is comprised between 0 and 3, edge values included [14] [16] [17]. The AE technique implies the collection of many data throughout the monitoring procedure, such as AE event counts, event magnitude and event source localization. These data are used in procedures to calculate the fractal dimension of the damage domain. Considering the size and time scaling laws and the data drawn from the monitoring it is possible to use the β_t parameters to predict critical conditions, while the *b*-values can be used to describe the damage level.

As mentioned above, crack growth is accompanied by electromagnetic emission also referred to as EME. This is due to the electric charge redistribution when the material failure occurs. Thus, moving charges produce a magnetic field. In 2010, Carpinteri, Lacidogna et al. reported that during compression tests on different brittle materials, they measured magnetic fields with a frequency range from 10 Hz to 400 kHz. The EME was investigated by means of an isotropic probe calibrated *ad hoc* with a measurement capability range comprised between 1nT and 80mT. It is interesting that in all specimens tested EME was detected only when sharp drops in stress occurred. The tests were carried out in displacement control conditions with a constant rate of displacement since, during the loading process, the stress sharply drops when there is a rapid decay of the material mechanical properties due to formation of new micro-cracks. In general, the mode of energy release, say AE, EME, etc. of a specimen in compression depends on its intrinsic brittleness, dimensions and slenderness [18] [19]. Carpinteri and his collaborators found that remarkably AE behaves as fracture precursor since it precedes EME followed by stress drops related to fracture propagation [14].

The neutron emission (NE), on the other hand, was for the first time associated to fracture phenomena investigated in compression tests by Carpinteri et al. [1]. Analogous NE was found by Cardone et al in experiments with fluids subjected to cavitation [20]. It is worth considering the analogy between experiments carried out by Cardone and those conducted by Carpinteri. For what concerns the compression tests on rock specimens, as mentioned before, pressure waves propagating in the solid material are caused by particularly brittle fracture events during the loading process. Nevertheless, in cavitation experiments, an external

source of ultrasounds is the cause of the process inducing the implosion of bubbles. The NE detected during experiments conducted both on liquids and solids were named piezonuclear since they appeared to be strictly related to pressure waves propagation, thus to the mechanical cause behind the catastrophic events observed in cavitation and in fracture formation. It is necessary to state that a worldwide accepted theoretical explanation does not exist and what is provided here is only one of many plausible interpretations that is under research and might provide directions for future work.

1.4 Evidence of neutron emission related to fracture phenomena: from the laboratory to the earth crust scale

In the Fracture Mechanics Laboratory of the department of Structural, Building and Geological Engineering of Politecnico di Torino (Turin, Italy) uniaxial compression tests on different materials have been carried out by Carpinteri et al. investigating the relationship between the characteristics of the specimens and the neutron emission detected [1] [14]. Specimens of different materials such as concrete, Syracuse limestone, Carrara marble, and Green Luserna granite were crushed. NE was detected by means of helium-3 neutron detector and bubble dosimeter detectors [21].

It is worth spending a paragraph to describe the measurement equipment used for the detection of neutrons. Since a neutron is a particle with no electrical charge it does not produce direct ionization in a detector. Therefore, neutron detectors rely upon a conversion process where an incident neutron interacts with a nucleus to produce a secondary charged particle. Such particle is then detected providing the information necessary to deduce the neutron presence. The ^{3}He type (Xeram, France) detector used has electronics of pre-amplification, amplification and discrimination directly connected to the tube containing the gas. It is powered by a high voltage power supply of about 1.3 kV through a module known as Nuclear Instrument Module (NIM). The logic output of the detector is connected to the NIM, produces transistor-transistor logic (TTL) pulses and is enabled for analog signals exceeding 300 mV. Such threshold is due to the sensitivity of the detector to gamma rays ensuing NE in ordinary nuclear processes and it is determined measuring the analog signal of the detector exposed to a Co-60 source of gamma radiation. The detector is calibrated for measuring thermal neutrons with a sensitivity of 65 counts per second per thermal neutron *cps/$n_{thermal}$* (±10% declared by the factory); that is, a flux of 1 *thermal neutron/s·cm^2* corresponds to a count

rate of 65 *cps*.

The bubble detectors are a set of passive neutron dosimeters insensitive to electromagnetic noise and with no gamma sensitivity. They are based on superheated bubble detectors (Bubble Technology Industries BTI, ON, Canada) calibrated at the factory with an Americium-Beryllium source [22] [23]. They provide instant visible detection and measurement of the dose of neutron. Each detector is composed of a polycarbonate vial filled with an elastic tissue equivalent polymer, where droplets of a superheated Freon gas are dispersed. When a neutron hits a droplet, the latter immediately vaporizes forming a visible gas bubble trapped in the gel. The number of visible bubbles provides a direct measure of the equivalent neutron dose with an efficiency of about 20%. By means of these dosimeters the dose of both thermal and fast neutrons can be measured. In particular BDT type detectors are suitable for thermal neutrons (energy E=0.025 *eV*), while BD-PND type ones are suitable for fast neutrons (energy E > 100 *keV*). The same types of neutron detectors described above have been used for the measurements conducted during the electrolytic experiments followed by the author and they are described in details in Chapter 4 and 5 of this thesis.

For the crushing tests, choosing specimens of different material is important because each material (e.g. granite, basalt, magnetite and marble) has different brittleness index and different composition, say different minerals or iron content. The more brittle the material is, the more catastrophic the failure of the specimen is. Additionally, the content in iron appeared to be another important feature involved in the occurrence of NE. As a matter of fact, crushing tests conducted in 2009 on marble and granite specimens showed detectable NE only during granite failure [1]. Figure 1 and Figure 2 report results of crushing tests conducted on two prismatic 6x6x10 cm^3 specimens of marble (labeled as P1 and P2 in Figure 1) and two of Luserna granite (P3 and P4 in Figure 2). For each specimen, the load (kN) versus time (min) curve is presented associated with its relevant NE measurements in terms of count rate (count per second cps) throughout each loading process. The neutron emission background level measured was equal to $3.8 \cdot 10^{-2} \pm 0.2 \cdot 10^{-2}$ cps. It is clear that only catastrophic failures, thus materials with brittle behavior (granite) are accompanied by neutron emission above the background level. Therefore, brittleness is a discriminant factor to observe NE when cracks occur.
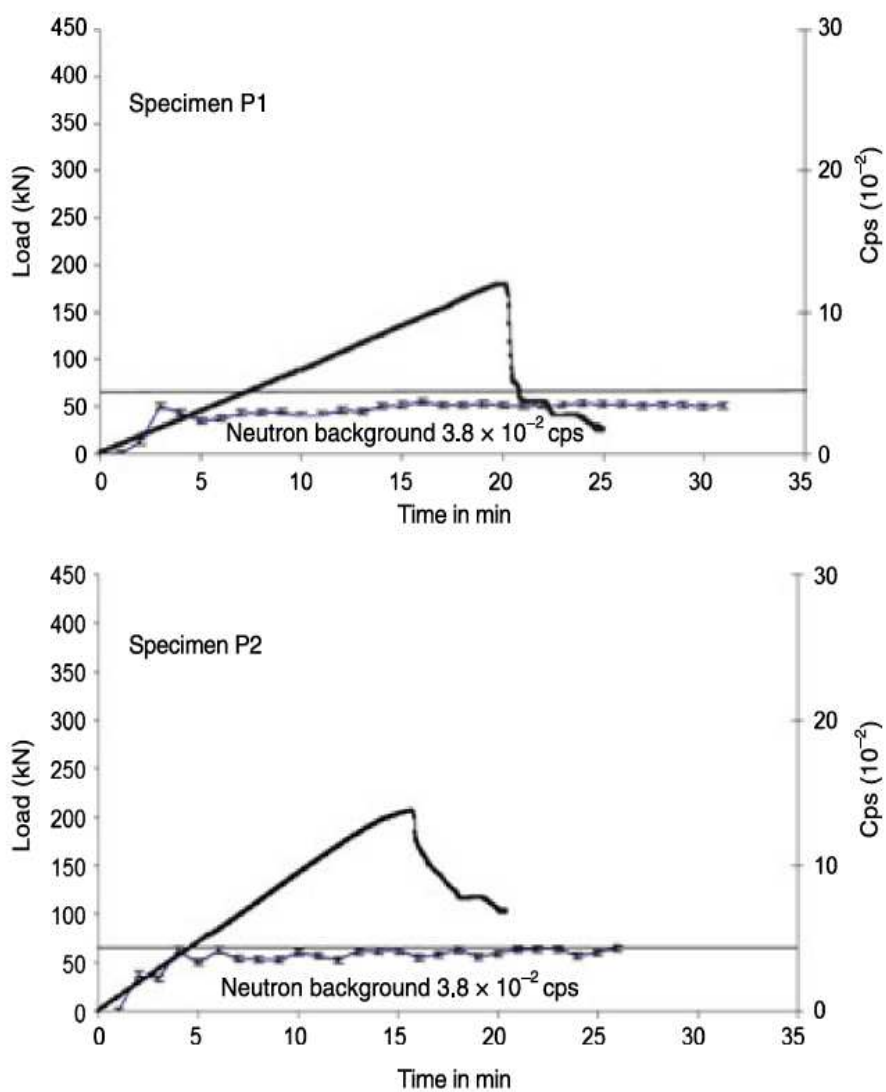
Figure 1 Carrara marble (specimens P1 and P2) crushing test results.
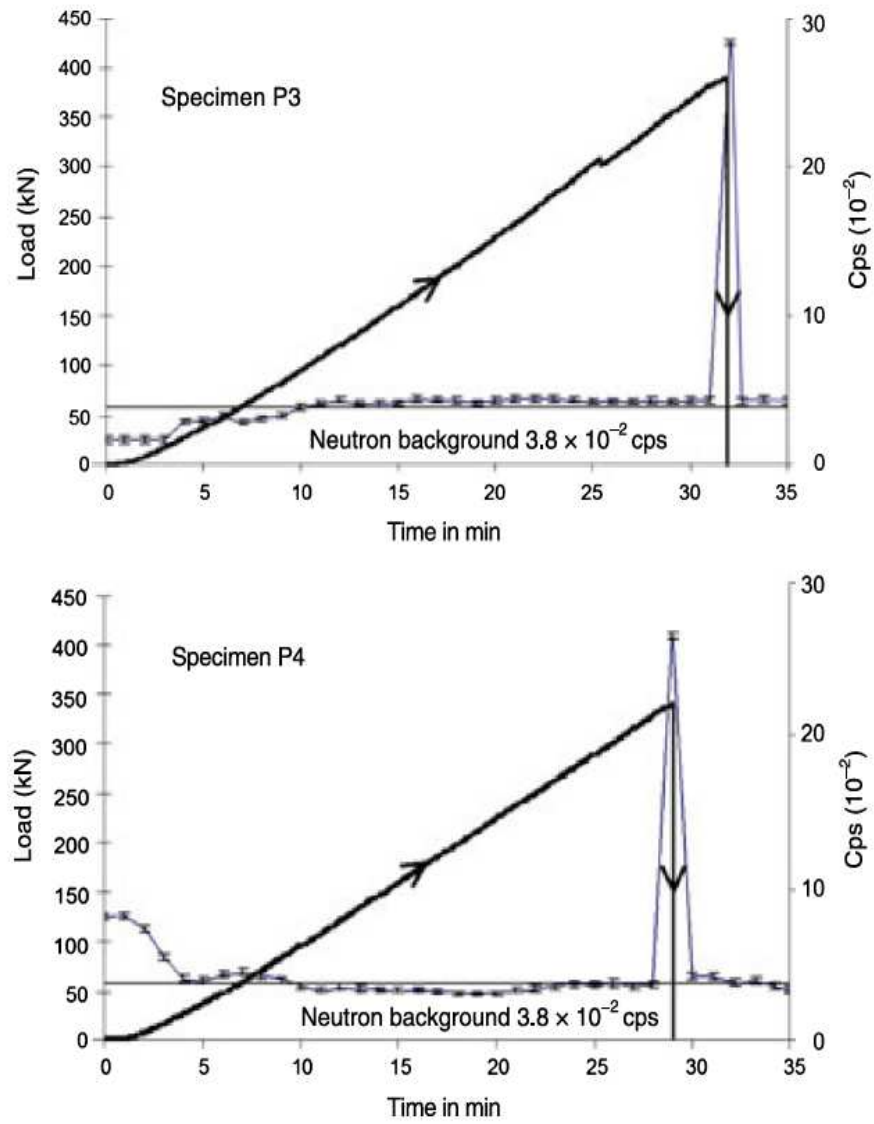
Figure 2 Luserna granite (specimens P3 and P4) crushing test results.

As what concerns the machinery used for the experiments, a servo-hydraulic or servo-controlled press working by means of digital control unit was adopted. The management software is TESTXPERTII by Zwick/Roel (Zwick/Roel Group, Ulm, Germany), while the mechanical parts are manufactured by Baldwin (Instron Industrial Products Group, Grove City, PA, USA). The applied force is determined measuring the pressure in the loading cylinder by means of a transducer. The error in the determination of the force is 1%, which makes it a class 1 mechanical press. The stroke of the press platen in contact with the test specimen is controlled through a wire-type potentiometric displacement transducer [1].

For granite specimens (P3 and P4) the figures show clear NE peaks corresponding to the sharp drops of the applied load. When specimen P3 failed, the count rate of neutron emission was $28.3 \cdot 10^{-2} \pm 0.2 \cdot 10^{-2}$ *cps* [1]. This corresponds to an equivalent flux of thermal neutrons of $43.6 \cdot 10^{-4} \pm 0.3 \cdot 10^{-4}$ $n_{thermal}$ *(s cm^{-2})*. With regards to specimen P4, at the time of the failure the count rate was found to be $27.2 \cdot 10-2 \pm 0.2 \cdot 10-2$ *cps*, which corresponds to an equivalent flux of thermal neutrons of $41.9 \cdot 10^{-4} \pm 0.3 \cdot 10^{-4}$ $n_{thermal}$ *(s cm^{-2})*. However, crushing marble specimens did not produce NE above the average background level that was $3.8 \cdot 10^{-2} \pm 0.2 \cdot 10^{-2}$ *cps* corresponding to an equivalent flux of thermal neutrons of $5.8 \cdot 10^{-4} \pm 0.3 \cdot 10^{-4}$ $n_{thermal}$ *(s cm^{-2})*.

In 2011 and 2012, new results of three different types of tests were published; that is, quasi-static and cyclic-fatigue tests at low (2 Hz), intermediate (200 Hz) and high (20 kHz) loading frequencies were carried out [21] [24]. Specimens of brittle rocks of Green Luserna Granite of varying size and shape were tested to monotonic displacement control compression, cyclic loading and ultrasonic vibration. Table 1 shows geometry and characteristics of the cylindrical specimens used for displacement control monitoring tests; diameter, height and slenderness are indicated respectively as D, H and H/D.

Table 1 Geometric characteristics of the Green Luserna Granite specimens.

Granite specimen	Geometry of the specimen		
	D (mm)	H (mm)	$\lambda = H/D$
P1	28	14	0.5
P2	28	28	1
P3	28	56	2
P4	53	25	0.5
P5	53	50	1
P6	53	101	2
P7	112	60	0.5
P8	112	112	1
P9	112	224	2

It is worth mentioning that while the compression experiments were conducted at Politecnico di Torino, the ultrasonic test was carried out at the Medical and Environmental Physics Laboratory of the University of Torino (Turin, Italy). In Figure 3, Figure 4 and Figure 5 are presented the most significant results in terms of neutron emission detection count rate associated to their relevant load curves for three specimens subjected to uniaxial displacement control compression. Carpinteri et al. reported that, when failure occurred, only three (P6, P8, P9) out of nine specimens were associated to NE corresponding to a count rate one order of magnitude higher than the natural background level of emission measured between $(3.17\pm0.32)\cdot10^{-2}$ *cps* and $(4.74\pm0.46)\cdot10^{-2}$ *cps*. In details, specimen P6, P8 and P9 failed with peaks of NE count rates of $(25\pm6.01)\cdot10^{-2}$ *cps*, $(30\pm11.10)\cdot10^{-2}$ *cps* and $(30\pm11.00)\cdot10^{-2}$ *cps* respectively.
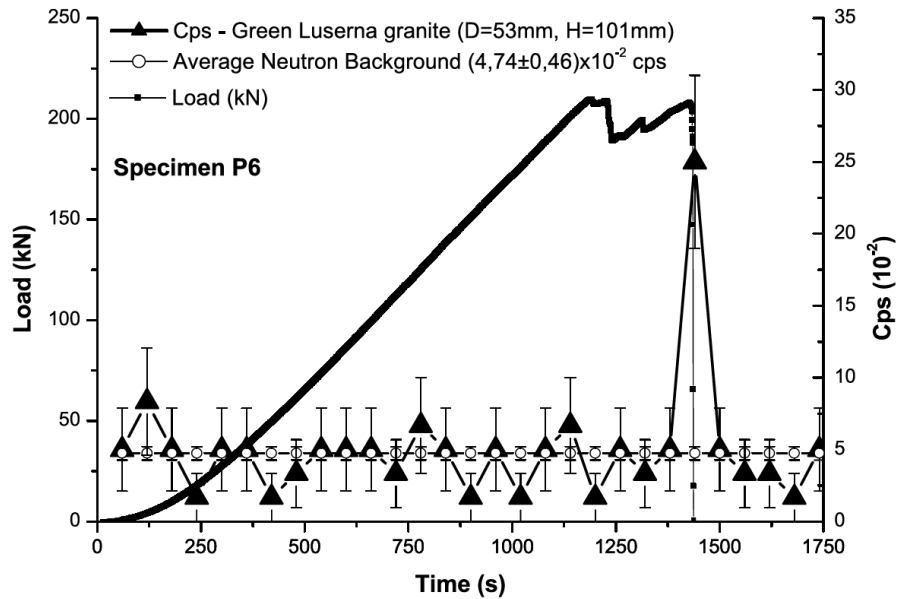
Figure 3 Green Luserna granite (specimen P6): load curve and NE count rate.

The failure of two specimens (P1, P5) was accompanied by a count rate between two and almost four times the background, while four specimens showed no significant results. It is evident from the figures that dimensions and geometry of the specimens are, along with the brittleness, discriminant factors for the occurrence of the NE when fracture takes place.

Interesting results were obtained also from the cyclic compression test (Figure 6), where the dose of neutrons was measured throughout the entire process by means of bubble detectors [21]. Figure 6 shows the trend of the measured dose as increases above the natural background level throughout the test.
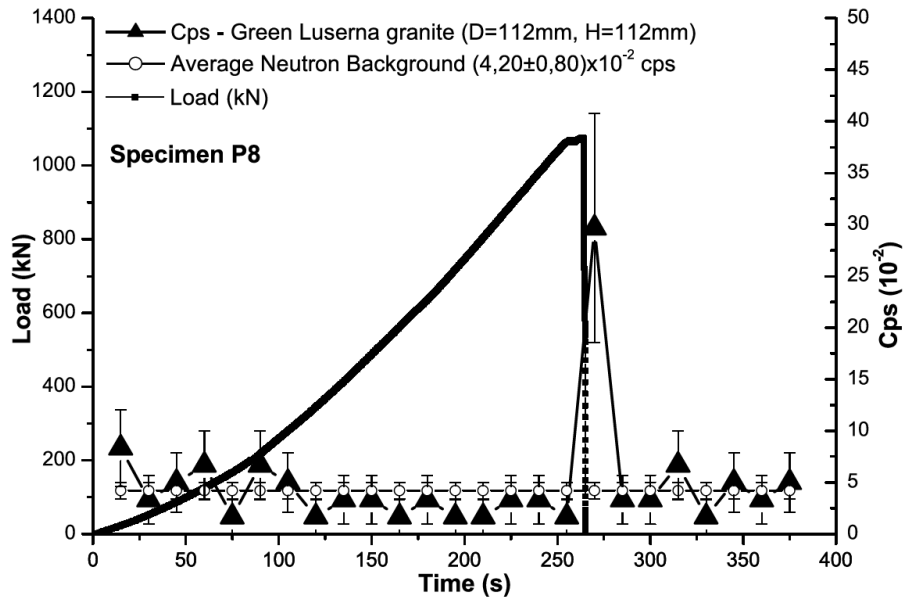
Figure 4 Green Luserna granite (specimen P8): load curve and NE count rate.

According to what has been described above, the results concerning neutron emission measurement reported by Carpinteri et al. prove to be the evidence of a strict dependence of a nuclear phenomenon on the fracturing process. Specifically, the neutron flux appears to depend, as mentioned before, on the iron content, on the brittleness of the specimen and is affected by the size effect: larger sizes imply a higher brittleness, a more relevant strain energy release [2] [25]. It is an interesting finding that gamma rays have not been detected so far in the experiments.
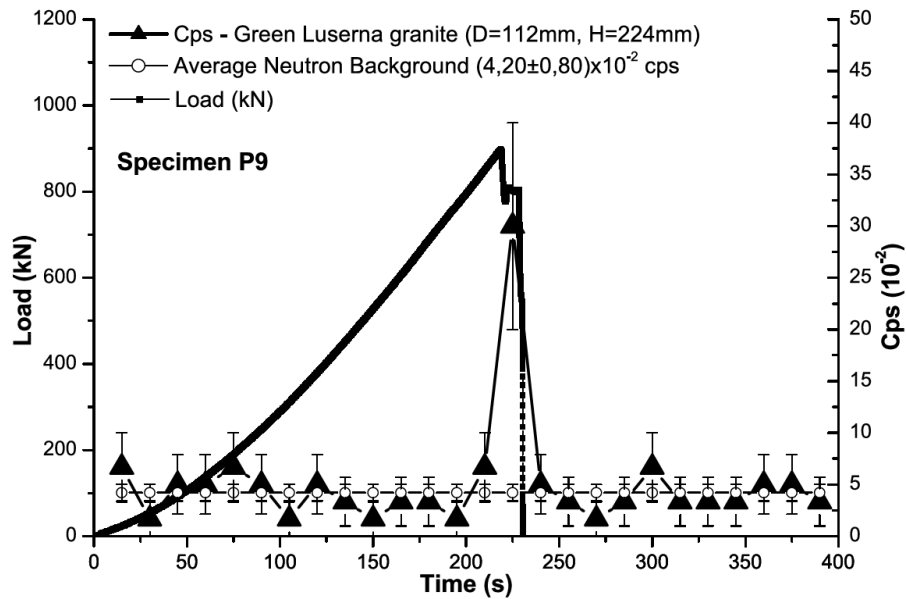
Figure 5 Green Luserna granite (specimen P9) load curve and NE count rate.

In order to understand such complex phenomena, diverse measurements were made by the research team of Professor Carpinteri: analyses of the chemical composition of the specimens tested under compression. In particular, as the hypothesis implied that the whole failure process of the material is involved, then cracked areas of specimens have been investigated. Therefore, fracture surfaces of the material were analysed and their composition characterized through a Field Emission Scanning Electron Microscope (FESEM) applying the technique of the Energy-dispersive X-ray Spectroscopy (EDX or EDS) [21] [26]. The average composition of fracture surfaces was compared to that of non-cracked surfaces of the same specimens to investigate the iron content. The general outcome was that the specimens seemed to have higher iron concentration on non-cracked surfaces than they had on fracture surfaces. Additionally, higher contents in aluminium and magnesium were found on the fractured areas with respects to the non-damaged surfaces [21].
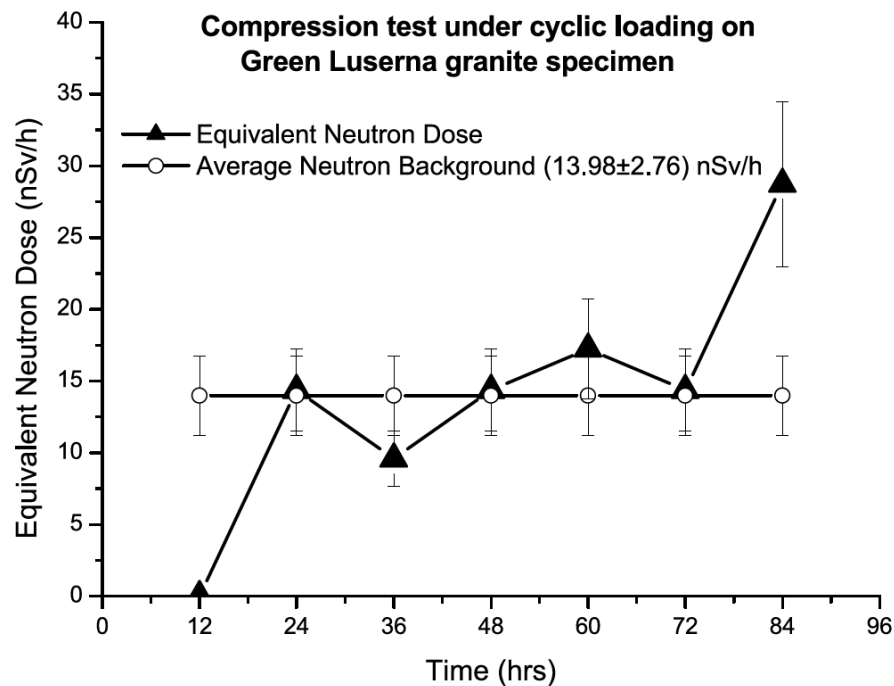
Figure 6: Green Luserna granite: equivalent neutron dose in cyclic compression test.

In detail, analyses were conducted on two crystalline phases present in Luserna Granitic specimens used for the crushing tests: phengite and biotite [26]. These two minerals are common in the Luserna stone, specifically, 20% phengite and 2% biotite. The EDS technique showed again interesting average differences when comparing the composition of the external non-damaged surfaces to that of fractured ones. The phengite analysed on the fracture surface had on average 2.2% (mass concentration) less iron than that on the external surface had. Analogously, the biotite on the fracture surface had on average 3% less iron than that on the external surface. Nevertheless, the average mass concentration of the aluminium was 2% higher in the phengite of the fracture surface than it was in that of the external one. Similarly, considering the biotite, the average mass concentrations of aluminium, silicon and magnesium were respectively 1.5%, 1.2% and 0.7% higher on the fracture surface than they were on the external surface. Although the author of this thesis did not include any reference in the bibliography, he assisted in

analyses of the composition that were also conducted on specimens of magnetite before and after crushing tests. The iron decrement in magnetite was found to be of 27.9%, compared to an overall increment of 27.7% in lighter elements. Although the percent variations might seem relatively low and coincidental, they might represent important indirect evidence, if approached from a specific point of view. Considering such compositional differences associated to the NE flux measured during the crushing of the specimens, the data could be interpreted as "two faces of the same coin": the neutrons and compositional variations can be interpreted as direct and indirect proofs of piezonuclear reactions triggered by brittle fracture in solid materials. Under the light of this new approach and consistent with the experimental data, new types of fission reactions were proposed by Carpinteri et al. Two of the most important involve iron, aluminium, silicon and magnesium as follows:

$$Fe_{26}^{56} \rightarrow 2Al_{13}^{27} + 2neutrons \qquad\qquad 1.1$$

$$Fe_{26}^{56} \rightarrow Mg_{12}^{24} + Si_{14}^{28} + 4neutrons \qquad\qquad 1.2$$

Recent studies showed that there is a connection between what Carpinteri and his research team found in the laboratory and the evolution of the Earth, especially in terms of the composition of the crust [27] [28] [29]. In the history of our planet the composition of the Earth crust changed over time. It is known from the literature that 3.8 and 2.5 billion years ago substantial changes occurred in correspondence with an intense period of activity of tectonic plates [27]. Figure 7 shows the evolution of concentration of most important metals composing the Earth's crust: iron (Fe), nickel (Ni), aluminium (Al) and silicon (Si) [29]. A stepwise pattern of variation of the metallic composition in Hadean and Archean Earth's protocrust and in Earth's continental crust is represented. Considering the entire life of our planet and all the most abundant chemical elements [30] [31] [28], it can be seen how ferrous elements have dramatically decreased in the Earth's Crust (-12%), whereas at the same time aluminium and silicon have increased (+8.8%) (Figure 7) [32].
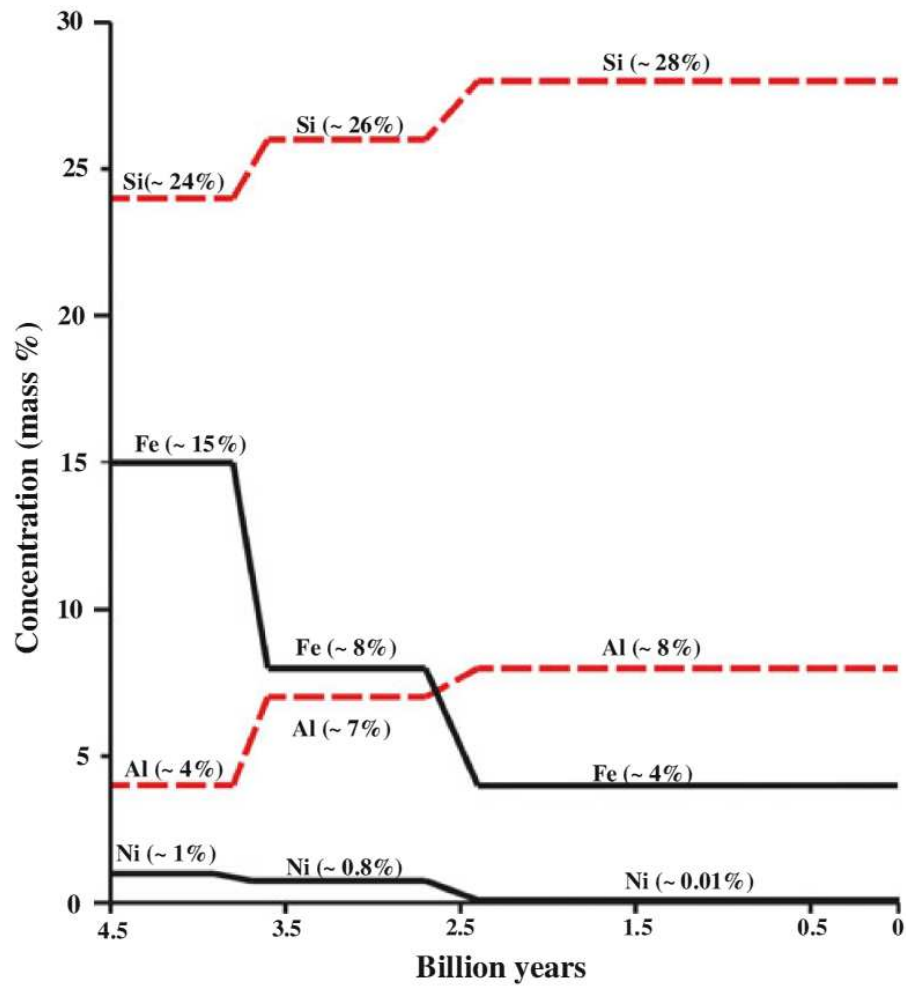
Figure 7 Metallic composition evolution of the Earth's crust.

Observing Figure 8, it is not just a remarkable coincidence that the largest iron mines and reservoirs are distributed on the continental Earth's crust in areas with low seismic risk and relatively far from fault lines. On the contrary, the largest reservoirs of aluminium are located relatively closer to fault linesFigure 9Figure 9 [32].

Iron reservoirs:
▲ more than 40 Mt/year
▴ from 0.5 to 40 Mt/year
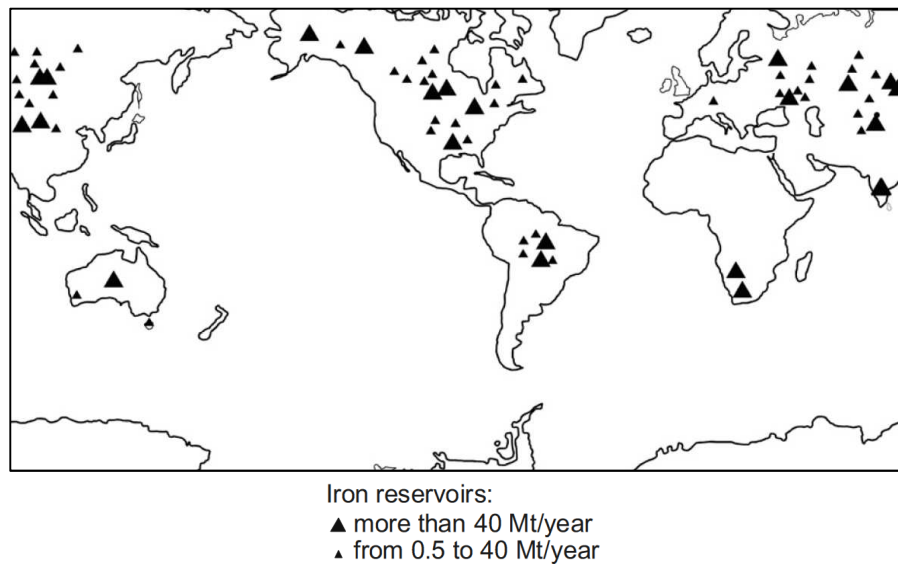
Figure 8 Distribution of iron reservoirs on the continental Earth's crust.

Figure 9 shows such aluminum reservoir distribution on Earth with respect to andesitic formations, subduction lines and plate trenches on the continental Earth's crust. The evolution of most important alkaline (Na, K), alkaline earth metals (Ca, Mg) along with the oxygen concentration on the Earth's crust follows a stepwise pattern as it is illustrated in Figure 10. Mass percentage concentration patterns in Hadean and Archean Earth's protocrust and in Earth's continental crust were studied [29].
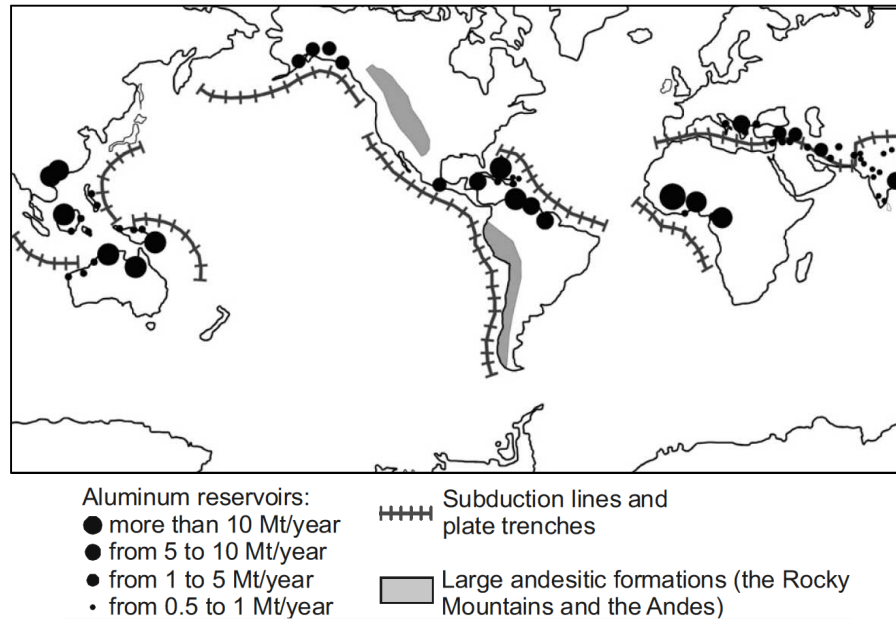
Figure 9 Distribution of aluminium reservoirs on Earth.

An increment in magnesium (+3.2%), which then transformed into carbon, may be assumed as the origin of carbon-rich primordial atmospheres. Similarly, alkaline-earth elements have strongly decreased (-8.7%), whereas alkaline elements (+5.4%) and oxygen (+3.3%) have increased. The appearance of 3.3 % oxygen represents the well-known Great Oxidation Event (Figure 10), a phenomenon that led to the formation of oceans and the origin of life on our planet Figure 10 [29].
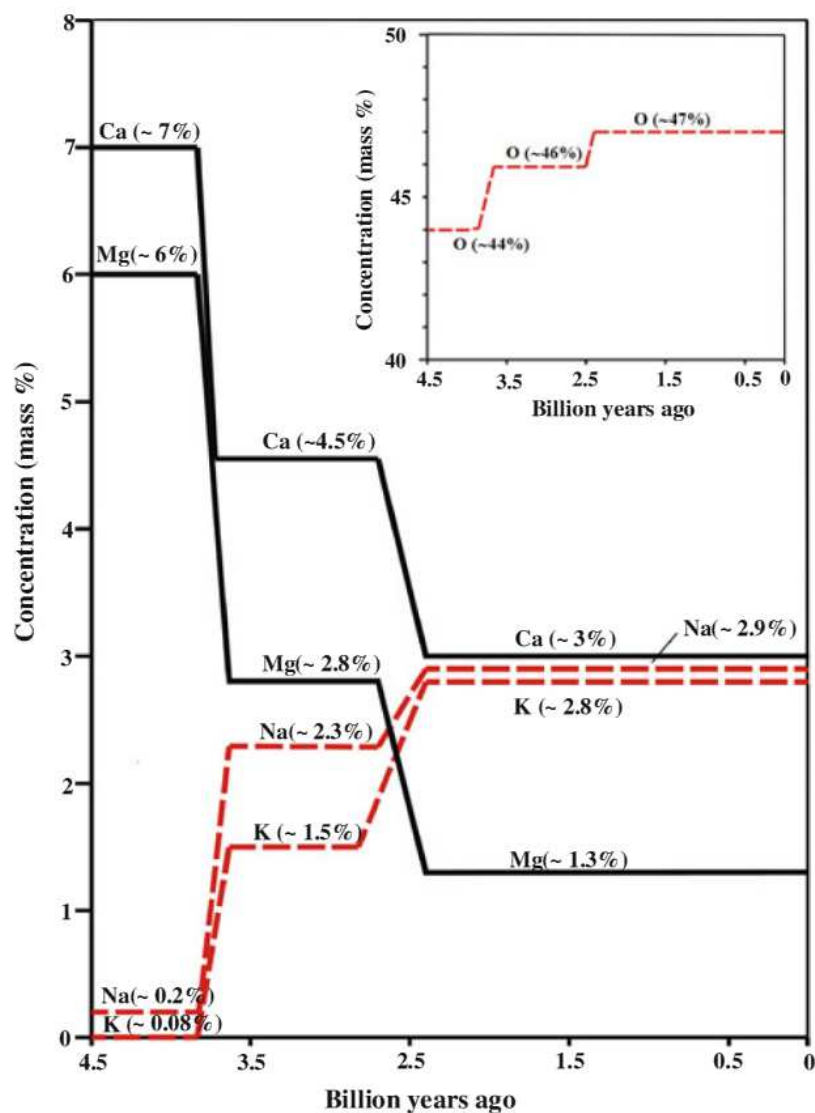
Figure 10 Alkaline, alkaline earth metals and oxygen.

According to what has been discussed above related to the experimental data and knowledge about the evolution of the Earth, a series of piezonuclear reactions

was conjectured by Carpinteri et al. (Table 2). These fission reactions were hypothesized from proofs obtained from EDX analyses of fractured specimens and also contribute to explain the changes of the composition of different environments on Earth throughout its long evolutionary processes.

Table 2 Piezonuclear reactions hypotheses.

Earth's Crust Evolution

(1)	$Fe_{26}^{56} \rightarrow 2\,Al_{13}^{27} + 2\text{ neutrons}$
(2)	$Fe_{26}^{56} \rightarrow Mg_{12}^{24} + Si_{14}^{28} + 4\text{ neutrons}$
(3)	$Fe_{26}^{56} \rightarrow Ca_{20}^{40} + C_{6}^{12} + 4\text{ neutrons}$
(4)	$Co_{27}^{59} \rightarrow Al_{13}^{27} + Si_{14}^{28} + 4\text{ neutrons}$
(5)	$Ni_{28}^{59} \rightarrow 2\text{ }Si_{14}^{28} + 3\text{ neutrons}$
(6)	$Ni_{28}^{59} \rightarrow Na_{11}^{23} + Cl_{17}^{35} + 1\text{ neutron}$

Atmosphere evolution, Ocean Formation and Origin of Life

(7)	$Mg_{12}^{24} \rightarrow 2C_{6}^{12}$
(8)	$Mg_{12}^{24} \rightarrow Na_{11}^{23} + H_{1}^{1}$
(9)	$Mg_{12}^{24} \rightarrow O_{8}^{16} + 4H_{1}^{1} + 4\text{ neutrons}$
(10)	$Ca_{20}^{40} \rightarrow 3C_{6}^{12} + He_{2}^{4}$
(11)	$Ca_{20}^{40} \rightarrow K_{19}^{39} + H_{1}^{1}$
(12)	$Ca_{20}^{40} \rightarrow 2O_{8}^{16} + 4H_{1}^{1} + 4\text{ neutrons}$

1.5   Chemical evolution in the solar system

Even in the case of the other planets of the Solar System there is experimental evidence that can be interpreted in the light of piezonuclear fission reactions [28]. In particular, the data coming from different surveys on the crust of planet Mars, made available by the NASA space missions over the past 15 years, suggest that

the increase in certain elements (iron, chlorine, and argon) and the concomitant decrease in others (nickel and potassium), together with the emission of neutrons from the major fault lines in the planet, should all be considered as strictly correlated phenomena [33] [34] [35]. These data provide a clear confirmation that seismic activity has contributed to the chemical evolution of the Red Planet. Similar experimental evidences are concerning Mercury, Jupiter (its Great Red Spot emits considerable fluxes of neutrons), and the Sun itself [28]. The piezonuclear phenomena are triggered by earthquakes in rocky planets and by storms in gaseous planets. In the Sun, for example, the drastic decrease in lithium appears to be due to the fission of the same lithium into helium and hydrogen.

Chapter 2

2 BRIEF HISTORY AND LITERATURE OF COLD FUSION

Before starting from the event leading to the development of the research of cold fusion, it is worth mentioning the vast work of the Los Alamos experimentalist, Edmund Storms, as described in his two books on Cold Fusion. He introduces his first book, in which his experience on the cold fusion research is summarized, saying that after reading all that has been published on the matter, he is certain the basic claims are correct and are caused by a previously unobserved nuclear mechanism operating in complex solid structures [36]. Storms is one of the most known and accredited researchers of cold fusion, which gives significance to his statement. This means that nuclear effects occurring in condensed matter are somehow real. However according to Storms such novel effects occur only in unique and very small locations, defined as "nuclear active environments" within the matter [36]. What is referred to as Cold Fusion, is not cold in absolute terms of course. It can be considered cold when compared to Hot Fusion, which involves high-energy physics, and it is not normal fusion as it is based on solid state physics and chemistry [36]. Again Storms states that what is taught and thought to be true in nuclear physics is only partially correct and, in the preface of his book his words are: "A totally unexplored environment, in which nuclear interaction can take place, apparently exists within solid materials" [36].

2.1 Origins and facts about cold fusion

The origin of the research of Cold Fusion could be conveniently fixed to a specific date: March 23, 1989. That day Professors Martin Fleischmann and Stanley Pons announced publicly that they found a new process to induce nuclear fusion [36]. In particular, they described an electrochemical process to induce the nuclear fusion of deuterons [37]. After this numerous scientists and researchers started working on reproducing what was called the Fleischmann and Pons effect. In time, new and interesting results came out: remarkable heat production, traces of new elements and also occasional neutron emissions that had to be interpreted as consequences of some nuclear phenomenon. Physicists and chemists started questioning what was traditionally known about nuclear quantum mechanics and the relationship between chemistry and nuclear physics [38]. The study of Low

Energy Nuclear Reactions (LENR) became the key to the interpretation and understanding of the massive amount of experimental data. If nuclear reactions occur in condensed matter, say ordinary matter, the energy involved had to be lower than those related to fission and hot fusion [39].

Several proofs of anomalous nuclear reactions occurring in condensed matter have been observed in phenomena of electrolysis. Despite the great amount of experimental results coming from the so-called Cold Nuclear Fusion and LENR research activities, a full comprehension of these phenomena is yet to be achieved. However, as reported by most of the articles devoted to Cold Nuclear Fusion, there are some common particular features: the excess heat, the neutron emissions and the appearance of micro-cracks on the metal host during loading processes, especially when palladium was used [36].

Kaliski, Winterberg and their co-workers [28] provided some interesting data about fission-fusion processes. Kaliski et al. investigated neutron emission from explosive compression and implosion fracture processes. Apparently, the pressure involved in the different phenomena favoured the emission of neutrons. This could be interpreted as a support to the idea of piezonuclear reactions occur in radioactive solids [40] [41]. Winterberg et al. proposed to implode dense thermonuclear plasma by a shell of fissile material: the ignition of the plasma would release neutrons that caused fission reactions in the imploding shell [42].

Professor Yoshiaki Arata of the Osaka University developed a "solid fusion" reactor carrying out experiments on the so-called Cold fusion [43] [44]. He experienced that Palladium nano-particles were able to absorb deuterium atoms from D2-pressurized gas. Stimulating the deuterated Pd particles with ultrasonic waves resulted in simultaneous excess heat and ^{4}He emission without any hazardous rays. Arata stated that this was the result of intense deuterium fusion in the host metal lattice, which he referred to as solid fusion.

As regards to other nuclear effects, R.P. Taleyarkhan reported observations of tritium decay and neutron emission associated with the collapse of bubbles in deuterated acetone [45]. In details, such observations were considered as due to deuterium-deuterium fusion reactions occurring in the imploding bubbles generated by acoustic cavitation. Hydrodynamic shock calculations indicated that highly compressed bubbles formed in a temperature condition range from 10^6 to 10^7 kelvin, and the neutron emission was about 2.5 million eV.

Other most relevant papers on the so-called Cold Nuclear Fusion describe broad experimental activities conducted on electrolytic cells powered by direct

current and filled with ordinary or heavy water solutions [36]. Considering what Fleischmann and Pons proposed in 1989, apparently the Palladium electrode reacted with the deuterium coming from the heavy water solution [37]. Later works reported that Pt and Ti electrodes had also been electrolyzed with heavy water (D_2O deuterium oxide) to produce extra energy and chemical elements previously absent [36]. Extra energy has been also measured during electrolysis with Ni cathodes and H_2O-based electrolyte. Furthermore, it was affirmed that a voltage sufficient to induce plasma electrolysis generates a large variety of anomalous nuclear reactions when Pd, W, or C cathodes are adopted [46]. In many of these experiments conducted in electrolytic environments, the generated heat was calculated to be several times the input energy, and the neutron emission rate was measured to be more than twice as high as the natural background level [36].

In 1998, Dr. Tadahiko Mizuno presented in his book "Nuclear Transmutation: the reality of cold fusion" a wide list of bright and dark side aspects related to the topic of cold fusion [47]. Together with Storms, Mizuno is one of the most dedicated scientists to cold fusion. He documented numerous data concerning his and his collaborators own daily research experience. In general, he built his own "cold fusion cell" experimenting on it and describing the results of various measurements he conducted. Neutron (2.45 MeV) flux was detected to be a million times smaller in proportion to the heat than it is in hot fusion. Heat was the main feature and neutrons appeared sporadically [47]. "Mizuno electrolytic cell" with its anode, cathode and electrolyte operated at 100 °C and 10 atmospheres of pressure. Dr. Mizuno documented proof of tritium and nuclear transmutation effects involving the metal lattice [47]. In later works, Mizuno reported that most evident excess heat was obtained through the condition of plasma electrolysis achieving simultaneously electrolysis and pyrolysis of water with K_2CO_3 electrolyte [48]. Conducting EDX measurements, new elements such as Ca, Fe, Zn, In and Ge where observed. Also in his previous experiments, Mizuno observed isotopic changes of reaction products [46]. Palladium cathodes were used and subjected to electrolysis in heavy water. Results showed that the isotopic distribution of certain elements measured on the cathode surface differed from the natural distribution. Elements such as N Pb, Fe, Ni, Cr, and Pd were investigated noticing that the isotopic distribution of Pd, Pb and Pt on the surface and in the electrodes deviated from the natural isotopic abundances. More important, it was noticed that cracks formed on the surface of palladium electrodes during electrolysis. These results suggested that nuclear transmutation reactions took place during the electrolysis process.

Later, in 2002 Dr. Philipp M. Kanarev and Mizuno reported other results about transmutation of atomic nuclei during many hours of plasma electrolysis [49]. They investigated alkaline and cathodic material metals, using iron cathodes (99.90% of Fe) immersed in KOH and NaOH solutions. The chemical compositions of the surface of the iron cathodes were analysed and new elements appeared after the experiments. EDX spectroscopy revealed the presence of Si, Cr, and Cu on the electrode that operated in KOH solution, and Al, Si, Cl, Ca, Cr and Cu on the one in NaOH. These findings are important evidence of compositional changes due to nuclear phenomena related to plasma electrolysis of water.

In 2007 and later on, Dr. Pamela A. Mosier-Boss et al. presented interesting anomalous results related to detection of energetic charged particles emitted during Pd/D co-deposition experiments [50] [51]. Mosier-Boss and her collaborators used plastic polymer CR-39 (not Chromium) as a solid state nuclear track detector of the charged particles. In the CR-39 detector, they observed pits generated during the co-deposition that had features consistent with those of pits that are of nuclear origin.

It is, now, necessary to focus the attention on those structural and physical alterations observed on materials and metals adopted in all laboratory experiences mentioned so far and other related to them. The observation of a wide range of surface damages such as holes, pits, cracks and microcracks in metal cathodes and other electrodes after hours of testing is well documented [36] [47] [52]. Specifically, the presence of cracks is to be accounted thoroughly. In fact, formation of crack and microcrack is one central feature that connects cold fusion research to piezonuclear effects. Above all, piezonuclear fission reactions, as illustrated in the first chapter of this thesis, have been specifically investigated considering fracture mechanics-related effects. Nevertheless, numerous related and remarkable data arise from nuclear physics. Chemical assisted phenomena like the ones related to the electrolytic environment mentioned above, represent the perfect case study. Electrochemical and nuclear phenomena meet fracture processes in such a complex environment. Thence, concepts like mechanical stress relief and metal embrittlement cannot be left aside when investigating crack formation and stress propagation processes.

There are cases in literature where scientists already associated nuclear with pressure-like conditions: in fact, the term "piezonuclear" was used when referring to particular nuclear fusion conditions. For instance, back in 1986, Van Siclen and Jones referred to piezonuclear fusion when investigating variations of the density of collection of hydrogen isotopic molecules [53]. They calculated a rough

theoretical estimate of the rate of fusion of nuclei in a deuterium molecule predicting an increase in fusion rate as the density of collection of molecules is increased.

In 1990, Professor Giuliano Preparata reported the terms "fractofusion" and "fractoemission" as referring to emission of charged particles of both signs and electromagnetic radiation ensuing mechanical processes of formation of fractures in solids [54]. Preparata suggested that cracks could generate sufficient voltage gradient and/or temperature to initiate a hot fusion within a crack itself. Furthermore, neutrons detected from fractofusion mechanisms-related studies have energies close to those relative to hot fusion.

Nevertheless, Storms suggested that cracks could be as well considered as the locations of LENR processes in a material, because specific nuclear active environments appear to form when cracks are produced [36] [55]. It was proposed that resonating structures in crack processes would induce fusion nuclear reactions between hydrogen isotopes trapped in microcracks.

It is, however, important not to confuse hot fusion with LENR; they are mechanisms substantially different from one another. Preparata once wrote that "the mechanisms occurring in the condensed matter are much more subtle and powerful than it has been hypothesized and studied upon until now" [38].

Very recently, in actual fact, a theoretical interpretation about disintegration and fission of nuclei has been proposed by Professors Allan Widom and Yogendra Srivastava. They have been investigating neutron emissions as a consequence of nuclear reactions taking place in iron-rich rocks during brittle fracture and micro-cracking [56] [57]. Widom and Srivastava presented data of iron nuclear disintegrations observed when rocks containing such nuclei were crushed and fractured. The resulting nuclear transmutations were particularly evident in the case of magnetite rocks and iron-rich materials in general. The same authors argued that neutron emissions might be related to piezoelectric effects and that fission of iron may be a consequence of the photodisintegration of the same nuclei.

As it was presented above, numerous former and latest tests appeared to have various analogies to Cold Fusion research: neutron and alpha particle emissions as well as excess heat. Additionally, specific pressure conditions were often involved. In general, for what concerns the products, traces of ^{4}He were found to be produced when deuterium or hydrogen isotopes were present. Proofs of a variety of nuclear reactions were investigated and led to observe that some of those reactions occurred at a rate sufficient to generate measurable excess heat.

Although hazardous radiation might be produced, the radioactivity did not reach harmful level [36]. At the same time, appreciable variations in the chemical composition of the materials involved in brittle or fracture processes were detected.

2.1.1 Nuclear anomalous effects and Piezonuclear fission

According to the data reported in the previous section, it is evident that plenty of metal materials were in strict contact to experimental electrochemical environments. The latter are rich in hydrogen by definition. Therefore, hydrogen embrittlement of the metals composing the electrodes (Pd, Ni, Fe, Ti, etc.) has to be taken into account. Such phenomenon is strictly related to crack processes as it was mentioned in section 1.2 of Chapter 1. It is, as a matter of fact, an important aspect of a much larger mechanical interpretation to nuclear effects observed and investigated as of now.

Taking Considering the many data collected by Carpinteri et al. about NE and compositional variations on the crust of the Earth, and considering also what is known about cold fusion, the ensuing question could be whether a mechanical interpretation of LENR and chemical assisted nuclear reactions (CANR) effects can be provided according to the piezonuclear hypothesis. Recent studies have been considering piezonuclear reactions related to earthquake and also triggered by them [24]. Therefore, according to what has been studied by Carpinteri and his research team, piezonuclear phenomena could be observed at different scales, in a number of various environments that present, though, specific analogue conditions. As it will be described in more detail in the next chapter, a specific experimental campaign has been conducted by the author of this thesis for the very reason of investigating the repeatable and common conditions that are involved or are thought to trigger mechanisms of piezonuclear reactions.

However, before going further, it is necessary to spend some words summarizing what is known and believed about piezonuclear reactions. The conjecture that can be drawn from the data is that fission nuclear reactions occur in solid material whenever they are subjected to mechanical loading and brought to failure. Not any failure would do the trick though. Observations suggest that brittle fractures must occur and the bigger the specimen is, the more evident the NE is. In fact, size alone is not enough; there is a dependence on the slenderness and brittleness index of the specimen or solid body undergoing rupture. Specifically, given that formation and propagation of microcracks and nanocracks in solid matter induce pressure waves at very high frequency (TeraHertz), anomalies of the

nuclear structures, say neutron and alpha emission, could be triggered by such dynamic phenomena.

Needless to say, investigating structures of nuclei of elements composing materials where anomalies such as those mentioned above (see also Chapter 1) are observed, is of great importance. Even small deviations from conventional assumptions concerning the condensation density of nuclear matter, the concept of an average binding energy per nucleon [39] could have significant implications. Based on the experimental evidence concerning piezonuclear fission, it would suffice to assume that a nuclear structure failure occurs along weak lattice planes within the nucleus, similar to the cleavage fractures known to occur in very hard and strong rocks. A subsequent question would now be: "what if the nucleus is studied as a structure that under the right amount of load cracks?"

Briefly anticipating what will be thoroughly described in Chapter 5, the nucleus could be studied from a geometrical perspective as a tri-dimensional lattice, where the bonds between nucleons are struts and ties and the nucleons themselves occupy the nodes. Most of the models in nuclear structure theory do not provide particular details predicting fission fragment size [58]. Generally, the liquid-drop model (LDM) predicts symmetrical fission (the mother-nucleus divides into two equal daughter-fragments).Only by adding an asymmetry parameter LDM predictions are made to agree with experimental data (concerning for example the fission of U^{235}). The shell model predicts fragments containing close shell ("magic") numbers of nucleons, but detailed fragment sizes are not predicted. In contrast, a lattice model would focus more on fragments resulting from the mechanical rupture of a structure. Also a variety of fragment sizes can be predicted, depending on what fracture (fission) plane is considered through the lattice. For this reason, Chapter 5 will show how the lattice model has been used to compare theoretical predictions with the experimental findings concerning the piezonuclear effects observed at different scales.

Chapter 3

3 MECHANICAL INTERPRETATION OF NUCLEAR EFFECTS IN ELECTROLYSIS EXPERIMENTS WITH NICKEL-IRON ELECTRODE

As mentioned in the introduction to this thesis, the author conducted an experimental activity focused on the use of an electrolytic cell. Relevant results were already presented to the Society of Experimental and Applied Mechanics (SEM) conference in 2013 [59] and in 2014 [60]. The aims were to investigate the mechanical effects on the electrodes used in an electrochemical process and then identify nuclear phenomena involved in the process, in particular piezonuclear. In this Chapter the first part of the experimental campaign will be described. To develop this part of the campaign it took a total amount of 38 hours. The activity was conducted using a Ni-Fe (nickel-iron alloy) anode and a Co-Cr (cobalt-chromium alloy) cathode immersed in a potassium carbonate solution. Emission of neutrons and alpha particles was monitored during the experiments and compared to the background level of the environment where the experiments were conducted. The composition of both electrodes was analysed both before and after the electrolysis. After showing the results of the experiments the author will present an interpretation of the features observed. The attention will be focused on those results suggesting that piezonuclear fissions occur in the host lattice of the material composing the electrodes. The symmetrical fission of Ni appeared to be the main and most evident feature. Such reaction would produce either two atoms of Silicon or two atoms of Magnesium with additional fragments as alpha particles. The results also suggest that piezonuclear fission reactions are likely to occur in correspondence to micro-crack and macro-crack propagation on the electrode surfaces, that is, where the metal lattice is more sensible to HE effects.

3.1 Experimental set-up

This section describes the equipment used for the experiment. The circuits providing the voltage difference to the electrodes are presented. The main component of the equipment has the general characteristics of a traditional electrolytic cell as it is shown in Figure 11 and in Figure 12.
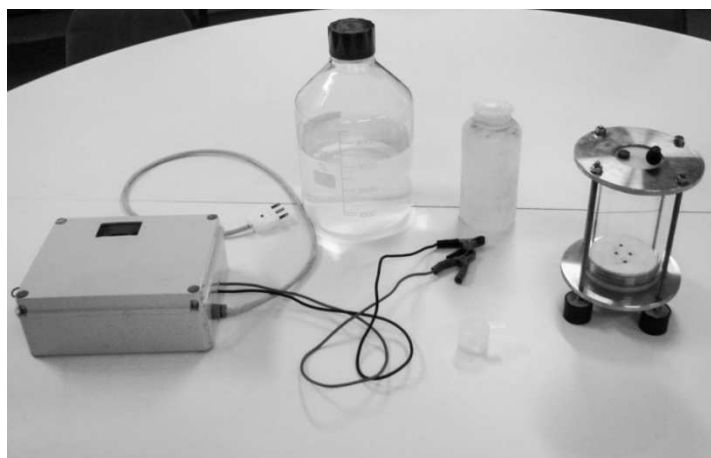
Figure 11 Equipment for electrolysis: power box (on the left), electrolyte jars, electrolytic cell (on the right).

Figure 12 Electrolytic cell: glass cylindrical container sealed with Teflon lids.

First of all, it is necessary to mention Mr. Alessandro Goi and his collaborators. They constructed the electrolytic cell and its power supply circuit (Figure 11). They have been experimenting on it over the past seven years and two years ago, started collaborating with Professor Carpinteri. At the moment of the writing of this thesis, he was the coordinator of the PhD course attended by the author. Mr. Goi provided Carpinteri with the cell (Figure 12) in order to allow his research team to conduct their tests on it. In such context, the author started following the experimental campaign related to the electrolytic cell. The latter was built in order to be appropriately filled with a solution made of water and Potassium Carbonate (K_2CO_3). The electrolytic phenomenon was obtained using two metal electrodes immersed in the aqueous solution. The solution container, named also reaction chamber in the following, is a cylinder-shaped element of 100 mm of diameter, 150 mm high and 5 mm thick. For the reaction chamber, two different materials were used during the experiments: Pyrex glass and Inox AISI 316L steel. The two metallic electrodes were connected to a source of direct current: Ni-Fe based electrode as positive pole (anode), and Co-Cr based electrode as negative pole (cathode). Figure 13 shows the electrodes used for the experiment: from the left hand side of the picture to the right one, a Co-Cr alloy cathode and a Ni-Fe alloy anode. Figure 14 shows the dimensions of the electrodes; in particular, only one electrode is represented as geometry is the same for both cathode and anode. In the figure three different regions of the electrodes are marked to indicate where the chemical composition was measured: the upper part close to the tip, the middle part and the lower part right above the threaded surface.

Figure 13 Electrodes: Co-Cr alloy cathode (on the left) and Ni-Fe alloy anode.
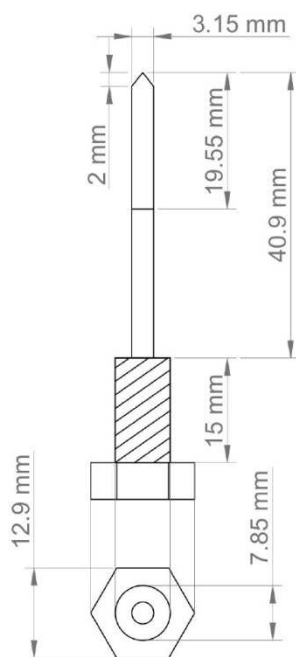
Figure 14 Electrodes geometry and dimensions.

With regard to the experiment described in the present research, after approximately 10 operating hours, generation of cracks was observed on the glass container, which forced the author to adopt a more resistant reaction chamber made of steel; this will be further discussed in section 3.4. Teflon lids were sealed to both top and bottom cross sections of the chamber. Two circular Inox steel plates held insulated Teflon layer lids of the cell by means of four threaded bars. The reaction chamber base consisted of a ceramic plate preventing the direct contact between liquid solution and Teflon lid (see Figure 12). Two threaded holes hosted the electrodes, which were screwed to the bottom of the chamber successively filled with the solution. A valve at the top of the cell allowed the vapor to escape from the reactor and condense in an external collector. The inferior steel flange of the reactor is connected to four supports isolated from the ground by means of rubber based material. Figure 15 reports the scheme of the power supply directly connected to the electrodes of the cell through two poles. A direct current reached into anode and cathode electrodes, provided by the power circuit connected to the AC (alternate current) supply (220 V, 50 Hz) of the national grid. The components of the circuit supplying the electrodes with a voltage difference were linked in series as follows: energy meter measuring the input energy provided by the AC supply grid, an electronic variable transformer (Variac) of the voltage, and a diode bridge rectifying the AC into direct current (DC). Also a voltmeter and an amperometer were connected to the poles directly linked to the electrodes in order to monitor input voltage and DC intensity. A voltage control wheel was also present in the circuit box in order to regulate the voltage provided to the electrodes (Figure 16).
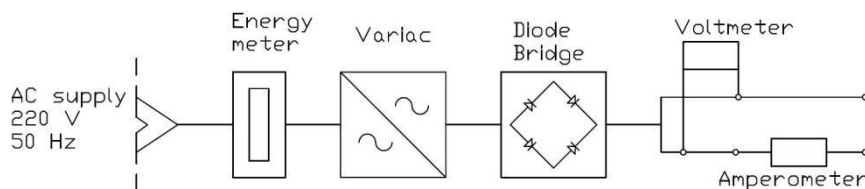
Figure 15 Power circuit diagram.

Figure 16 illustrates the experimental set up of neutron measurement equipment. From the figure it is visible the steel electrolytic cell (left), the neutron counter (top) connected to the tube containing the He^3 type neutron detector (top right), the

bubble neutron dosimeters, voltmeter and amperometer and the power box with the small energy meter display and the voltage control wheel .
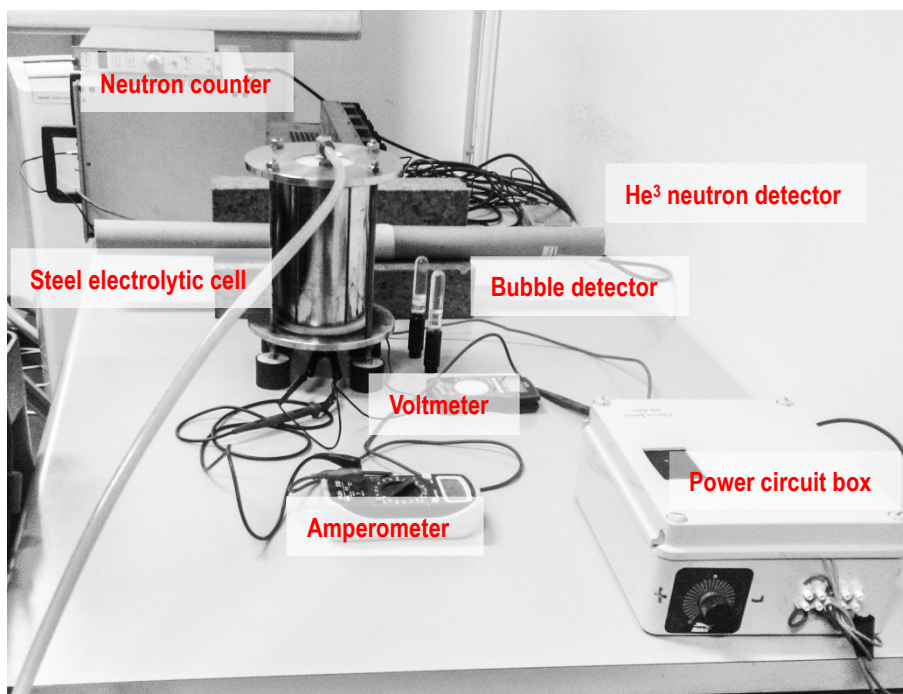
Figure 16 Experimental set up of the measurement equipment.

Different physical quantities were measured during the experiments, such as voltage, current, neutron and alpha particle emissions. Electric current and voltage probes were positioned in specific points of the circuit as it is shown in Figure 15 and Figure 16. The voltage measurements were performed by a differential voltage probe of 100 MHz with a maximum rated voltage of 1400 volts. The current was measured by a Fluke I 310S probe with a maximum rated current of 30 A. Particular attention was paid to the data obtained from the current and voltage probes positioned at the input line powering the reaction chamber in order to evaluate the power absorbed by the cell. From the start (switch on) to the end (switch off) of the electrolytic process, current and voltage were found to vary respectively in a range from 3 to 5 A, and from 20 to 120 V. For convenience, these values were considered as a benchmark to be compared to further

measurements that could be undertaken in future research.

For the description of the neutron emission detector the reader should check the Introduction Chapter, section 1.4 "Evidence of neutron emission related to fracture phenomena: from the laboratory to the earth crust scale".

For what concerns the alpha particle emission, a 6150AD-k probe (Figure 17) with a sealed proportional counter was used, which did not require refilling or flushing from external gas reservoirs [61]. The probe was sensitive to alpha, beta, and gamma radiation. An electronic switch allowed the operating mode "alpha" to detect alpha radiation only, such that in this mode the radiation recognition was very sensitive because the background level was much lower. A removable discriminator plate (stainless steel, 1 mm) distinguished between beta and gamma radiation detection. An adjustable handle could be locked to the most convenient orientation. During the experiments the 6150AD-k probe was used in the operating mode alpha to monitor the background level before and after switching on the cell.

Figure 17 6150AD-k alpha and beta detector.

Finally, before and after the experiments Energy Dispersive X-ray spectroscopy had been performed in order to recognise direct evidence of piezonuclear reactions that could take place during the electrolysis. The elemental analyses were performed by a ZEISS Auriga field emission scanning electron microscope (FESEM) equipped with an Oxford INCA energy-dispersive X-ray detector (EDX) with a resolution of 124 eV @ MnKa. The energy used for the

analyses was 18 KeV.

3.2   Results of detection of neutron and alpha emissions

Above all, it is necessary to point out that beside alpha and neutrons, beta and gamma rays were qualitatively investigated, however, no proofs whatsoever of such radiation above save levels were to be found during the experiments.

Neutron emission measurements performed during the experimental activity are represented in Figure 18.
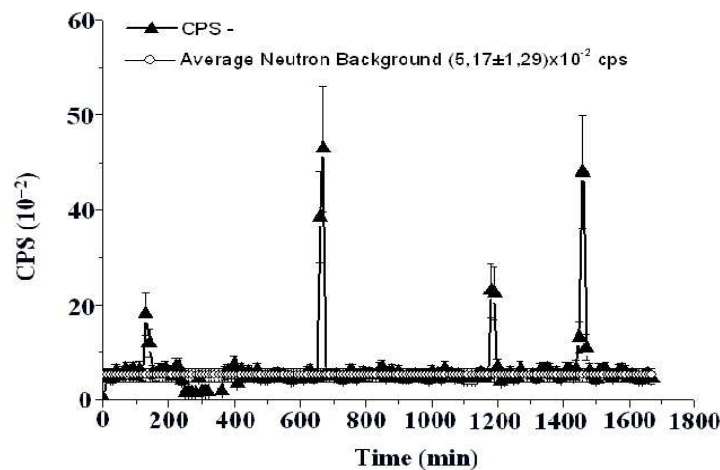
Figure 18 Neutron Emission cps measurements.

The main features observable from the figure are peaks of emissions measured during the experiments and reaching values between 4 and 10 times the background level. The average neutron emission background level of the environment was measured and it is reported in the figure. It corresponded to 5.17 $\pm 1.29 \times 10^{-2}$ cps. The measurements performed by the He^3 detector were conducted for a total amount of time of about 26 hours. The background level was measured during different time spans before switching on and after switching off the reaction chamber. Furthermore, during the cell activity, it was possible to observe that after a time span of about 200 minutes neutron emissions about 4 times higher than the background level were recognized. After 650 minutes from the beginning of the measurements, it was possible to observe a neutron emission

peak of about one order of magnitude greater than the background level. Similar results were observed after 1200 minutes (20 hours) and 1500 minutes (25 hours), when neutron emissions respectively about 5 times and 10 times higher than the background were measured.

In Figure 20, the alpha particle emission measurements are reported. The data are related to an alpha emission level monitored by means of the 6150AD-k probe set to the operating mode "alpha". The measurements shown in figure are referred to the data acquired for a time interval equal to 3600 seconds (60 minutes).
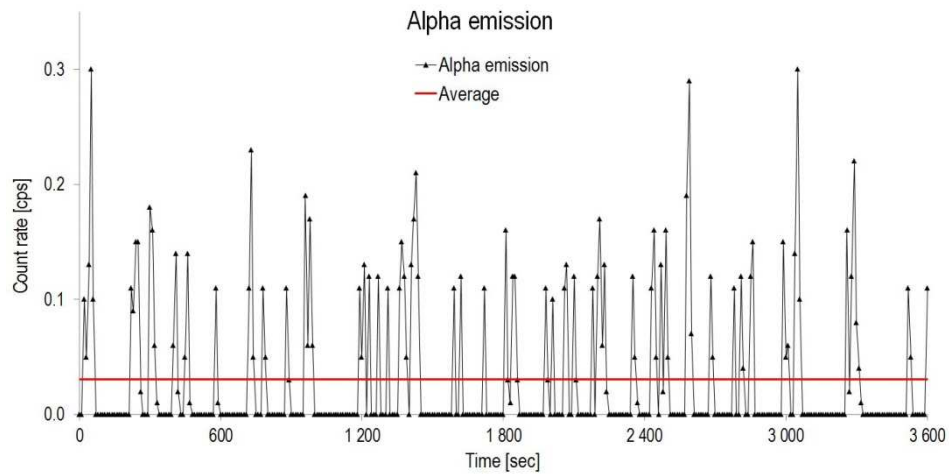
Figure 19 Alpha emission count rates during electrolysis.

Such measures were taken when the reaction chamber was operating. On the other hand, the data in Figure 20 represent the alpha particle emissions corresponding to the background level. They were obtained by measurements acquired when the cell was not operating in a 3600 second window, in order to detect a sample of the natural alpha emission level of the environment.
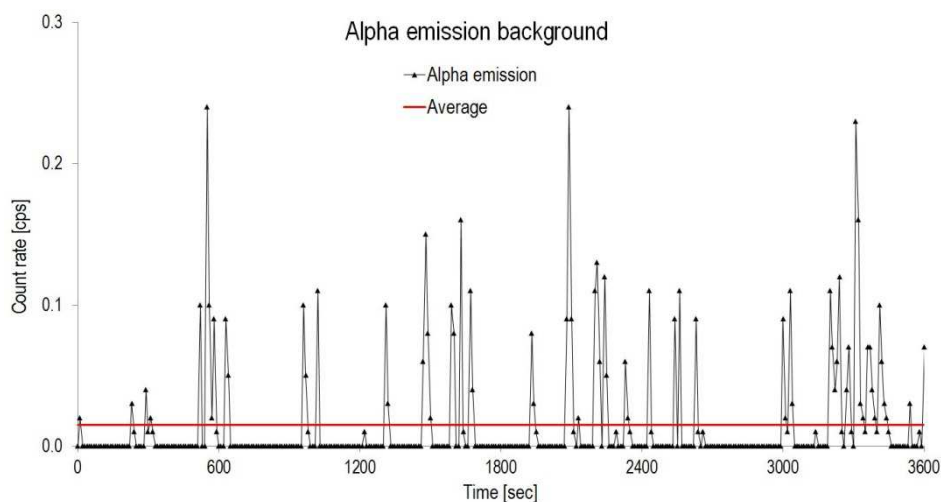
Figure 20 Alpha emission background level.

From these figures, it can be noticed that the number of counts per second acquired by the probe increased considerably when the electrolytic cell was operating (Figure 20). In addition, the average values of two alpha emission incremental time series were computed, one when the cell was switched on and the other when the cell was off. The first time series, showed an average alpha emission of about 0.030 c/s (cps count per second), whereas the second one provided the background emission level in the laboratory with an average value of about 0.015 c/s. It is evident that the average alpha particle emission during the electrolysis is two times higher than the background level one. These results, together with the evidence of neutron emissions reported in Figure 18, were particularly interesting once having considered the compositional variation described later on in this Chapter. In fact, they proved useful to corroborate the hypothesis of piezonuclear fission of important chemical elements constituting the electrodes.

In Figure 21, the cumulative incremental time series of the alpha emission counts are also reported.
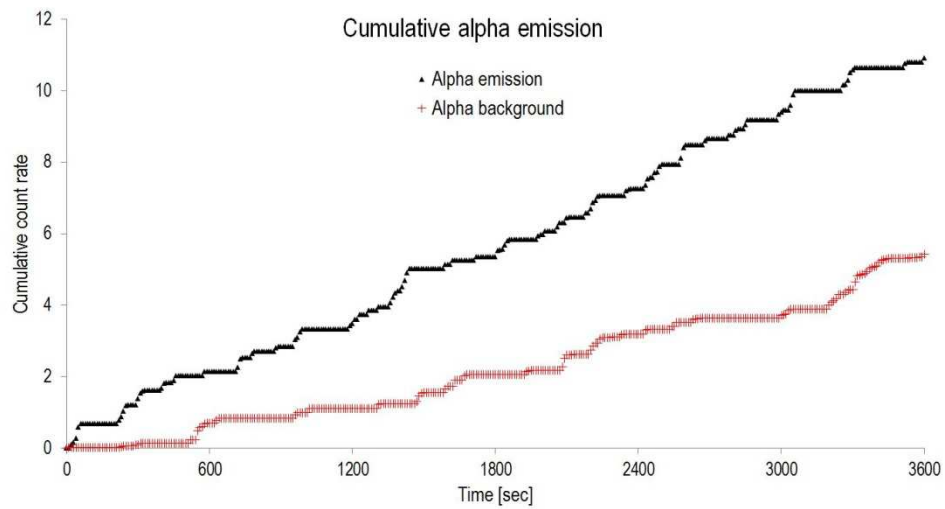
Figure 21 Cumulative alpha emission.

The data corresponding to the measures acquired during electrolysis are reported in black (Alpha emission), while the alpha emission incremental trend corresponding to the environment background level is presented in red (Alpha background). It is evident from the figure how the total amount of counts monitored when the cell was operating (10.91 cps) was approximately twice the value measured for the background level (5.42 cps).

3.3 Superficial chemical composition of the electrodes and piezonuclear effect interpretation

The initial measurement phase implied the use of the Energy Dispersive X-ray spectroscopy (EDX) technique to obtain measurements necessary to evaluate the chemical composition of the two electrodes before the experiments. In particular, a series of measures were repeated in three different regions of interest for each electrode in order to obtain a sufficient amount of reliable data. Such regions are the upper, the middle and the lower part of the single electrode (Figure 14).

In Figure 22, concentrations of each element found on the surface of the Ni-Fe electrode used for the electrolysis is indicated as an average mass percentage of the total concentration measured by means of the EDX spectroscopy.
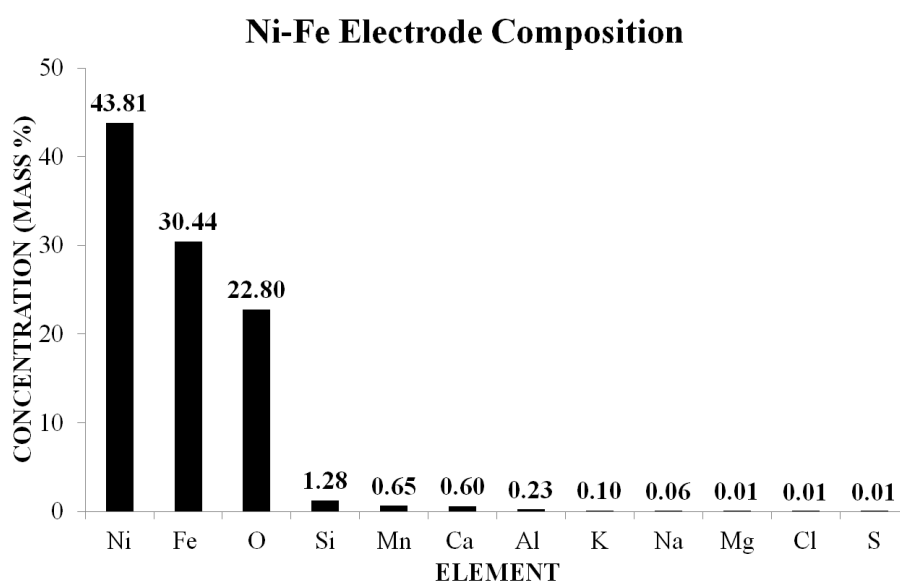
Figure 22 Chemical composition of the Ni-Fe anode.

The original composition of the un-used Ni-Fe electrode (anode) is as follows: approximately 44% nickel (Ni), 30% iron (Fe), and 23% oxygen (O). The remaining percentage includes traces of silicon (Si), manganese (Mn), calcium (Ca), aluminium (Al), potassium (K), sodium (Na), magnesium (Mg), chlorine (Cl), and sulphur (S), observable only in traces (**Figure 22**).

In Figure 23, the composition of cobalt-chromium alloy cathode is shown. The percent average mass concentration of each element found on the electrode is displayed.
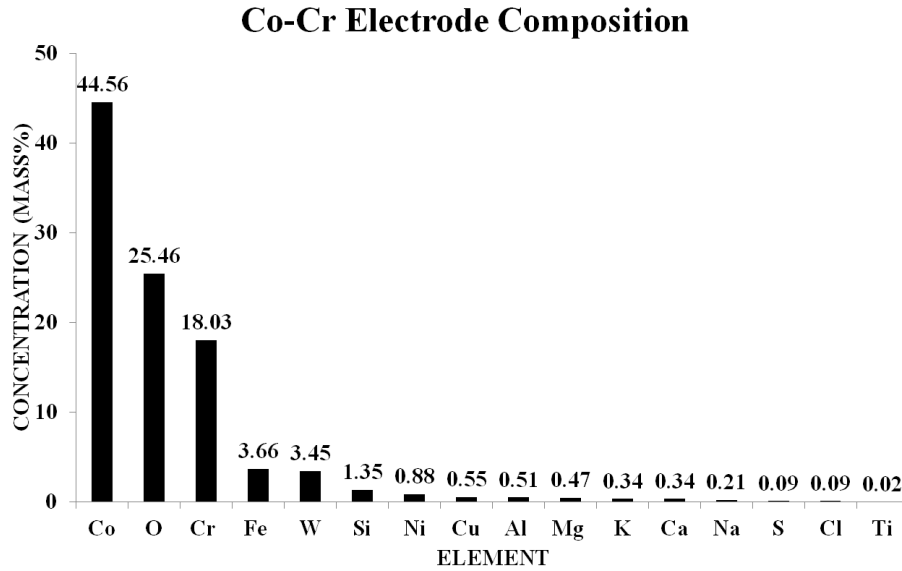
Figure 23 Chemical composition of the Co-Cr cathode.

The cathode was composed approximately by 44% cobalt (Co), 18% chromium (Cr), 4% Fe, 25% O, and traces of other elements such as Si, Al, Mg, Na, wolfram (W), copper (Cu), and sulphur (S).

The solution as well, was analysed in order to obtain a clear chemical composition, thus deposited dry residue was extracted from 500 ml of solution and its composition was measured. Table 3 summarizes the results of the EDX spectroscopy compositional analysis conducted on the dry deposited residue. The aqueous solution of potassium carbonate salt (K_2CO_3+H_2O) had a solute (K_2CO_3) to solvent (H_2O) ratio of approximately 40 g/l.

Table 3 Composition analysis of dry deposited residue of the aqueous solution.

Element	Weight%	Atomic%	Compound%	Formula
C	13.02	22.05	47.72	CO_2
K	43.40	22.57	52.28	K_2O
O	43.58	55.38		
Totals	100.00	100.00	100.00	

As already mentioned, Energy Dispersive X-Ray Spectroscopy was performed in order to investigate the surface of the electrodes and its changes throughout the process of electrolysis. Proofs of connections between superficial changes of the electrodes and piezonuclear effects were explored. In particular, the powerful tools of the FESEM were used to acquire a series of images of the surface of the electrodes, in order to visually studying its alteration. As a matter of actual fact, Figure 24, Figure 25, Figure 26 and Figure 27 show specific images of the surface of both Co-Cr cathode and Ni-Fe anode.
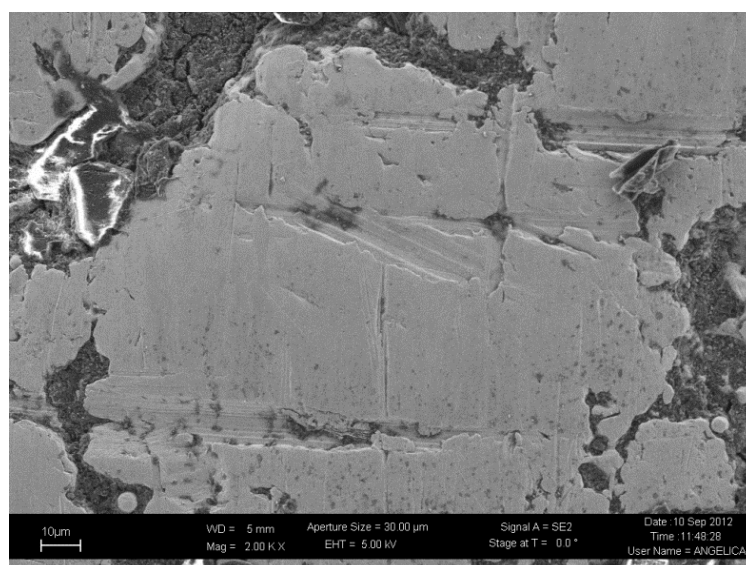
Figure 24 Portion of the Co-Cr electrode surface before the experiment.

The images were taken both before the experiment and after the exposure to the

process of electrolysis. Technical details of the images are reported on the black stream at the bottom of each figure.

In Figure 24, the image of the surface of the Co-Cr electrode was taken by means of the FESEM prior subjecting it to the electrolysis process. In Figure 25, the external surface of the electrode after several hours of exposure presented a rougher conformation and more evident micro-cracks. Figure 24 shows a surface generally smoother than that of Figure 25, with very few localized micro-cracks. After the exposure to the electrolysis the surface of the cathode appears to be strongly altered by the process: a trench with an evident micro-crack at its bottom is displayed in Figure 25.
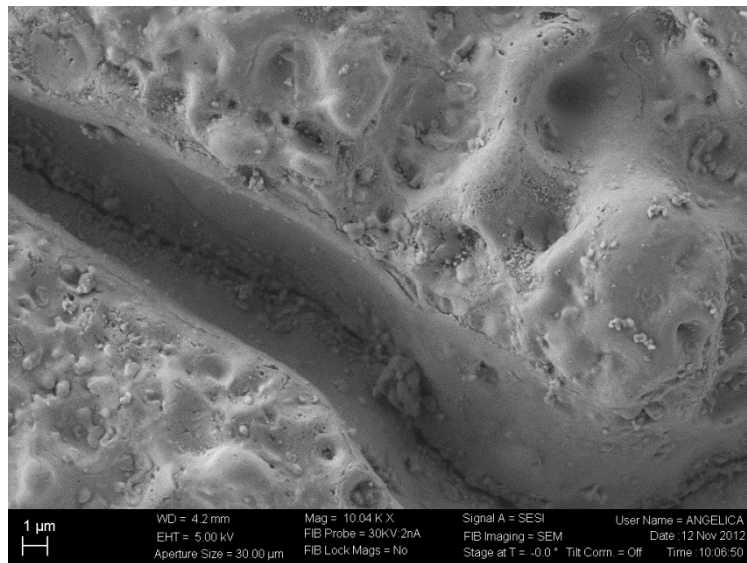
Figure 25 Portion of the external surface of the Co-Cr electrode after electrolysis.

The Ni-Fe anode presented similar and more evident alterations that are observable comparing Figure 26 to Figure 27. After many hours of exposure to the electrolytic process the morphology of the Ni-Fe surface was severely altered. Moreover, evident microcracks were diffused over the whole surface of the anode (Figure 27).
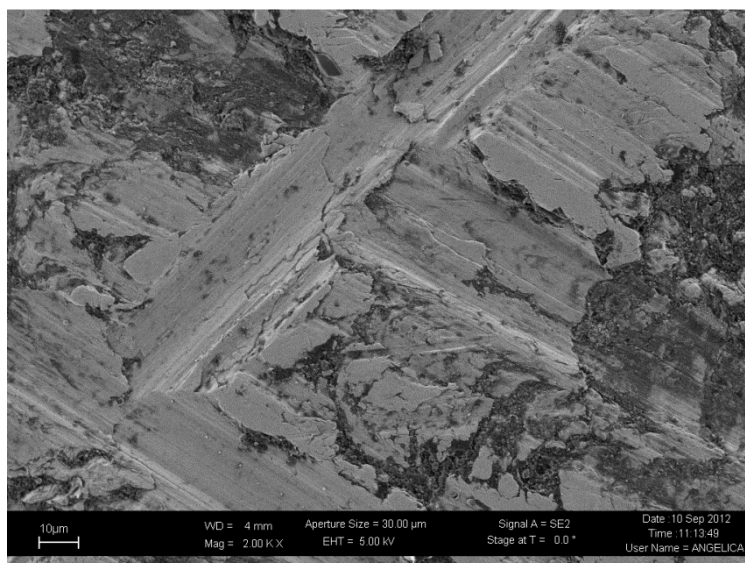
Figure 26 Surface of a portion of the Ni-Fe electrode.
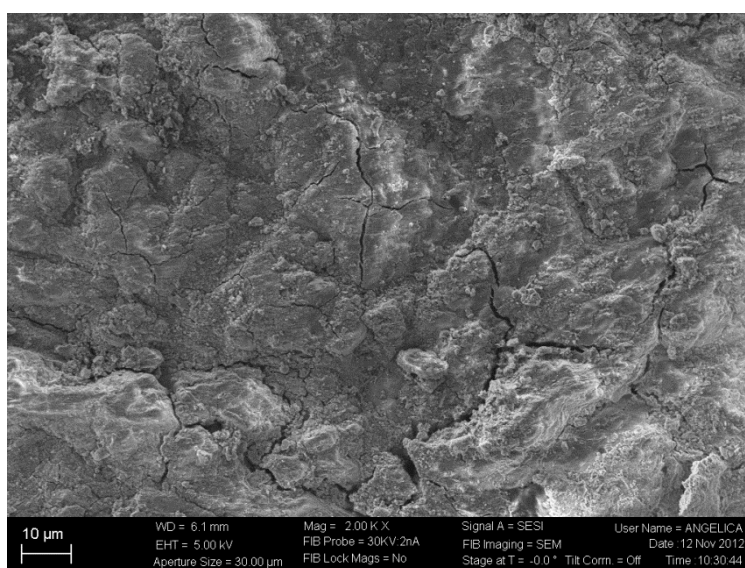
Figure 27 Surface of the Ni-Fe electrode after electrolysis.

The duration of the electrolytic process was broken into three different phases in order to better investigate possible compositional variations on the electrodes' surface. Table 4 summarizes the average concentrations of the most important elements identified on the surface of the anode at each phase.

Table 4 Average mass concentration of the elements composing the Ni-Fe electrode.

	Ni (%)	Si (%)	Mg (%)	Fe (%)	Cr (%)
Before the experiment	43.9	1.1	0.1	30.5	-
After 4h	43.6	1.1	0.4	30.7	-
After 32h	35.2	5.0	0.2	27.9	-
After 38h	35.3	1.5	4.8	27.3	3.0

Average concentrations of Ni, Si, Mg, Fe, and Cr are reported in detail: the electrodes' composition was investigated through different EDX measurement sessions, that is, before the experiment, after 4 hours, after 32 hours and after 38 hours of electrolysis. The first analysis was carried out to evaluate the composition of the electrodes before they underwent the electrolysis experiment (0 hours), (Table 4). The second analysis was conducted after an initial operating time of the electrolytic cell of four hours. After this, a third and a fourth step analyses were performed. For these two steps, the cell operated for 28 and 6 hours respectively, corresponding to a cumulative working time of 32 (4h+28h) and 38 hours (4h+28h+6h) (see Table 4).

Figure 28 summarizes the mass concentration percentages of nickel measured on local spots of the surface of Ni-Fe anode. The measures are displayed on the y-axes as a percentage of the total concentration of elements measured on precise spot of the Ni-Fe electrode. On the x-axes the spots investigated are labelled by a numbers from 1 to 15, being the spots 1 to 5, 6 to 10 and 11 to 15 chosen in regions of interest respectively around the tip, in the centre and above the base of the electrode. Two series of measures are shown corresponding to the condition before the experiment (in black) and after 38 hour of electrolysis (in red): fifteen points are indicated for each series along with the relevant average value M and standard deviation σ.
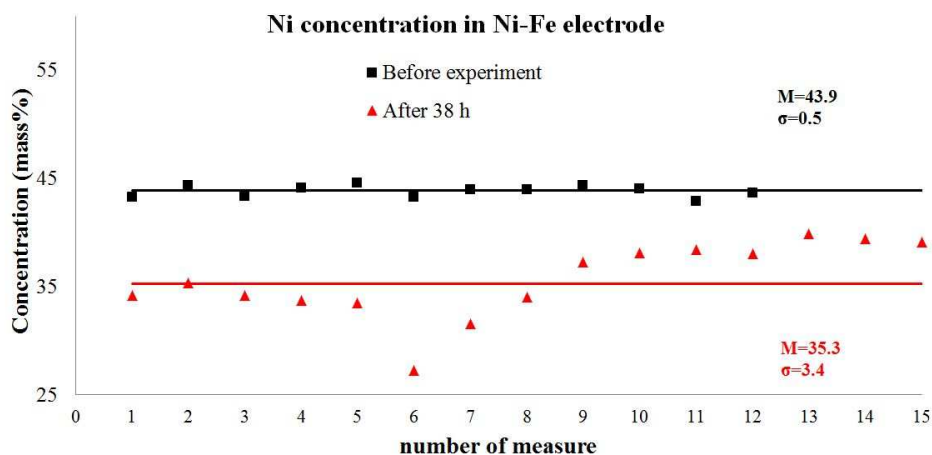
Figure 28 Local measures of nickel concentration on the Ni-Fe electrode.

Figure 29 shows the measures of Si concentration taken on local spots across the electrode surface.
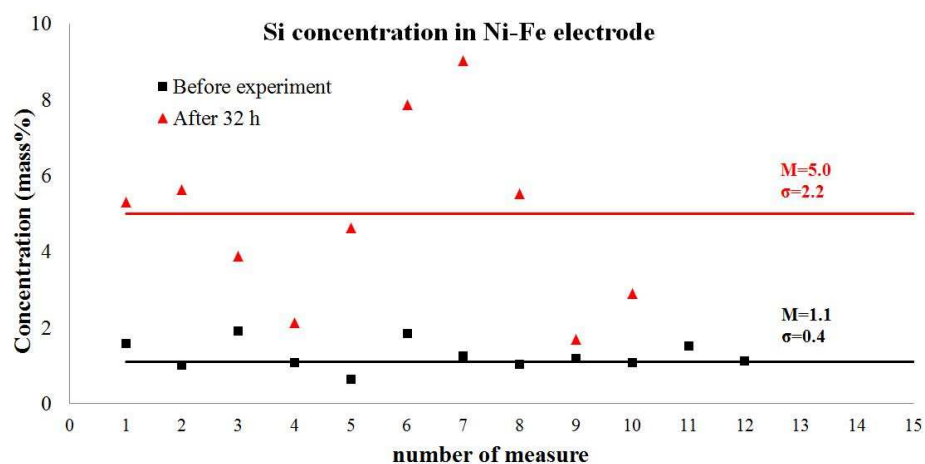
Figure 29 Local measure spots of Si concentration.

Standard deviation σ and relevant average concentration M and are indicated with the latter displayed as a straight line. Also in this case, the series in black

corresponds to the points measured before the experiment, and the one in red to those taken after 32 hours of electrolysis.

Figure 30 reports the Mg concentration measured on local points spread over the surface of the anode.
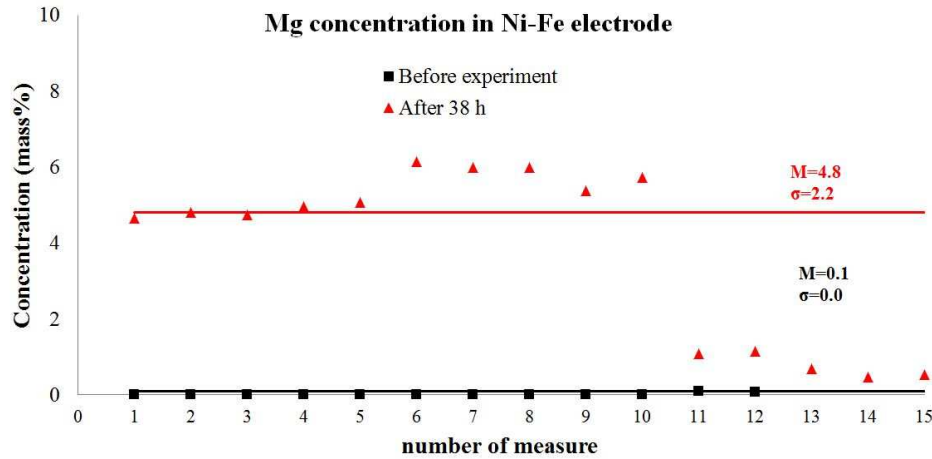
Figure 30 Local Measure spots of Mg concentration.

The measures are expressed in percent mass concentration. Two series are displayed: the black one comprising the spots acquired before the experiment and the red one concerning fifteen measures conducted after 38 hours of electrolysis. Average concentration M of each series is represented again as a straight line and the standard deviation σ is indicated.

Analogously, Figure 31 shows the points with iron concentration acquired on the surface of the electrode. Also in this case the black and red series were taken respectively before and after the exposure to all 38 hours of electrolysis. The average M of each series is shown again together with the standard deviation σ.
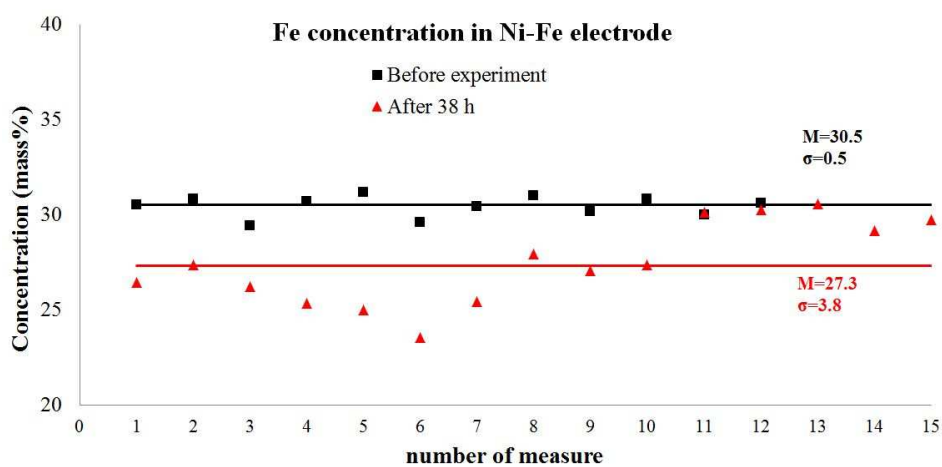
Figure 31 Series of measures of Fe concentration.

Figure 32 reports the evolution of Cr concentration taken on the surface of the Ni-Fe electrode after 38 hour of exposure to electrolysis.
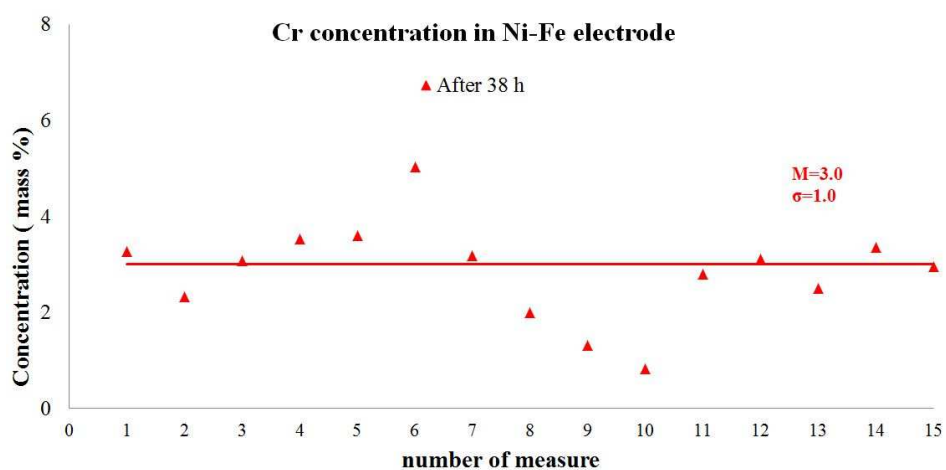
Figure 32 Series of fifteen measures of Cr concentration.

The measures from 1 to 5 were taken on the surface of the upper part of the electrode (close to the tip); from 6 to 10 were taken on the central part of the

electrode; the last five were acquired on the surface of the lower portion, close to the threaded surface.

In the APPENDIX, more detailed graphs of EDX measurements for each element illustrated above are reported (Figure 64, Figure 65, Figure 66, Figure 67 and Figure 68). The evolution of their local (series of 15 spots) and average concentrations (histograms) with relative standard deviations was investigated at different stages of the electrolytic process: before the experiment (0 hours), after 4, after 32, and after 38 hours of electrolysis.

Considering the overview of the variation of chemical composition of the Ni-Fe anode reported in Table 4, interesting observations could be made. Firstly, the Ni concentration showed a total average decrease of 8.6% from 43.9% to 35.3% after 38 hours (see Table 4 and Figure 28). This Ni depletion is one fourth of the initial Ni concentration.

Secondly, an average increment in Si concentration after 32 hours of 3.9% (Figure 29) and an average increment in Mg concentration after 38 hours (Figure 30), starting from 0.1% up to 4.8%, can be observed from the data reported in Table 4.

Similar considerations may be done also for Fe concentrations. The average Fe content decreased of 3.2%, changing from 30.5% to 27.3% at the end of the experiment (Table 4 and Figure 31).

On the other hand, one of the most evident features is the appearance of Cr, before absent on the nickel-iron electrode, as reported in Figure 32. Cr concentration appeared only in the last phase, after 38 hours of electrolysis, with an appreciable increase of 3.0% (see Table 4).

The decreases in Ni and Fe seem to be almost perfectly counterbalanced by the increases in other elements: Si, Mg, and Cr. In particular, since the analysis excluded any Ni content variations on the other Co-Cr cathode, the following interpretation of the data could be considered. A relationship involving Ni, Si and Mg was conjectured: *Ni (−8.6%) ⟹ Si (+3.9%) + Mg (+4.7%)*. Under the light of the neutron and alpha emission detected, such relation could be reasonably explained admitting a contribution from the following symmetrical piezonuclear fission reactions:

$$\mathrm{Ni}_{28}^{58} \rightarrow 2\mathrm{Si}_{14}^{28} + 2 \text{ neutrons} \qquad\qquad 3.1$$

$$\mathrm{Ni}_{28}^{58} \rightarrow 2\mathrm{Mg}_{12}^{24} + 2\mathrm{He}_2^4 + 2 \text{ neutrons} \qquad\qquad 3.2$$

At the same time, another correspondence could be observed: *Fe (−3.2%)* ⟹ *Cr (+3.0%)*. This could be explained either by considering a galvanic effect of the electrochemical process, either associating it to the following reaction:

$$\mathrm{Fe}_{26}^{56} \rightarrow \mathrm{Cr}_{24}^{52} + \mathrm{He}_2^4 \qquad\qquad 3.3$$

It is very interesting to point out that reactions 3.1 and 3.2 imply neutron emission, whereas, reactions 3.2 and 3.3 imply alpha particle (nuclei of helium He) emissions. Such implications result theoretically consistent to the neutron and alpha emission events recorder throughout the experiment. Thus, the nuclear phenomena might have plausibly contributed to the variation of the composition of the Ni-Fe anode.

As far as the Co-Cr electrode is concerned, it was possible to observe even more evident variations in the concentrations of the most abundant constituting elements. Table 5 summarizes the average mass concentration of the most notable elements identified on the cathode. The data reported in the table correspond to four different steps of compositional measurement: before the experiment, after 4 hours of electrolysis, after 32 hours and at the end of the electrolytic process after 38 hours of experimentation.

Table 5 Average concentration of elements constituting the Co-Cr electrode.

	Co(%)	Fe(%)	Cr(%)	K(%)
Before the experiment:	44.1	3.1	17.8	0.5
After 4h	43.7	1.6	17.8	2.2
After 32h	20.6	26.3	9.7	12.9
After 38h	34.4	6.6	5.1	4.4

Figure 33 shows in detail the evolution of Co concentration measures before the electrolysis (in black) and the after 32 hours (in red).
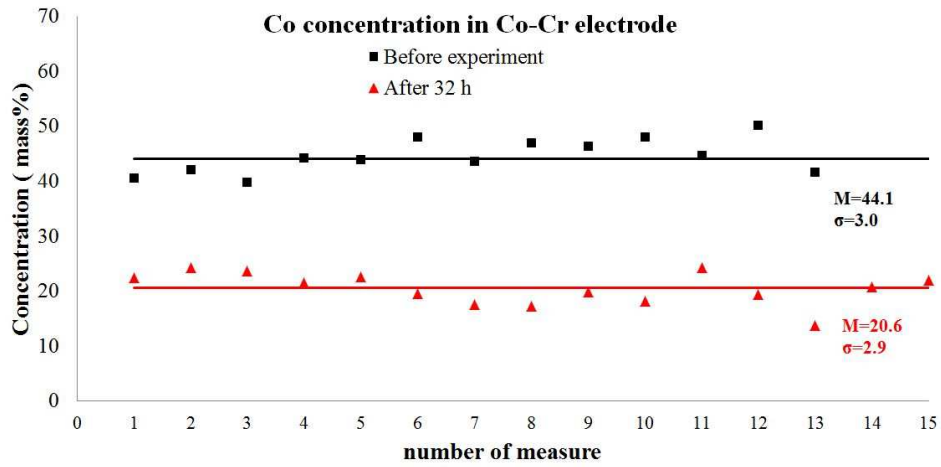
Figure 33 Series of measures of Co concentration on the Co-Cr electrode.

Figure 34 and Figure 35 show analogous results concerning the evolution of concentrations of respectively Fe and Cr on the Co-Cr cathode.
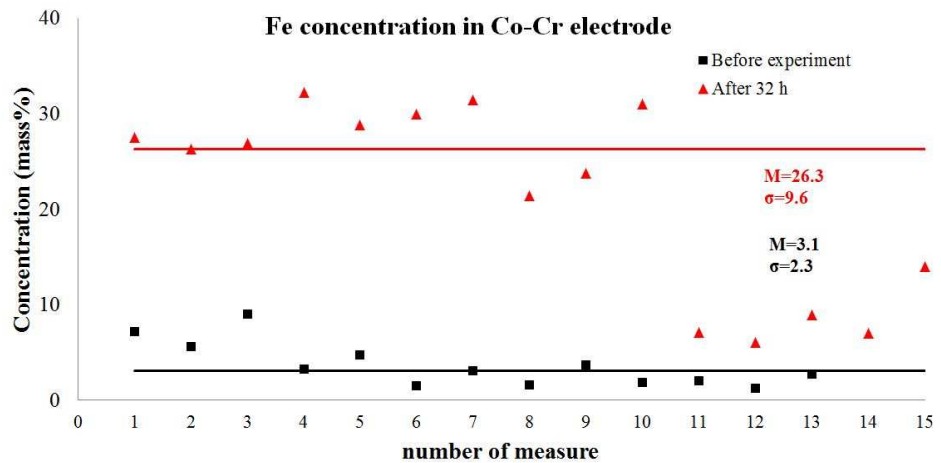
Figure 34 Series of measures of the Fe concentration on Co-Cr electrode.

In each figure the evolution of concentrations measured before the experiment and after various hours of electrolysis is reported.
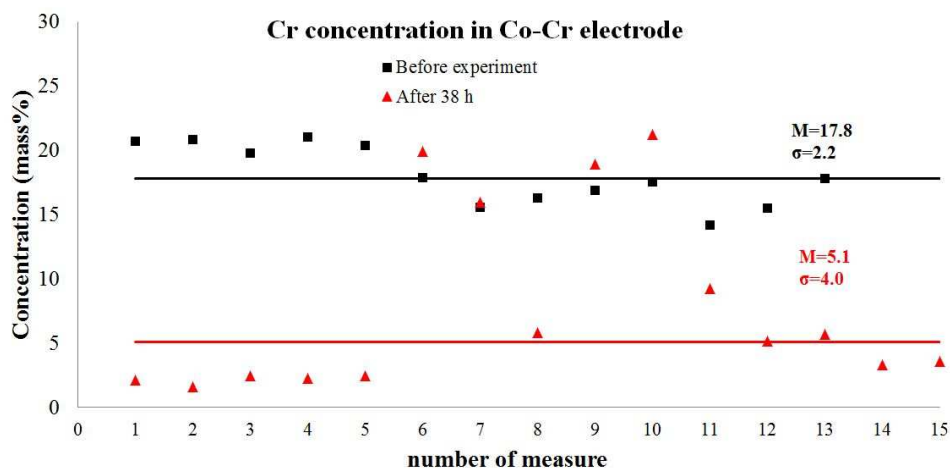
Figure 35 Series of measures of the Cr mass concentration on the Co-Cr cathode.

Figure 36 shows the presence of K concentration after various hours of electrolysis.
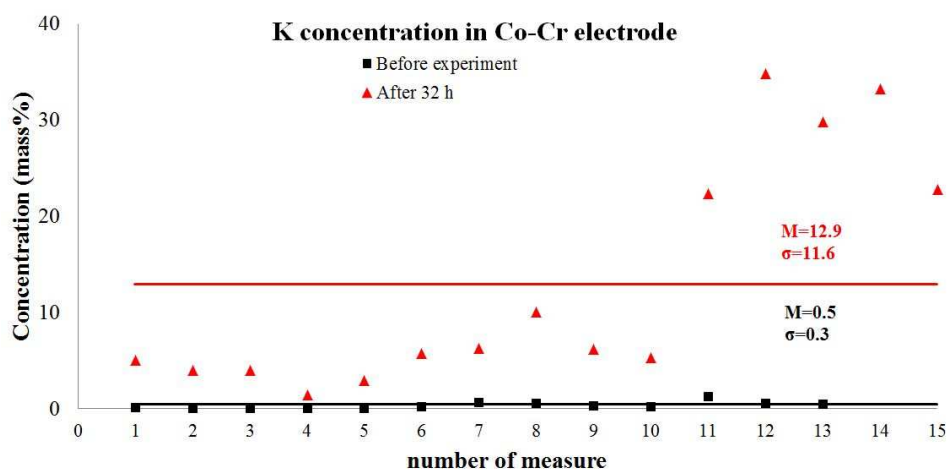
Figure 36 Measures of the K concentration before the experiment and after 32 hours.

In the APPENDIX, details of the evolution of concentration of elements constituting the Co-Cr electrode at different stages of the experiment are displayed

(Figure 69, Figure 70, Figure 71 and Figure 72).

Considering the variation overview of the cathode composition reported in Table 5, also in the case of the Co-Cr electrode interesting observations were made. First of all, it was noticed that the average Co concentration decreased by 23.5%, from an initial percentage of 44.1% to a concentration of 20.6% after 32 hours (Figure 33).

At the same time an increment of 23.2% was observed in the Fe content after 32 hours, changing from 3.1% before the experiment to 26.3% at the end of the second phase (see Table 5 and Figure 34).

It is rather impressive that the decrease in Co and the increase in Fe are comparable considering the following relationship: *Co (−23.5%) ⟹ Fe (+23.2%).* According to the compositional analysis on the Ni-Fe electrode no Co concentration was found on the anode that could lead us to consider the chemical migration to explain its depletion in the Co-Cr electrode. Hence, the relationship expressed above could be associated to the following reaction:

$$Co_{27}^{59} \rightarrow Fe_{26}^{56} + H_1^1 + 2 \text{ neutrons} \qquad\qquad 3.4$$

This nuclear transformation contributes to explain the variation in Co and Fe content on the cathode and it is theoretically consistent to the neutron emission peaks detected during the experiment.

Examining the data in Table 5, Figure 35 and Figure 36, it was noticed that Cr and K local and average concentrations vary throughout different phases of the experiment. The Cr average concentration decreased of about 8.1% after 32 hours of experiment. Such variation associated to the appearance of Cr on the anode could be explained as the result of a galvanic effect of the electrochemical process.

Additionally, the K concentration increased by about 12.4% after 32 hours. This could likely be an effect of deposition of K_2CO_3 constituting the aqueous solution.

However, Cr and K variations could be studied from another point of view. The decrease in Cr concentration (8.1%) on the cathode partially counterbalanced the increment in K with an exceeding 4.3% variation. Hence, the possibility of a contribution of K coming from a nuclear transformation was considered. The following piezonuclear reaction involving Cr as the starting element and K as the resultant was conjectured:

$$Cr_{24}^{52} \rightarrow K_{19}^{39} + He_1^1 + 2He_2^4 + 4 \text{ neutrons} \qquad\qquad 3.5$$

It is important to remark that both reactions 3.4 and 3.5 imply neutron emission, while reaction 3.5 alone implies also the emission of alpha particles, which is theoretically consistent to the experimental proofs of nuclear emission reported in the previous section. It is also important to reconsider the relationships observed for Ni-Fe anode (associated to reactions 3.1, 3.2 and 3.3) and for Co-Cr cathode (associated to reactions 3.4, 3.5). They were obtained considering the values of the second or third EDX measure session corresponding to the larger variation for each element concentration (Table 4 and Table 5).

Additional variations observed for some of these elements, such as Si, Co and Fe, between the second and the third session of measures could be explained considering other secondary effects and possible piezonuclear reactions occurring in the metal electrode lattice. Supplementary efforts devoted to evaluate the evidence of secondary fission transformations were in progress by Professor Carpinteri research team at the moment of the writing of this thesis.

All the results and visual proofs listed upon until now suggested that in hydrogen rich environments such as electrolytic ones, the host metal lattice of electrodes was subjected to mechanical damaging and fracturing due to HE caused by H atoms absorption and penetration in the metal. Clear proofs of a diffused cracking were identified on the electrode surface after the experiments (see Figure 24 and Figure 25, Figure 26 and Figure 27). According to such considerations, the author argued that hydrogen, favouring the crack formation and propagation in the metal, comes from the electrolysis of water. In fact, being the electrodes immersed in a liquid solution, their surface is exposed to the formation of gaseous hydrogen especially at the cathode due to the decomposition of water caused by the current passage. More in detail, such cracking process was responsible for triggering nuclear effects that were identified through variation of chemical composition and nuclear emission detection.

3.4 Comments and experimental issues about equipment and measures

It is important for the sake of science to provide a brief overview of the issues encountered regarding equipment and measurement.

First of all, after setting the rig and the instruments, a particular problem came

up during the initial hours of electrolysis. Specifically, the container of the cell underwent cracking in the first 5 hours of use of the cell and the liquid solution inside started leaking. Such problem forced the author to disrupt the experiment and substitute the container of the cell. The first reaction chamber was made of high resistance Pyrex glass. However, it seemed reasonable to assume that it could not withstand the variation of temperature involved in the electrolysis process and so it cracked. Such outcome forced the author to change the reaction chamber and use a more resistant one made out of steel.

Another minor issue was related to the process of filling the electrolytic cell. In particular, the equipment was set so that the cell could be filled only manually. When the cell was powered and the voltage difference induced the electrolysis, the temperature of the liquid gradually rose up to the boiling point. Hence, gas was generated due to the electrochemical process and to the change of phase. As the gas was collected in an external reservoir, the cell slowly emptied. Thus, in order to keep the electrodes always immersed in the solution and keep the process going it was necessary to manually refill the cell with liquid solution when the level was too low.

On the other hand, it is important to spend few more words on the difficulties related to the acquisition of the chemical composition of the electrodes. A slight inconvenience was also encountered when elaborating the numerous data concerning the chemical analyses. The latter were conducted measuring the local composition of specific spots chosen all over the surface of the electrodes. The first difficulty was related to the choice of the regions of interest that had to be investigated on the electrodes surface. Specific chemical characterizations were made on local spots spread on the surface. A second inconvenience was the choice of how many spots were to be considered in order to collect a statistical reliable amount of data. For this reason series of fifteen points were elaborated in order to assess the local evolution of the concentration of each noteworthy element identified on the electrode. However, certain series represented in the graphs reported in the previous section and in the appendix have less than fifteen points. This is explained thanks to the fact that in some specific spots no concentration of the element under investigation was detected.

Chapter 4

4 MECHANICAL INTERPRETATION OF NUCLEAR EFFECTS IN ELECTROLYSIS EXPERIMENTS WITH PALLADIUM CATHODE

The experiments described in Chapter 3 were characterized by remarkable neutron and alpha particle emission, together with appreciable variations of the chemical composition of the electrodes. Taken for granted the electrolytic phenomenon and the relative effects, the results were explored from the perspective of the piezonuclear approach. A mechanical reason for the so-called Cold Nuclear Fusion was worth considering. The hydrogen embrittlement due to H atoms produced by the electrolysis played an essential role in the observed crack propagation in the material of the electrodes. In particular, it affected the nuclei of the elements composing the host metals (Pd, Ni, Co). Consequently, the hypothesis was that piezonuclear reactions occurred in correspondence with the micro-crack formation. In order to repeat the results obtained with Co-Cr and Ni-Fe electrodes, electrolytic tests have been conducted using different metal electrodes: 100% Pd cathode and Ni-Ti alloy anode. As in the first experimental campaign, also in this second campaign compositional changes and traces of elements before absent were studied on both Pd and Ni electrodes after the process of electrolysis. NE was monitored once again by means of the same equipment as it is described in Chapter 1, section 1.4 "Evidence of neutron emission related to fracture phenomena: from the laboratory to the earth crust scale".

It is necessary to mention that throughout this second experimental campaign current intensity and voltage were not monitored as the focus was not on the energy consumption and production, but rather on the mechanical and chemical alteration of the electrodes. Nor the alpha particle emission was monitored as an appropriate alpha detector was not available at the moment of conducting this campaign. Moreover, the analysis of the Pd cathode was given higher priority in order to explore and broaden the hydrogen embrittlement effects connected to nuclear products. This is also justified by the fact that during electrochemical processes such as that one under investigation the cathodic polarisation environment is the one region of interest where gaseous hydrogen is formed.

4.1   Neutron emissions measurements

Neutron emission measurements performed during the experimental activity are represented in Figure 37.
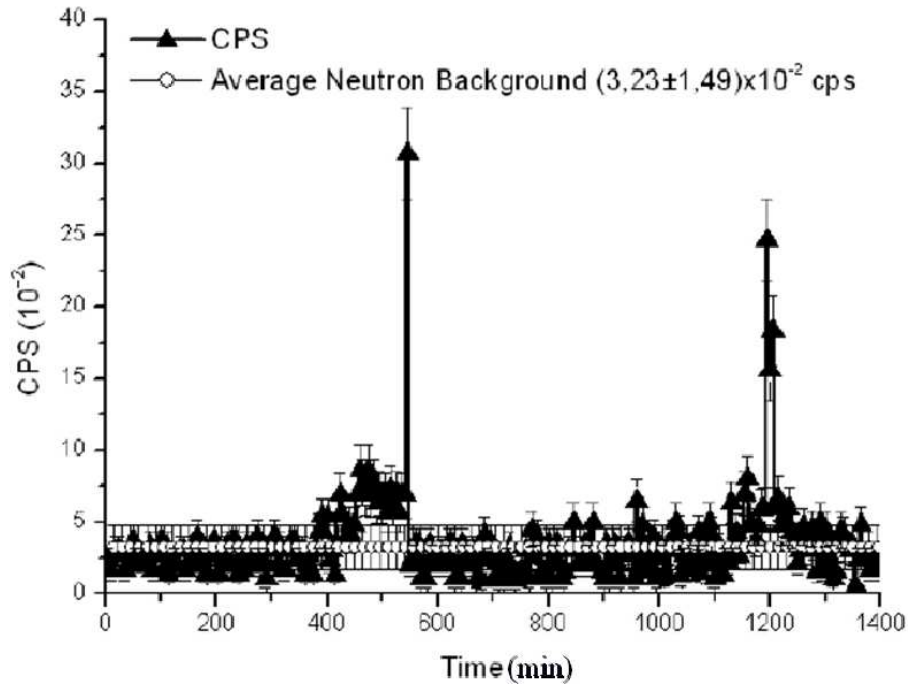
Figure 37 Neutron Emission measurements.

Emissions between 3 and 10 times the background level were observed during the experiment. The measurements performed by the He^3 detector were conducted for a total time of about 24 hours. The background level was measured for different time intervals before switching on and after switching off the reaction cell. These measurements reported an average neutron background of about $(3.23\pm1.49)\times10^{-2}$ cps. Furthermore, when the reaction chamber was active, it was possible to observe that after a time interval of 460 minutes neutron emissions about 3 times higher than the background level were recognized. After 545 minutes from the beginning of the measurements, it was possible to observe a neutron emission level of about one order of magnitude greater than the

background level. Similar results were observed after 1200 minutes when neutron emissions up to 7 times the background were measured. The detection of such peaks of neutron emission suggested that also in this case nuclear phenomena were involved during the electrolytic process.

4.2   Compositional analysis of electrodes: palladium cathode

In this section an analysis of chemical compositions taken before and after the experiments is considered. The author in collaboration with Professor Carpinteri research team studied as well the evolution of local and average concentrations of each element identified on the surfaces of the two electrodes. Moreover, observations of surface alteration of the cathode (Pd electrode) are presented below as it was already done in the first experimental campaign in Chapter 3. Firstly, features and considerations concerning the Pd electrode were taken into account. Subsequently, comments about the anode (Ni-Ti alloy electrode) were elaborated as dealt with later on in next section.

Results of EDX analyses conducted on the Pd electrode are summarized in Table 6. Average concentrations of elements found on the cathode before and after the electrolysis (20 hours) were compared.

Table 6 Composition of Pd electrode.

Element	AVERAGE CONCENTRATION		AVERAGE VARIATION
	Before the Experiment (%)	After 20 hours (%)	(negative for decrease) (%)
O	0.0	18.5	+18.5
Na	0.0	0.2	+0.2
Mg	0.0	1.0	+1.0
Al	0.0	0.4	+0.4
Si	0.0	1.1	+1.1
K	0.0	1.5	+1.5
Ca	0.0	0.2	+0.2
Cr	0.0	0.5	+0.5
Fe	0.0	2.0	+2.0

Co	**0.0**	**0.2**	**+0.2**
Cu	**0.0**	**3.0**	**+3.0**
Pd	**100.0**	**71.3**	**−28.6**

A detailed imaging analysis was conducted on the palladium cathode thanks to the FESEM. Images and macro images of the surface of the electrode were acquired after the electrolysis and they are illustrated in Figure 38, Figure 39 and Figure 40.
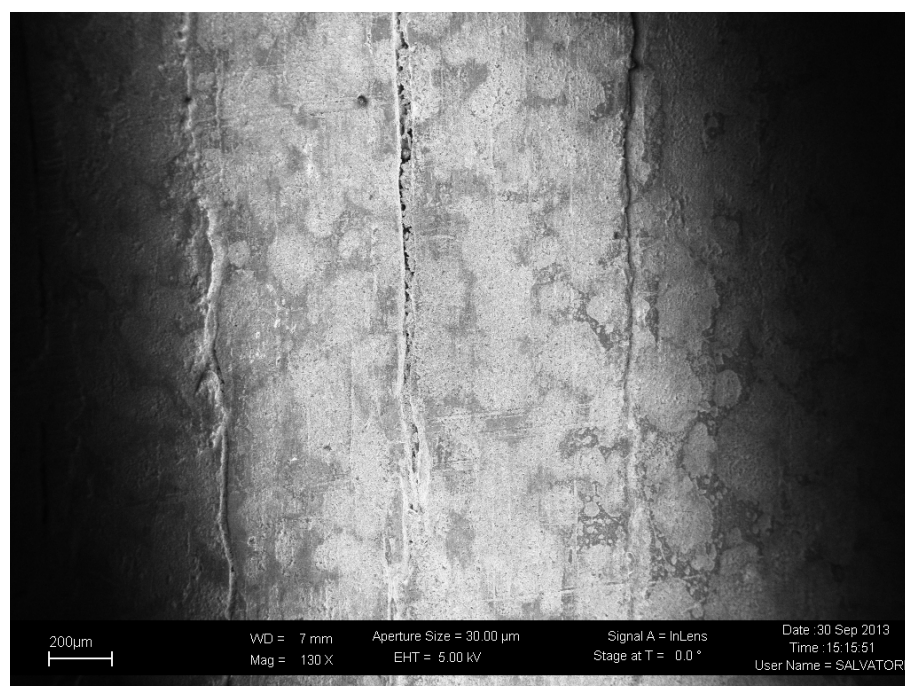
Figure 38 Image of the surface of the Palladium electrode.

Proofs of cracking were particularly strong in the case of the Pd electrode, where a major fracture took place after the tests. As a matter of fact, a remarkable longitudinal crack formed on the surface of the cathode after more than 20 hours of electrolysis. The crack opening was more than than 40 μm wide and it was visible to the naked eye (Figure 40).
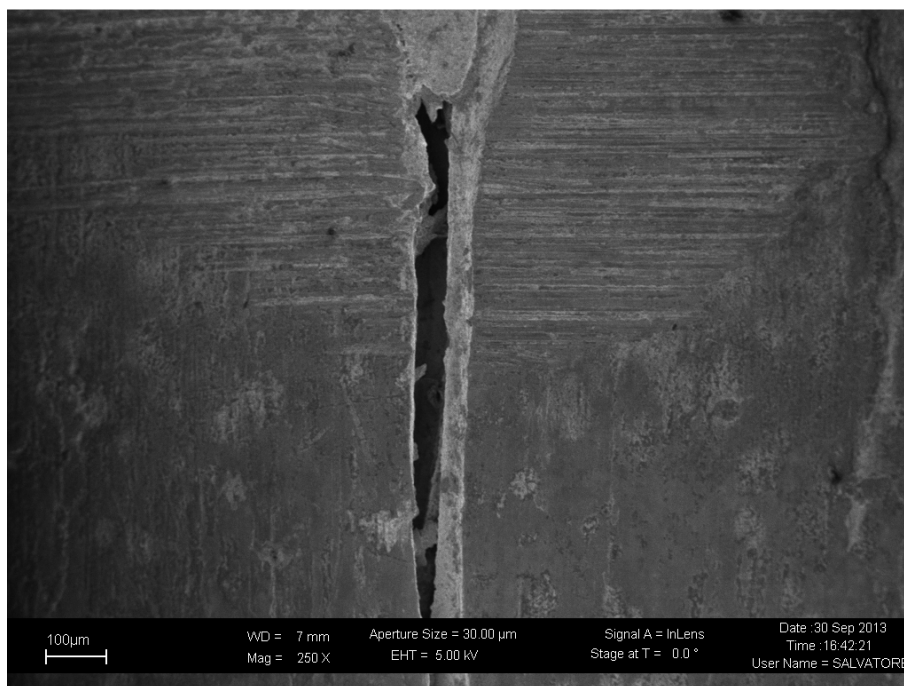
Figure 39 Longitudinal crack found on the cathode.

Under the light of neutron emission peaks measured, assuming hydrogen embrittlement occurred at the cathode and on the basis of previous studies of Carpinteri et al., the evident microcracking of the cathode surface was accounted for to explain the whole process through a mechanical interpretation of the phenomena. The idea underlying such interpretation was that the damaging and cracking of the palladium electrode triggered nuclear reactions contributing to the chemical variations of the composition of the electrode itself. These considerations found confirmation in the experimental results of the EDX spectroscopy analyses. Proposed reactions are listed later on in this section associated to the chemical variations of the elements found on the electrode after the electrolytic process.
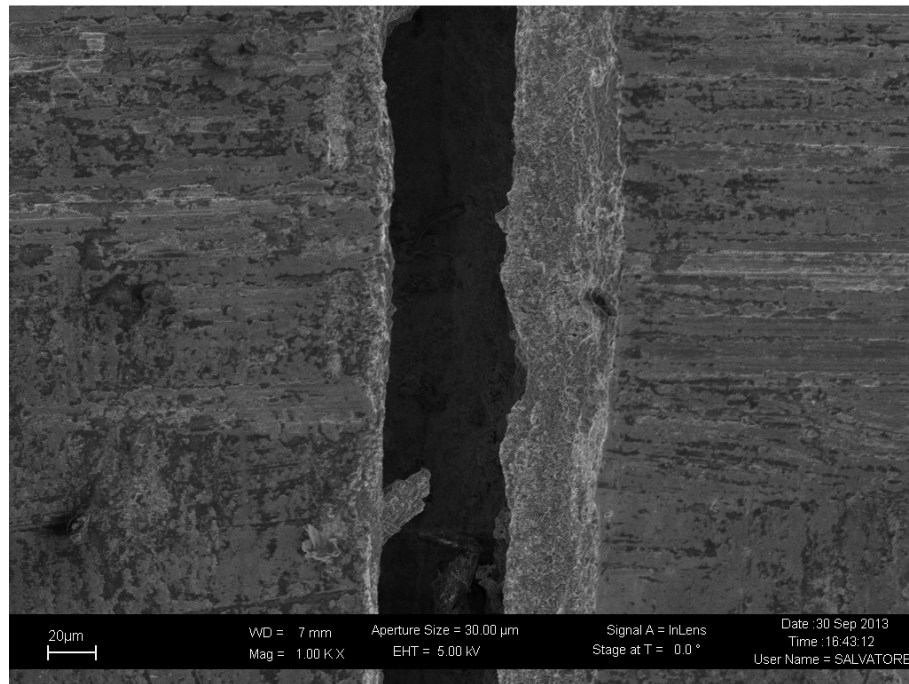
Figure 40 Magnified zoom of the microcrack.

Figure 41 reports the series of measures conducted to assess the evolution of Pd local concentration measured in precise spots spread across the cathode surface. Fifteen different points of the surface have been studied. Pd concentration taken before the experiment (in black) was compared to that taken after the electrolysis (in red); the average concentration M (straight horizontal line) and the corresponding standard deviation σ are reported in the figure.
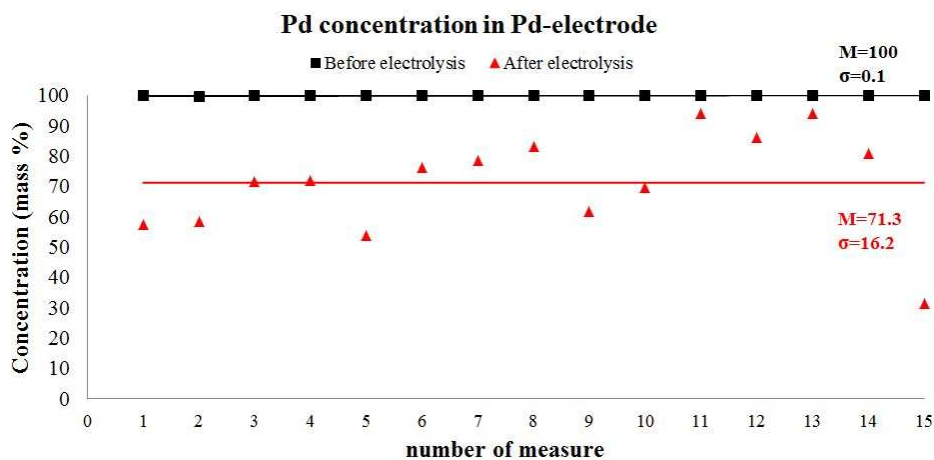
Figure 41 Series of measures of Pd concentration in Pd electrode.

Figure 42 shows that on the cathode no Fe concentration was detected before its use in this experimental campaign. Only after 20 hours of electrochemical process the EDX analysis revealed the presence of Fe on the Pd electrode.
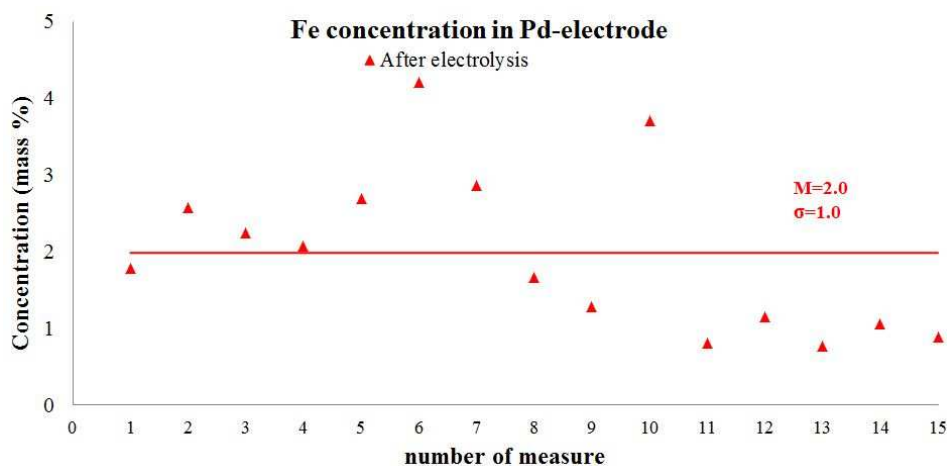
Figure 42 Fe concentrations measured on the electrode surface after the electrolysis.

Other elements were detected on the cathode surface only after the

electrochemical process. These elements are calcium, oxygen, magnesium, silicon and potassium.

Figure 43 summarizes some results showing very feeble traces of Ca revealed on the cathode. Interesting peaks were detected although the average concentration of Ca after the experiment is quite low.
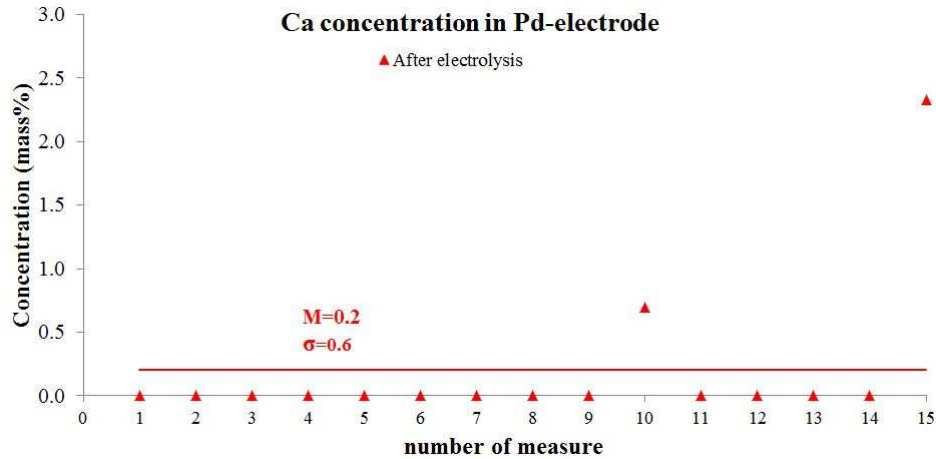
Figure 43 Traces of Ca concentration have been detected after the electrolysis.

The series of data represented in Figure 44, on the other hand suggested that the oxygen deeply interacted with the Pd electrode. The presence of the Oxygen was remarkable after the experiments. Although, the standard deviation is quite high, the average concentration of oxygen measured in fifteen local spots reaches 18.5 %.
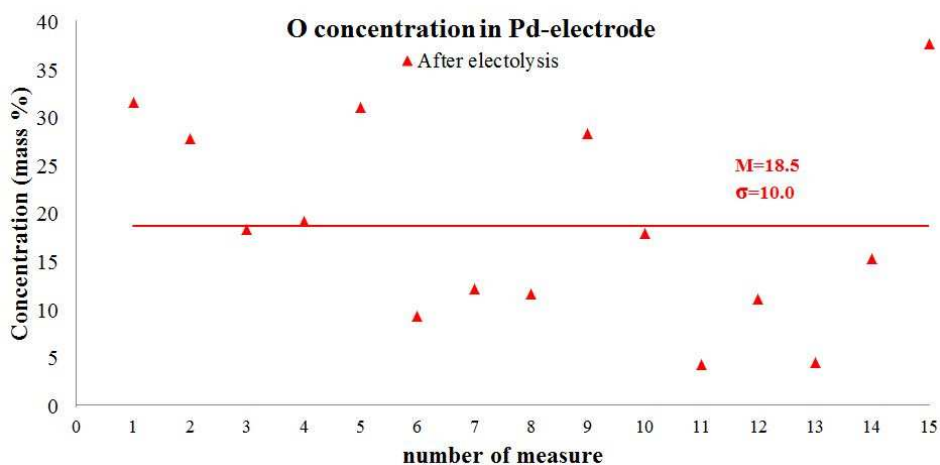
Figure 44 Series of measures of O concentration.

In Figure 45 it is possible to read the values of Mg concentration measured on the Pd electrode. The magnesium presence on the cathode was evident after the experiment, while there was no trace of it before the experiment.
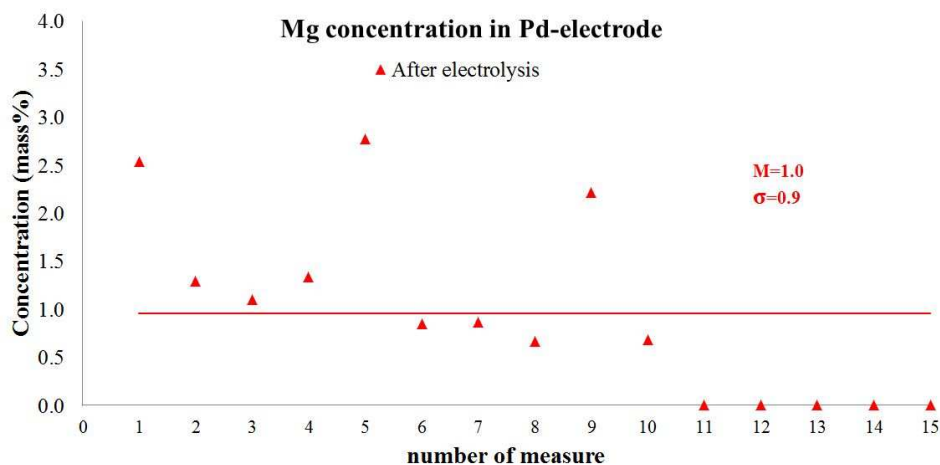
Figure 45 Series of measures of Mg concentration on Pd electrode.

Traces of potassium and silicon were also found as it is described in Figure 46 and

Figure 47 respectively. EDX results of Si concentration resulted in a value of standard deviation higher than the average concentration of silicon itself. This was due the anomalous peak concentration corresponding to point 15.
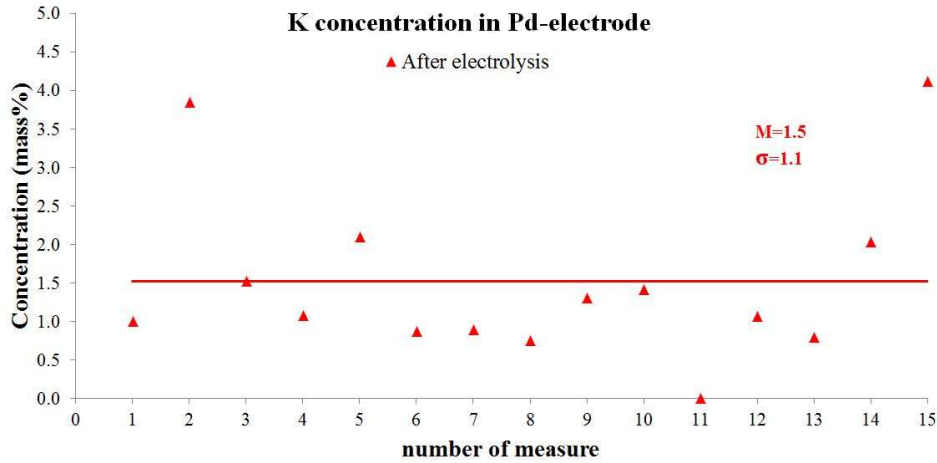
Figure 46 Potassium concentrations have been detected only after the experiment.
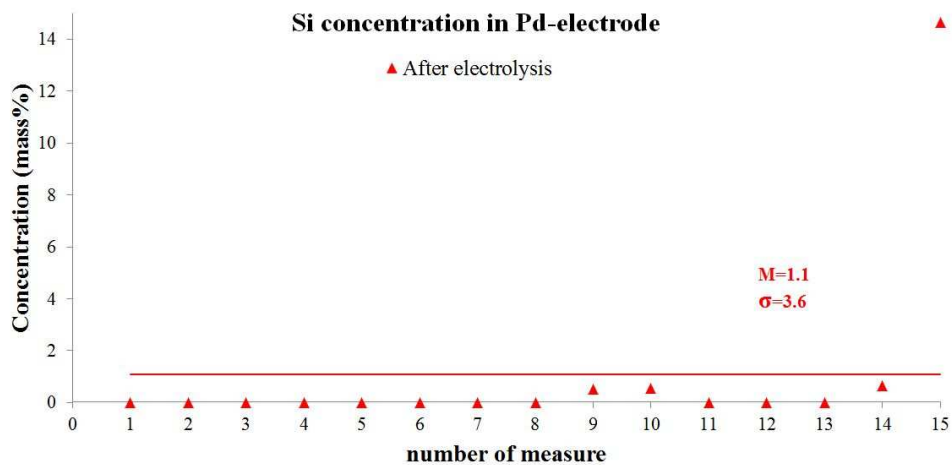
Figure 47 Traces of Si concentration in Pd electrode.

Analyzing the overview listed in Table 6, specific considerations were made in

order to interpret the data. First of all, it was noticed how remarkably the global average concentration of Pd decreased (-28.6 %) throughout the electrolytic process. Such variation was associated to the following reaction:

$$Pd_{46}^{106} \rightarrow Ca_{20}^{40} + Fe_{26}^{56} + 10 \text{ neutrons} \qquad\qquad 4.1$$

According to reaction 4.1 the average Pd decrease should have been counterbalanced by increments in Ca and Fe concentration corresponding respectively to 10.8% of Ca and 15.1% of Fe accompanied by a remaining quantity of 2.3 % of the mass concentration equivalent to the released neutrons.

Secondly, the whole iron increase, hypothesized according to reaction 4.1, could be entirely considered as mother element involved in a transformation for the production of other elements. Hence, a second nuclear reaction was proposed involving Fe as mother element and O as daughter product together with alpha and neutron emission:

$$Fe_{26}^{56} \rightarrow 3O_8^{16} + He_2^4 + 4 \text{ neutrons} \qquad\qquad 4.2$$

According to reaction 4.2 the Fe depletion produced about 12.9 % of O with alpha particles (nuclei of helium He) and neutron emissions that are theoretically consistent with the NE measurements.

The average O concentration, before absent on the cathode, increased after 20 hours of experimental activity up to 18.5%, (Table 6 Composition of Pd electrode.), this quantity seemed to be partially counterbalanced by the formation of O coming from reaction 4.2. The remaining 5.6% of O concentration could be explained considering other reactions involving Ca (daughter product of reaction 4.1) as mother element:

$$Ca_{20}^{40} \rightarrow Mg_{12}^{24} + O_8^{16} \qquad\qquad 4.3$$

$$Ca_{20}^{40} \rightarrow 2O_8^{16} + 4H_1^1 + 4 \text{ neutrons} \qquad\qquad 4.4$$

The nuclear transformation 4.3 was associated to a decrease of Ca concentration of 1.6% and to the formation of 1.0 % of Mg and 0.6% of O. Furthermore, reaction 4.4 justified a decrease of Ca concentration equal to 5.9%, an increase of 4.7% in O concentration and 0.6% in H, corroborating the NE peaks

measured considering neutron release equal to remaining 0.6% in mass.

It is necessary to point out that the total O increase predicted by reactions 4.2, 4.3 and 4.4 is equal to 18.3% in mass. This is almost perfectly comparable to value of average O concentration equal to 18.5% experimentally measured through EDX spectroscopy on the Pd cathode at the end of the electrolytic process. Hence, the proposed reactions are theoretically consistent to the relative experimental evidence.

At the same time the Mg increase observed after the experiments can be explained by the results of reaction 4.3 (Table 6). According to reactions 4.3 and 4.4 the following relationships were considered: *Ca (−1.6 %)* $\Rightarrow$ *Mg (+1.0 %) +O (+0.6 %)*; *Ca (−5.9 %)* $\Rightarrow$ *O (+4.7 %) + H (+0.6 %) + neutrons (+0.6 %)*. Taking into account these transformations and considering the Ca increase predicted by reaction 4.1 (10.8%) a concentration of 4.3% of Ca was yet to be counterbalanced.

For such purpose, additional reactions involving Ca as mother element and Si, K and C as the daughter products were proposed:

$$Ca_{20}^{40} \rightarrow K_{19}^{39} + H_1^1 \hspace{5cm} 4.5$$

$$Ca_{20}^{40} \rightarrow Si_{14}^{28} + C_6^{12} \hspace{4.8cm} 4.6$$

The following relationships were associated to the reactions above: *Ca (−1.6 %)* $\Rightarrow$ *Si (+1.1 %) + C (+0.5 %); Ca (−1.5 %)* $\Rightarrow$ *K (+1.5 %)*.

Finally considering the formation of 0.2% of Ca measured after the experiment the total Ca increase predicted by reaction 4.1 could be perfectly counterbalanced. In fact, the average Ca decrease measured was equal to 10.8% and the total Ca involved by reactions 4.3, 4.4, 4.5 and 4.6 was 10.6% which gave a difference equal to 0.2 % equal to the final average Ca concentration measured. At the same time the variation of other elements predicted by the piezonuclear transformations proposed was confirmed by the measurements obtained after the experiments summarized in Table 6. In fact, they are consistent to the measured values of average variations of Mg (1.0%), Si (1.1 %) and K (1.5 %) (see Table 5Figure 45, Figure 46, Figure 47).

However, with regards to the iron, its average compositional increase (+2.0%) measured on the Pd electrode could be interpreted also as a galvanic effect, since it

is similar to the compositional Fe decrease (-2.0 %) measured on the Ni electrode as it is described in the next section. The presence of K concentration on the Pd cathode could as well be explained as deposition effect of the solute. Nonetheless, it is necessary to state for the sake of science that the presence of copper (Cu in Table 6) measured on the Pd electrode after 20 hours of experimentation could not be explained.

4.2.1   Analysis of nickel-titanium alloy electrode

Let us consider the nickel-titanium alloy electrode (anode). Table 7 lists the composition of the anode in terms of average mass concentration percentage of the elements found on the surface of the electrode. It also summarizes the concentration variations after the electrolysis.

Table 7 Composition variation of Ni-Ti electrode.

Element	AVERAGE CONCENTRATION		AVERAGE VARIATION
	Before the Experiment (%)	After 20 hours (%)	(negative for decrease) (%)
C	0	0.8	+0.8
O	2.0	21.5	+19.5
Al	0.0	1.8	+1.8
Si	0.3	1.1	+0.8
K	0.0	2.7	+2.7
Ti	3.4	3.0	-0.4
Cr	0.2	0.1	-0.2
Mn	0.0	0.1	+0.1
Fe	2.4	0.4	-2.0
Ni	91.6	68.5	-23.1

It was observed that nickel diminished of about 23.1%, while the most apparent positive variation was that of Oxygen (+19.5%). It was worth noticing that the average concentration decrease in Fe (−2.0%) was comparable to the average increase in Aluminum (+1.8%). Figure 48, Figure 49, Figure 50 and Figure 51 show the series of localized concentrations measured before and after the experiments. In particular, when an element average concentration is zero the corresponding series is absent: for instance, on the Ni electrode surface the Aluminum had not been detected before the electrolysis (Table 7, Figure 51).

In Figure 48, two series of fifteen points each show the measured concentration before (in black) and after 20 hours of electrolysis (in red). An average variation between the two series of about 23.1% was observed.
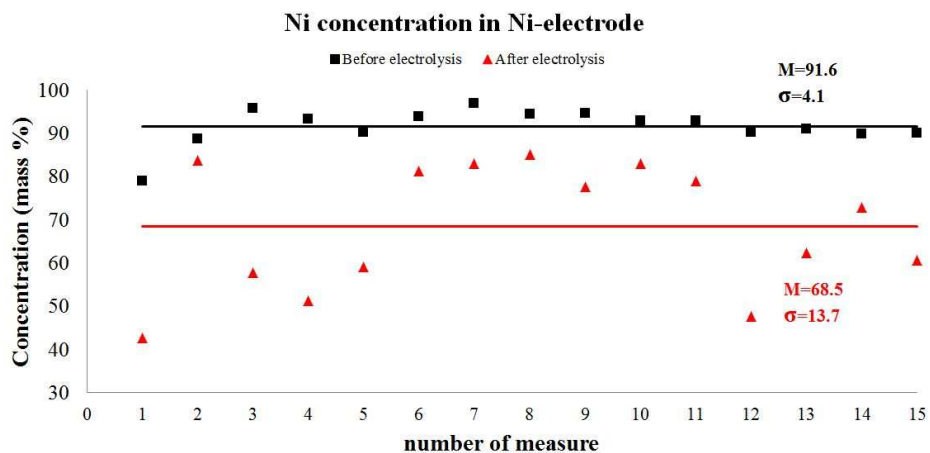
Figure 48 Series of measures of Ni concentration on Ni-Ti anode.

A remarkable variation of the oxygen concentration was observed after the experiment as it is illustrated in Figure 49.
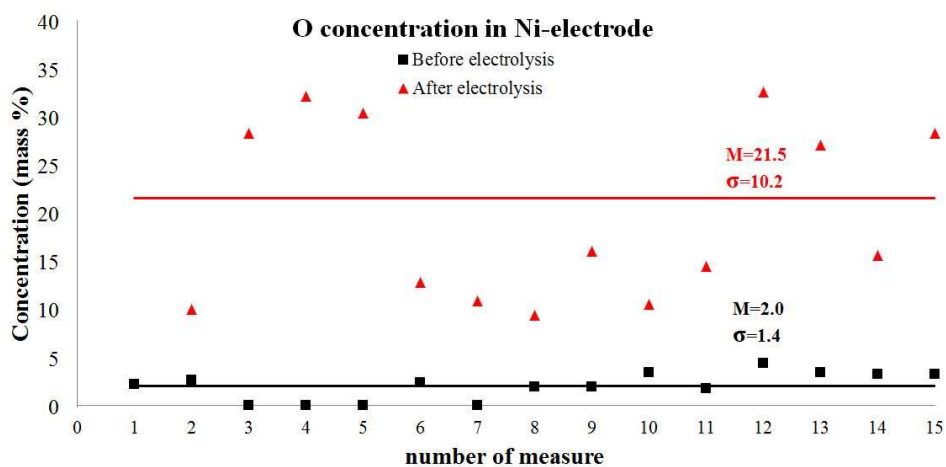
Figure 49 O concentration local measures on Ni-Ti anode.

The average value of O concentration changed from a mass percentage of 2.0% before the experiment to 21.5% after 20 hours of electrolysis.

Details of local variations of iron and aluminum concentrations on the anode surface are presented in Figure 50 and Figure 51.
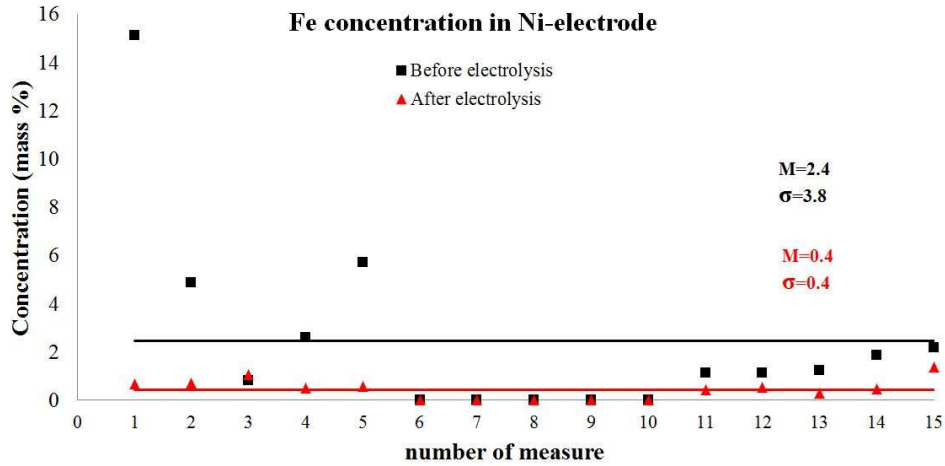
Figure 50 Local measures of Fe concentration.
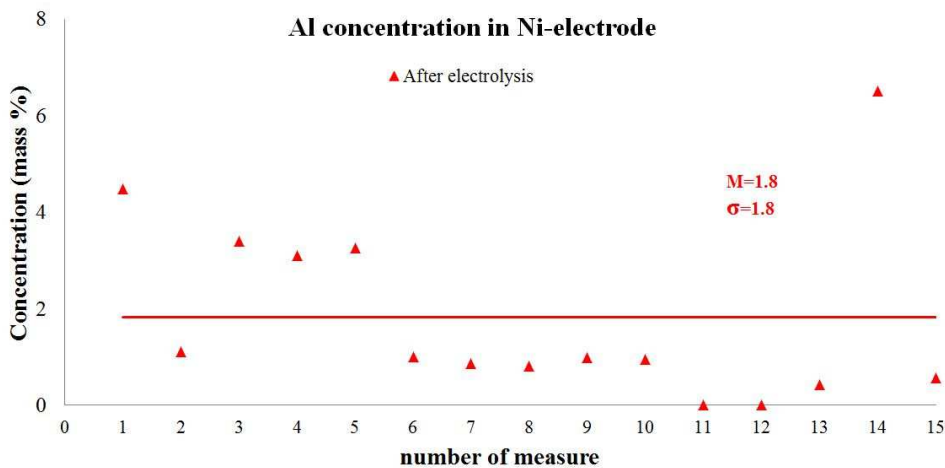
Figure 51 Series of measures of Al concentration found after the experiment.

The average value of Fe concentration changed from a mass percentage of 0.4% at before the experiment to 2.4% after it. The presence of aluminium was not

detected on the electrode before the experiment, but only after the electrolytic process traces of it were found.

On the basis of the piezonuclear reactions conjecture, the Oxygen average variation was assumed associated to nuclear effects and the following piezonuclear reaction was proposed involving the nickel as mother element:

$$Ni_{28}^{59} \rightarrow 3O_8^{16} + 2He_2^4 + 3 \text{ neutrons} \qquad\qquad 4.7$$

A second hypothesis associated to the variation in Fe and Al concentration was considered concerning the iron as mother element and the aluminum as daughter, thus the following reaction was proposed:

$$Fe_{26}^{56} \rightarrow 2Al_{13}^{27} + 2 \text{ neutrons} \qquad\qquad 4.8$$

A third hypothesis associated to the silicon concentration variation was made considering the silicon as daughter element:

$$Ni_{28}^{59} \rightarrow 2Si_{14}^{28} + 3 \text{ neutrons} \qquad\qquad 4.9$$

Reactions 4.7, 4.8 and 4.9 implied emission of neutrons, which was theoretically consistent to the NE peaks measured. The main idea underlying the hypotheses outlined above was that an average decrease of 23.1% in nickel was associated to a reaction producing at least 18.8% of oxygen together with alpha and neutron emissions.

Secondly, an average depletion of 2% in Fe produced about 1.9% of aluminum accompanied again by neutron emissions.

Thirdly, another average decrease in Ni of about 1% contributed to produce silicon (+0.9%) releasing more neutrons. Considering the standard deviations corresponding to each average concentration measured before and after the experiment (Figure 48, Figure 49, Figure 50, Figure 51), the three considerations outlined above were summarized according to the following relationships: *Ni (−23.1%) ⟹ O (+18.8%) +Si (+0.9%) + alpha + neutrons*; *Fe (−2.0%) ⟹ Al (+1.9%) + neutrons*.

Excluding the potassium increase (+2.7%), which could be explained considering the deposition of the salt contained in the solution, the variations of other elements' are lower than 1% and could be overlooked.

Chapter 5

5 INSIGHT INTO NUCLEAR QUANTUM MECHANICS THROUGH A LATTICE MODEL

The presence of diverse groups of models based on different assumptions explaining properties and characteristics of a nucleus, strongly suggest that knowledge of nuclear structure is not a "closed chapter" in Physics [58]. Moreover, recent studies on piezonuclear fission reactions, occurring in the Earth's crust and triggered by earthquakes and brittle rocks failure, provided a good opportunity for old questions concerning nuclear structure to be addressed once again in the light of new phenomena suggestive of low-energy nuclear reactions.

From a structural point of view, there is a need of a model that can be approached also in terms of geometry. Therefore, this Chapter deals with a nuclear lattice model that is used to approach the piezonuclear reactions from a numerical point of view. Such nuclear lattice model has been advocated by Cook and Dallacasa as a unification of the diverse models used in nuclear structure theory [62] [63], but, remarkably, the basic lattice structure was first proposed by the originator of the well-established independent-particle model, Eugene Wigner [64] [65], in 1937 – work that was explicitly cited in his Nobel Prize notification. The lattice model has previously been used to simulate (i) the mass of fission fragments produced by thermal fission of the actinides, and (ii) the transmutation products found on palladium cathodes after electrolysis, as reported in various experimental studies [66] [47] [67]. With regard to the underlying nuclear lattice model, the antiferromagnetic face-centered-cubic (fcc) lattice with alternating proton and neutron layers is the most suitable model for various reasons: (i) from theoretical research on nuclear matter, it is known to be the lowest-energy solid-phase packing scheme of nucleons (N=Z) [58]; (ii) the lattice structure reproduces the quantum number symmetries of the independent particle model (IPM) (the entire *n*-shell and *j-lm*-subshells of the shell model), while being based on the local interactions of the liquid drop model (LDM); (iii) because of the identity between the nuclear lattice and the IPM, the approximate nucleon build-up procedure is known and implies a specific 3D structure for any given number of protons and neutrons with known quantum numbers, which can be represented in Cartesian

space.

Several decades of development of the lattice model suggested that the gaseous, liquid, and cluster-phase models of conventional nuclear structure theory can be unified within this specific lattice model. Moreover, the lattice lends itself to straightforward application in explaining different fission modes [58]. The earlier simulation results were concerned with fission fragments from uranium nuclei and transmutation products from palladium isotopes (experimentally reported by Mizuno in 1998 and 2000 [47]). In order to carry out simulations strictly connected to concepts and contents within the research of this thesis, the Nuclear Visualization Software (NVS) renamed as Quantum Nuclear Dynamics (QND) software [58] was used by the author. Such software is available and downloadable for free from www.res.kutc.kansai-u.ac.jp/~cook.

Anomalous nuclear reactions observed by Carpinteri's research team were taken into account. Specific nuclear lattice structures were modelled to numerically reproduce the nuclear products observed after fracture and fatigue experiments. In addition, the lattice approach allowed to compute a probability related to each possible fission reaction. The probability values obtained for the anomalous reactions could then be used to predict or at least interpret the evolution of the abundance of product elements in the Earth's crust, ocean and atmosphere through the piezonuclear hypothesis drawn from laboratory experimental proofs.

5.1   Geometric Reproduction of fission reactions through the lattice model

As mentioned before, the nuclear lattice model proposed by Cook and Dallacasa was used to simulate the piezonuclear fission reactions by constructing individual isotopes, in accordance with the lattice build-up procedure, and then simulating the cleavage of the lattice along various lattice planes. The starting points for the simulations were therefore the nuclear structures of the elements and those known to be abundant in the Earth's crust today and in previous eras (see Introduction, section 1.4 "Evidence of neutron emission related to fracture phenomena: from the laboratory to the earth crust scale"). Although other nuclear structure models have been developed since the 1930s, the fcc lattice was the most suitable to simulate the anomalous reactions recently discovered because of its clear structural implications. Generally, the simulation begins with a 3D lattice structure of specific isotopes based on the total number of neutrons N and protons Z. By simulating the fission of the nucleus as a fracture occurring along a certain

section plane across the lattice, "fragments" are produced, and correspond to the post-fission daughter nuclei.

The quantum mechanical foundations of the lattice model and its relation to the Schrödinger wave-equation have been discussed elsewhere, but, for the purposes of the simulation, it is sufficient to describe the lattice structure in Cartesian space. That is, the mean position of each nucleon can be defined in relation to its quantum numbers by means of the following equations [58]:

$$x = \left| 2m \right| \left(-1 \right) \left(m + 1/2 \right) \tag{5.1}$$

$$y = \left(2j + 1 - \left| x \right| \right) \left(-1 \right)^{\left(i + j + m + 1/2 \right)} \tag{5.2}$$

$$z = \left(2n + 3 - \left| x \right| - \left| y \right| \right) \left(-1 \right)^{\left(i + n - j - 1 \right)} \tag{5.3}$$

n, m, j, s, i are the quantum numbers that describe the energy state for a given nucleon [39]. Equations 5.1, 5.2 and 5.3 are deduced from a rigorous, self-consistent representation of the IPM in three-dimensional space. In accordance with the known quantum mechanics of nuclear states, each nucleon is characterized by a unique set of five quantum numbers, which define the precise energy state of the nucleon, as described by the Schrödinger equation [39]. The spatial origin of this wave is a function of the three coordinates x, y, z. Hence, for any isotope, knowing that each nucleon belongs to a certain energy level given by the values of its quantum numbers, it is possible to consider the 3D lattice of nucleons as a representation of its quantum mechanical state.

Piezonuclear reactions cannot be defined as traditional fission reactions, since temperature and energy conditions are not equivalent to those involved in thermal neutron-induced fission. For this reason, it is convenient to verify that these anomalous reactions may be correctly described in the QND simulations. To simulate this new kind of fission, it was assumed that fractures propagated in the nuclear lattice along their crystal planes. Following this approach, two distinct fragments are produced from any considered reaction. Their characteristics are given by the software in terms of fragment stability, fission threshold energy related to a certain fracture plane, and number of protons and neutrons in each fragment. The resulting elements can be deduced from the characteristics of the

fragments obtained at the end of the simulation. The analysis of the nuclear characteristics is described in the next section along with the isotopes obtained from the piezonuclear reactions. Important considerations were made concerning the neutron emissions from the anomalous nuclear reactions measured during the experiments. They could be deduced by investigating the stability of the resulting fragments. In fact, it was assumed that unstable isotopes with an excess of neutrons were likely to induce neutron emissions, depending on local binding characteristics, in order to reach more stable nuclear states. These emissions deduced from the model were then compared with the experimental results reported by Carpinteri et al.

5.1.1 Application of the model through the QND software

The QND software simulates lattice structures up to 480 nucleons and calculates fission results regarding seventeen different section planes for each given nuclide. In actual fact, many more lattice planes are available for simulation, but the electrostatic repulsion between the protons in the two fragments is much greater for lattice planes that break the lattice structure into approximately symmetrical fragments, so that many low-repulsion, asymmetrical fission events are ignored. A single simulation consisted in fracturing the nucleus along one single plane at a time, breaking only the bonds that connected the two fragments. It is understandable that the choice of the fracture planes is affected by the lattice structure and, therefore, by the position of the nucleons with respect to the x, y, z axes. Being the lattice model drawn from crystallography implies that all the planes used for the simulations correspond to the principal crystallographic planes [58]. In particular, the seventeen planes used by the QND are parallel to the horizontal, vertical and inclined (45°) planes passing through or near the origin of the axes. Each plane is identified by a number from 1 to 17, as shown in Table 8.

Table 8 Fission planes and their identification numbers in the QND software

Fracture Plane	Equation
1	$x = 2$
2	$x = 0$
3	$x = -2$
4	$z = -2$

5	$z = 0$
6	$z = 2$
7	$y = 2$
8	$y = 0$
9	$y = -2$
10	$-x + y + z + 1 = 0$
11	$-x + y + z - 1 = 0$
12	$x - y + z + 1 = 0$
13	$x - y + z - 3 = 0$
14	$-x - y + z - 1 = 0$
15	$-x - y + z + 3 = 0$
16	$x + y + z - 1 = 0$
17	$x + y + z + 3 = 0$

More than twelve reactions derived from direct and indirect experimental evidence were simulated by means of the QND along different fission planes, each considering a different mother element (Table 2). As mentioned in the Introduction, the elements known to be involved in the piezonuclear reactions were introduced in the numerical simulations. Such reactions were strictly connected to: (i) the experimental results obtained from the EDX analyses performed after fracture tests on natural rock specimens, or (ii) the compositional changes in the Earth's crust evolution during the last 4.57 billion years. As recently reported, the evolution of the Earth's crust and atmosphere, the formation of oceans and greenhouse gases, and the origin of life are phenomena deeply related to piezonuclear reactions. This was the motivation for undertaking the simulation of fission reactions according to a non-traditional methodology.

These reactions were simulated using two build-up procedures for nuclear structure. The first one generated a default nucleus where each nucleon has a pre-assigned position and quantum numbers that give the lattice a regular, densely-packed, polyhedral structure. The second procedure used the "picking function",

which was the most convenient way for constructing a nucleus from a set of nucleons with specific quantum numbers and coordinates. The picking function was adopted only when the lattice structures using the default configuration were inappropriate due to the weak bonding of the last few nucleons. In particular, once a specific default nucleus was constructed and displayed, usually the last two protons or neutrons were individually moved from one energy-state to another to find the configuration that best reproduced the (fission) product elements.

All reactions reported in Table 2 (Chapter 1 Introduction, section 1.4 "Evidence of neutron emission related to fracture phenomena: from the laboratory to the earth crust scale") were simulated by the QND and the results are summarized in Table 15 reported in the APPENDIX. For each simulation, the plane that allows the fission is indicated. Each fragment is identified by the number of protons (Z), the number of neutrons (N), and the corresponding isotope. In addition, when the fragment was unstable, QND software displayed the experimentally-known decay time of that fragment. In the case of unstable fission fragments, the number of neutrons exceeded the stable condition and neutron emission might have been assumed for that fragment in order to achieve stability. It was interesting to note that, from the QND results, it was possible to deduce and reproduce the neutron emissions of piezonuclear reactions, in addition to the product elements (fragments).

For the first simulation, the Fe^{56}_{26} (also referred to as Fe^{56}) nucleus was chosen as the mother element and the lattice of this nucleus is shown in Figure 52. Its characteristics assigned by the software were as follows: Protons: 26; Neutrons: 30; n-values: 0, 1, 2, 3; j-values: 1/2, 3/2, 5/2, 7/2; m-values: $\pm 1/2$, $\pm 3/2$, $\pm 5/2$, $\pm 7/2$, according to the literature [39].
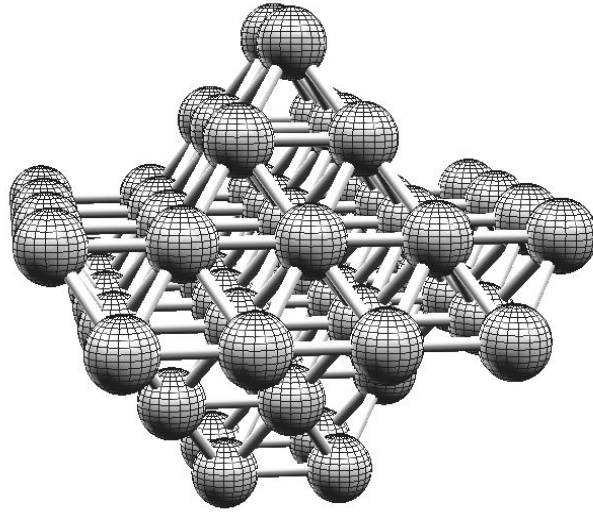
Figure 52 Fe^{56} lattice structure.

Once the nuclear structure was modified with the picking option, the lattice was "fractured" along fission planes that cut all crossing nucleon-nucleon bonds. Among the 17 planes of fission, six of them were relevant to reactions (1), (2) and (3) of Table 2, whereas the remaining 11 produced results not consistent to the empirical data, thus they were overlooked. Specifically, the simulation results related to reaction (1) predicted the fission of iron along fission planes 2 and 8, which were the yz and the xz plane in Cartesian space respectively (see Table 8).

In Figure 53 two lattice structures of Fe^{56} are sliced in two fragments each by specific fission planes. Broken bonds connecting the two fragments resulting from each cut are displayed in red. The two iron structures refer to reaction (1) reported in Table 2 and Table 15 in the APPENDIX.
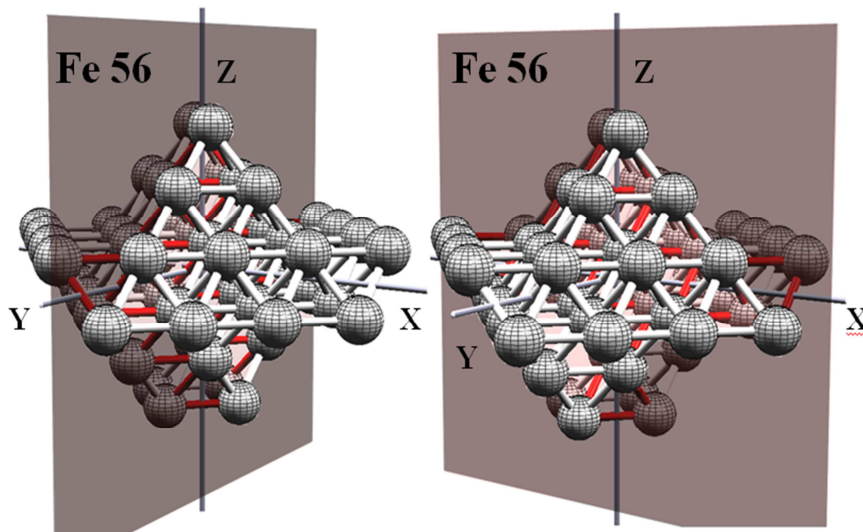
Figure 53 Fracture of the Fe^{56} lattice along planes 2 (x=0) and 8 (y=0).

The fragments produced from the fission along planes 2 and 8 possessed the same characteristics as those described in the piezonuclear reaction (1) (Table 2). The two fragments corresponded to Al^{27}_{13}, and Al^{29}_{13}. The former was stable, whereas the latter was unstable as it contained two neutrons in excess, which were weakly-bound to the lattice fragment and were presumably released when such reaction occurred. Assuming the emission of these two neutrons, the fission can be considered as symmetric with respect to both planes 2 and 8.

The second simulation was run in accordance with reaction (2) (see Table 2 and Table 15 in the APPENDIX). In this case, the lattice structure for Fe^{56} was built using the picking option. Figure 54 illustrates the fission of Fe56 along planes 14 (-x-y+z=1) and 16 (x+y+z=1). Broken bonds are in red and they connect two fragments corresponding respectively to Mg and Si according to reaction (2) in Table 15 in the APPENDIX.
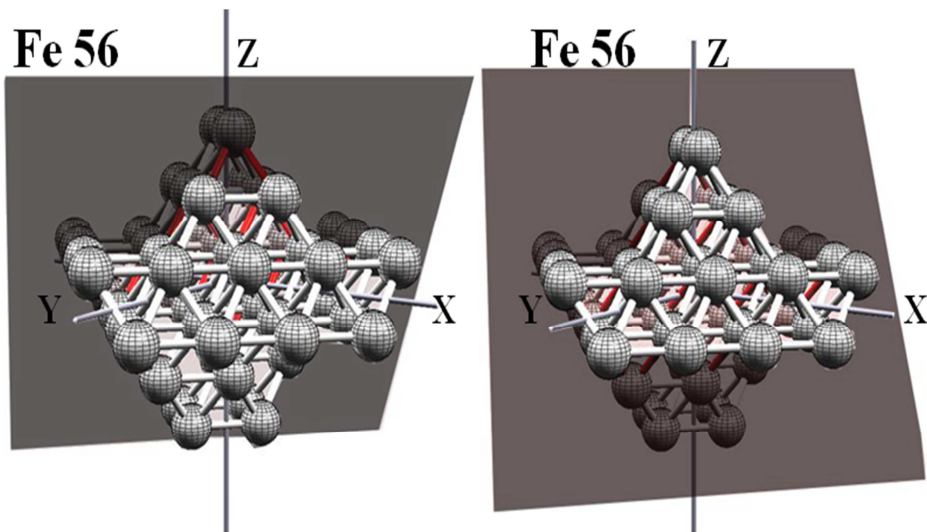
Figure 54 Fracture of Fe^{56} lattice along planes 14 and 16.

The results of the simulation showed that the fragments predicted were consistent to those of reaction (2) for fission occurring along two different planes: 14 and 16. It was remarkable that the fragments from the fission along plane 14 were identical to those along plane 16. The simulation produced an isotope of Mg and an isotope of Si, which were identified as Fragment 1 and Fragment 2. In each case, Fragment 1 was stable, whereas Fragment 2 was unstable. In particular, Fragment 1 was a stable nucleus of Mg^{24} and Fragment 2 was a nucleus of Si^{32}, unstable, which contained 4 neutrons that could be released when reaction (2) occurred.

Magnesium and calcium were considered next as mother elements of next fission simulations. A nuclear lattice reproducing the structure of Mg^{24} is displayed in Figure 55.
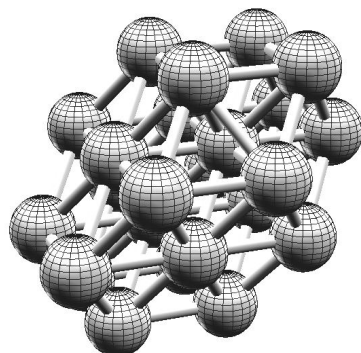
Figure 55 Mg^{24} nuclear lattice structure

Figure 56 illustrates how Mg^{24} structure is cut by plane 2. The red bonds connecting the two resulting fragments are interrupted by the fission plane.
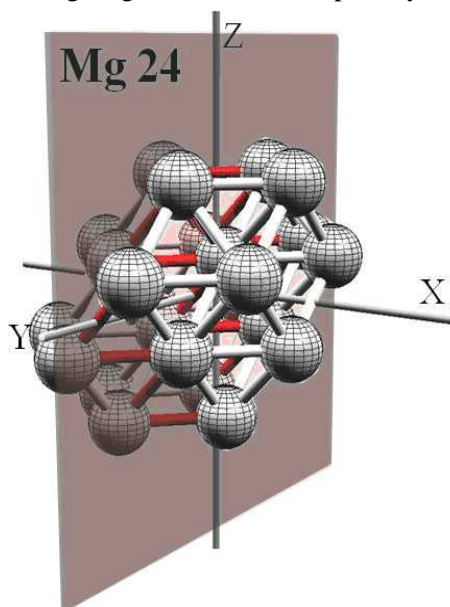
Figure 56 Fracture of the Mg^{24} lattice along plane 2.

Figure 57 illustrates the structure of Ca^{40} lattice, which was relevant to reaction

(12) where calcium was the mother element resulting in nuclei of oxygen and hydrogen.
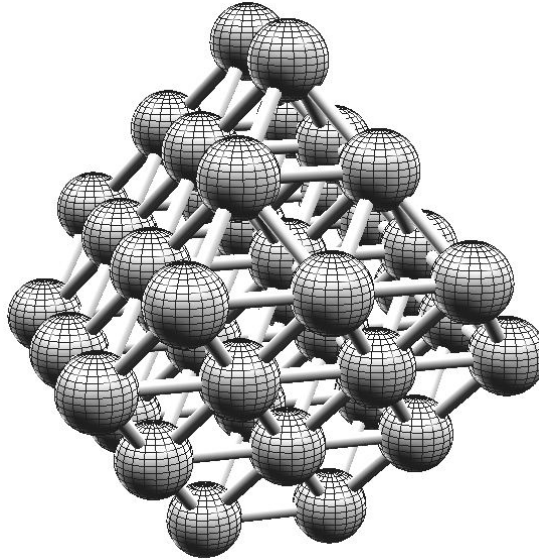
Figure 57 Ca^{40} nuclear lattice structure.

Considering the data from the Earth's crust and the indirect piezonuclear evidence, the hypotheses of reactions (7) and (12) were particularly significant for their respective implications concerning atmosphere evolution and ocean formation. The simulation results of these reactions are summarized in Table 15 in APPENDIX. The simulation of piezonuclear reaction (7) produced as fragments two nuclei of C^{12} with no excess of neutrons. Therefore, the simulation described a symmetrical fission that did not entail neutron emissions according to piezonuclear reaction (7).

On the other hand, as observed in the case of reactions (1), (2), and (12), there were unstable fragments. In particular, for every plane (Table 15 in APPENDIX) that allowed for the products $(2O_8^{16} + 4H_1^1)$ of piezonuclear reaction (12), at least one of the two fragments obtained from each simulation was unstable. This results suggested that neutron emission was favored in many of the lattice fission events. Figure 58 illustrates an example of the Ca lattice sliced by planes 1 and 3 associated to the simulation of reaction 12 (Table 15).
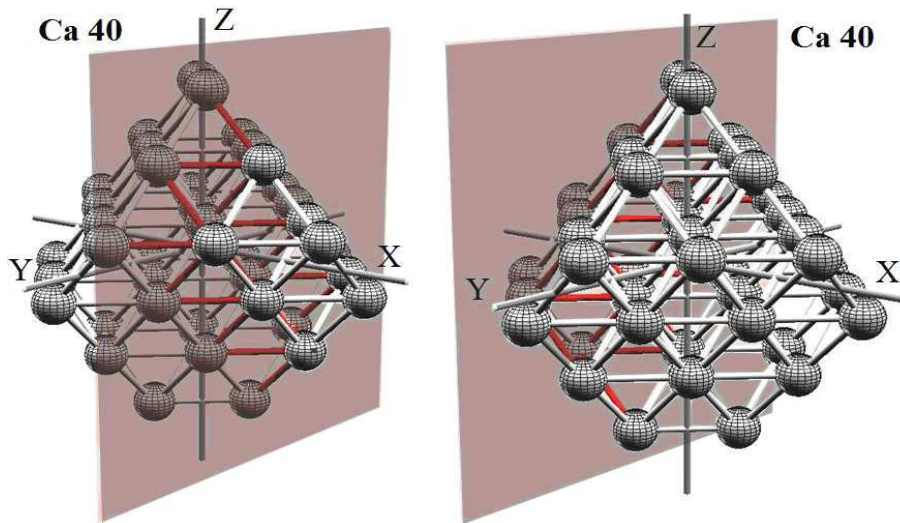
Figure 58 Fracture of the Ca^{40} lattice along planes 1 and 3.

5.1.2   Probability of fission according to the lattice model

As described above, the nucleus is represented as a lattice where the nodal positions are occupied by the nucleons. A given nuclear lattice in its ground-state has a certain total binding energy (BE) that generally depends on the number and type of nearest-neighbour nucleon-nucleon bonds, thus on the number of constituent nucleons [58] [39] [3]. The binding energy is usually expressed as average binding energy per nucleon (BE/nucleon) or average binding energy per bond (BE/bond), which represents a mean value of the energy distribution among the bonds in the nucleus. According to the lattice model, the bonds are not all equivalent and are formed by various combinations of nucleon states (as specified by quantum numbers n, j, m, s and i). Specifically, the dipole-dipole interactions of nucleon pairs are attractive (singlet-pairs) for all nearest-neighbour PP and NN combinations, but there are both attractive and repulsive dipole combinations for PN pairs (triplet- and singlet-pairs, respectively). As a consequence, the antiferromagnetic fcc lattice with alternating proton-neutron layers implies the existence of lattice planes that are either strongly or weakly bound, depending on the character of the bonds in the lattice plane. It is the internal structure of the

nucleon lattice that leads directly to the prediction of lattice fragments of various masses and probabilities.

In order to assess the probability of fission occurring in a given nucleus, it is necessary to know the binding force of the nuclear lattice structure: the lower this force is, the higher the probability of fission is. This can be evaluated in terms of binding energy of the lattice structure through a specific plane. In particular, the binding energy of the bonds between nearest-neighbour nucleons crossed by a fracture plane minus the Coulomb repulsion through the same plane represents the residual binding energy. Inverting this value yields a ratio (MeV^{-1}) that is defined as proportional to the probability of fission ($P_{fission}$) [58]:

$$P_{fission}\left(Z,N\right) = \frac{1}{\left(\beta \sum_{m}^{A_{f1}} \sum_{n}^{A_{f2}} b_{m,n} - \sum_{j}^{Z_{f1}} \sum_{k}^{Z_{f2}} Q_{j,k}\right)} \qquad 5.4$$

where Z, N, and A are the number of protons, neutrons and the total number of nucleons contained in the atomic nucleus; *f1* and *f2* stand for the two resulting fragments of the given reaction; *β* is an experimental value of the nucleon-nucleon binding force. Between nearest-neighbour nucleons this value changes according to the different nature of the bond; $b_{m,n}$ is the number of bonds across the fission plane taken into consideration and so the number of broken nucleon-nucleon bonds along the fracture plane; $Q_{j,k}$ is the Coulomb repulsive contribution between the protons in the two fragments defined by the fission plane.

Using the parameter $P_{fission}$, the probabilities of piezonuclear reactions (1) and (2) were calculated as shown in details in Table 15 in the APPENDIX. The Fission Probability is expressed as a normalized percentage of the cases studied for each element reported in Table 2 with their relevant fission planes, and a given binding force value β is assumed (approximately comprised in the range between 2 and 4 MeV) [58]. The simulation of piezonuclear reaction (1) resulted in two cases of the 17 possible fission planes, with a total $P_{fission}$ of ~23%, whereas reaction (2) resulted in two cases having a total $P_{fission}$ of ~41%. According to these considerations, it was of interest that these probabilities reproduced the known abundances of the Al^{27}, Mg^{24} and Si^{28} elements in the Earth's crust. The probability that a nucleus of Fe^{56} produced magnesium and silicon (piezonuclear reaction (2) in Table 2) is significantly larger (ratio:1.74) than that implying the symmetrical nuclear fission of Fe^{56} into two Al^{27} atoms (reaction (1) in Table 2).

This was in agreement with the evidence regarding the compositional changes in the evolution of the Earth's crust. In fact, the total decrease in Fe^{56} over the last 4.57 Billion years of about 11% seemed to be consistently counterbalanced by the increases in Mg, Si and Al, where the contribution of Mg^{24} and Si^{28} (~7%) was a little less than twice that of the Al^{27} increase, ~4%. The ratio of the normalized $\boldsymbol{P_{fission}}$ of reaction (2) to that of reaction (1) was approximately 1.75, as the ratio of Mg and Si (~7%) increase to the increase in Al (~4%) in the Earth's crust. It is also interesting to note that reaction (3) involving Fe as the mother element and Ca and C as the products could be obtained by the QND simulation. This reaction, not so frequent in the Earth's crust system, could be recognized as a fundamental reaction during the application of ultrasound to sintered Ferrite (α-Iron) and steel bars, as recently reported by Cardone et al. [20]. This evidence indicates that the QND was able to reproduce different piezonuclear fission reactions also belonging to different systems and experiments at different scales (Earth's crust or ferrite bar).

The results obtained from the Ca-based reaction simulations also showed consistency with the findings reported by Carpinteri and his research team. During the evolution of the Earth's crust, Ca decreased by about ~4%, while K increased by about ~2.7%, according to reaction (11). The total Ca depletion could be almost perfectly counterbalanced considering the increases in O and H (H_2O) that together correspond to an increment of about 1.3%. This means that more than two thirds of the Ca depletion resulted in potassium and approximately one third in H_2O. On the other hand, considering the probability of fission computed for reactions (10), (11) and (12), the piezonuclear reaction involving K as the product returned a normalized probability of ~58.4%. The normalized probability of the simulation of reaction (12), involving H and O as products, is about 31.2% (Table 15 in the APPENDIX). The ratio of the fission probability of reaction (11) to that of reaction (12) was about two, which was in good agreement with the evidence concerning the Earth's crust (see Chapter 1, section 1.4).

The consistency with the evidence drawn from the Earth's crust can be verified also in the case of Mg as the starting element of the anomalous reactions (7) to (9). In particular, it was found a global Mg decrease (~7.9%) that was counterbalanced by a ~2.7% increase in Na in the Earth's crust and by increases of ~2.0% and ~3.2% in H_2O and C, respectively, in the ancient atmosphere. The evidence of the Na increase was supported by the QND simulation that returned a normalized probability percentage for reaction (8) equal to ~31.0%. With regard to the other reactions, involving C, O and H as resultants, it was obtained a total normalized

probability percentage of about ~69%. These last two percentages were in good agreement with the considerations concerning the evolution of the Earth's crust composition as about two thirds of the Mg decrease could be ascribed to the formation of gaseous elements such as C and H_2O that formed in the proto-atmosphere of our planet [32].

5.2 Optimization of a set of parameters accounting for the binding energy

Within this section a closer look at the lattice model was provided. In particular, an overview of the research developed in collaboration with Professor N.D. Cook of the Kansai University (Osaka, Japan) is presented below.

The research activity consisted of three main phases: the first one was modelling a statistically significant series of stable and semi-stable nuclei; after that, the second phase was collecting the data for each nuclear structure, and, in the third phase, optimizing the structures in order to obtain predictions of the nuclear binding energies that better fit the experimental data. This process of modelling led to a set of improved parameters that were later used to predict better nuclear binding energies and fission fragments for medium-heavy nuclei. The process of optimization of the parameters in presented in the following section accompanied by new predictions of fission fragments concerning certain elements related to the experimental activity conducted by Carpinteri et al. The assumptions underlying the parameter optimization is reported as well.

By means of the QND (quantum nuclear dynamics) software, a series of structures of stable and semi-stable nuclei was built according to the lattice model. A set of ten factors was defined in order to calculate the binding energy as a linear combination of such factors. In Table 9 the set of ten parameters defined to describe the nuclear binding energy is summarized. Such factors were defined in order to obtain a better prediction of nuclear binding energies.

Table 9 Ten parameters defining different bond strengths.

PP1	NN1	PN1s	PN1t	PP2	NN2	PP3	NN3	PN3s	PN3t

The factors shown in Table 9 were named after the type of strong interaction

they refer to. That is, the proton-proton interaction factors were labelled PP, the neutron-neutron ones NN and the proton-neutron interactions PN. Distinctions were made for first, second and third neighbour interactions (e.g. PP1, PP2, PP3) as well as for strongly bound triplet pair interactions (e.g. PN1t, PN3t) and weakly bound singlet pair interactions (e.g. PN1s PN3s). Once such factors were set, nuclear structures were modelled and data were collected, that is, the number and type of inter-nucleon bonds, experimental known values of spin, parity and binding energy of the corresponding element.

The optimization of the ten factors could have been conducted in two different ways: on one hand, by means of a multiple regression technique and, on the other hand, by means of a Biot-Savart-like calculation, as proposed by Dallacasa. The multiple regression technique was already used by Professor Cook in a multi-factor parameter optimization procedure. In detail, Cook conducted linear regression analyses for different number of variables (e.g. one, three, eight or ten factors). Setting to zero the y-intercept of the regression line for each set of chosen variables implied that there were no other supplementary relevant variables. Although this might be unrealistic, it allowed accounting for the independent variables only, assessing their relative weight and adjusting them within the regression procedure. Results of a 10 factor regression analysis are summarized in Table 10. All the output data of the regression, such as correlation factors (R, R2, Corr. R2), standard deviations, number of objects, statistical significances (t-value, P-value), etc. are included in the table. The "s" and "t" associated to the bond strength parameters indicated singlet and triplet pair interactions, while the numbers 1, 2 and 3 indicated first, second and third neighbour interactions, distinguishing different ranges of interaction.

Table 10 Multiple Regression of Nuclear Binding Energies with 10 Factors.

Multiple Regression	
R	0.99999
R2	0.99998
Corr. R2	0.99620
Std Dev	7.44021
No. Obs.	273

Factors	Coeff.	Std. Dev.	t-value	P-value
Intercept	0	-	-	-
PP1s	2.715	0.301	9.035	0.000
PP2t	-0.918	0.226	-4.054	0.000
PP3s	1.436	0.170	8.449	0.000
NN1s	1.804	0.217	8.306	0.000
NN2t	0.332	-0.145	-2.284	0.020
NN3s	-0.615	0.116	-5.298	0.000
PN1t	3.025	0.447	6.772	0.000
PN1s	2.258	0.470	4.807	0.000
PN3t	1.208	0.195	6.209	0.000
PN3s	0.338	0.210	1.607	0.109

For such regression analysis 273 nuclei were modelled and their structures optimized. Assuming that nuclei self-organize uniquely into an antiferromagnetic array of alternating layers of protons and neutrons, the positions of all surface nucleons were manipulated individually for each lattice structure built.

An alternative approach was considered when defining the factors accounting for the binding energy. First of all, the three factors PP1, NN1 and PN1t were defined according to Dallacasa *et al.* [58]. Using the expression of the potential

$$V = \mu_0 \frac{\mu_1 \mu_2}{\pi R^2 y} \cos \varphi + 0(y^{-2}) \qquad\qquad 5.5$$

the short-range nucleon-nucleon interactions could be calculated, thus the values of the factors accounting for the binding energy were defined. The basic assumptions underlying the Dallacasa calculation were as follows. Each factor represented the strength of the bond (energy) of the corresponding interaction and could be calculated as V (see formula above). The magnetic properties μ_0, μ_1 and μ_2 are the magnetic permeability of vacuum and the magnetic moments of protons and neutrons respectively, they are known from the literature, thus fixed [39] [3]. Considering the dimensions of the nucleon in terms of its radius R allowed to calculate the energy of each bond (interaction) as depending only on R and on the distance y between the two interacting nucleons. Dallacasa investigated the short-

range interactions of the first neighbour nucleons with a radius of 0.5 fm and a relative distance of 2 fm. According to those assumptions an average binding energy of about 3 MeV could be found from the factors PP1, NN1 and PN1 calculated to be approximately 3.93, 1.84 and 2.69 MeV respectively. Such value of binding energy is not far from the average binding energy per nucleon reported in the literature [39] [68]. However, other relevant factors were left aside, such as the second and third neighbour interactions and the distinction between triplet- and singlet-pair nucleon interactions. For this reason "new" factors were added to the Dallacasa calculations. In detail, according to the antiferromagnetic array of the lattice geometry, three different relative distances y were chosen for first, second and third neighbour nucleons respectively and an initial nucleon radius R of approximately 0.5 fm was considered. In Table 11 the distances used for the calculation of the strength factors are presented according to the lattice geometry and to Dallacasa's assumptions. The definition of the eight values is also illustrated in the table. It is evident that first neighbour interactions are stronger than second and third neighbours as the distance (2 fm) is smaller than that of other nucleon pairs.

Table 11 Ranges of interaction associated to their nucleon-nucleon pairs parameters.

Distance (fm)		2		2.83		3.46	
Nucleon pairs		PP1, NN1, PN1		PP2, NN2		PP3, NN3, PN3	
PP1	**NN1**	**PN1**	**PP2**	**NN2**	**PP3**	**NN3**	**PN3**
3.93	1.84	2.69	-2.75	-1.29	2.25	1.06	1.54

Once all necessary assumptions and independent variables were defined, it was possible to begin the optimization procedure. For model optimization was intended the optimization of the factors PP1, NN1, etc. This also led to the optimization of the binding energy prediction by means of the QND software. Such procedure was conceptually straightforward as it implied, setting the factors (function of R), building the lattice structure of a given number of nuclei, check each QND prediction of the binding energy with its experimentally known value, assess the error and correct the R accordingly. However, building the lattice structure of the nuclei required a certain effort as each single structure had to be built in order to grant the compliance and consistency of lattice model properties to those of the nucleus which is modelled. This meant building a nucleus lattice so

that its total spin, parity, and magnetic moment were consistent with the known values reported on the periodic table of Elements [68]. Thus, more than 300 nuclei were modelled including light, medium, heavy both stable and semi-stable nuclei.

Figure 59 shows the results of binding energy prediction (BE(8)) calculated using 8 strength factors. Each value was referred to the corresponding atomic number (number of proton Z) of the relative nucleus. It was also compared with the reference experimentally known nuclear binding energy indicated as expBE. The BE(8) energy, expressed in MeV on the primary vertical axis, is the sum of the nuclear experimental binding energy and the Coulomb repulsion calculated according to the liquid drop model (LDM). It was quite evident that the error of the prediction could not be ignored as it went over 50% of the experimental value.
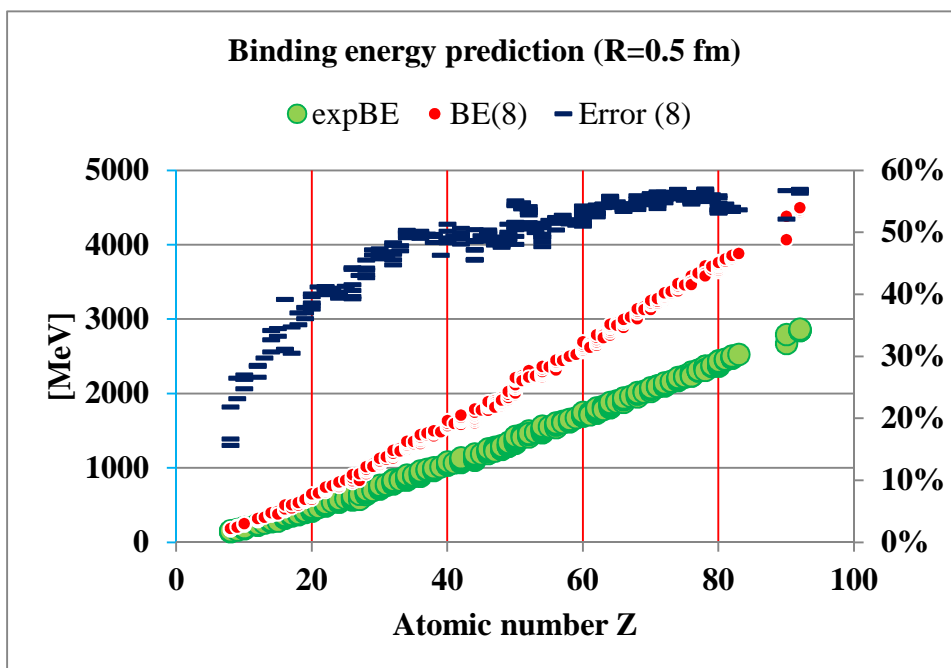

Figure 59- Eight factors binding energy prediction.

During the lattice building procedure, it wasalso noticed that the structures could develop mainly in two directions: along the *z axis* (around the lower j-subshells) or along the *xy plane* (with increasing j or m). Moreover, the medium

and heavy nuclei lattice structures appeared to be somehow slightly oblate, resulting in a larger number of proton-neutron (PN) type bonds. This fact led Professor Cook and the author to think that the PN pairs played a larger role in the contribution to the nuclear binding energy, thus it was decided to add two more factors to our set of eight.

Therefore, a new set of ten strength factors was calculated as shown in Table 12. The effect of proton-proton, neutron-neutron and proton-neutron pairs was considered at different distances, distinguishing also between triplet and singlet pair interactions.

Table 12 Set of ten new factors accounting for the binding energy.

PP1	NN1	PN1t	PN1s	PP2	NN2	PP3	NN3	PN3t	PN3s
3.93	1.84	2.69	1.34	-2.75	-1.29	2.25	1.06	1.54	0.77

The linear combination of those factors was intended to provide an expression of the binding energy including also weaker effects between the nucleons according to their position inside the lattice nuclear structure. It is worth mentioning that the factors referring to the singlet pairs (PN1s and PN3s) had been chosen as half of those referring to the triplet pairs (PN1t and PN3t). Such decision was taken as according to the literature the proton-neutron singlet pairs were assumed to be weakly bound short-range interactions.

A series of over 300 nuclei was modelled once again adopting the new set of ten factors. After collecting the data from the numerous nuclear structures, we calculated a new binding energy prediction keeping **R** equal to 0.5 fm.

Figure 60 reports the 10 factors-prediction (BE(10)) of the binding energies expressed in MeV and associated to their relative nuclei (number of proton Z). On the primary vertical axis the energy is expressed as the sum of the experimentally known binding energy and the Coulomb repulsion. On the secondary vertical axis the percent error between the experimentally known nuclear energy (expBE) and the QND ten factors prediction one (BE(10)) is indicated.
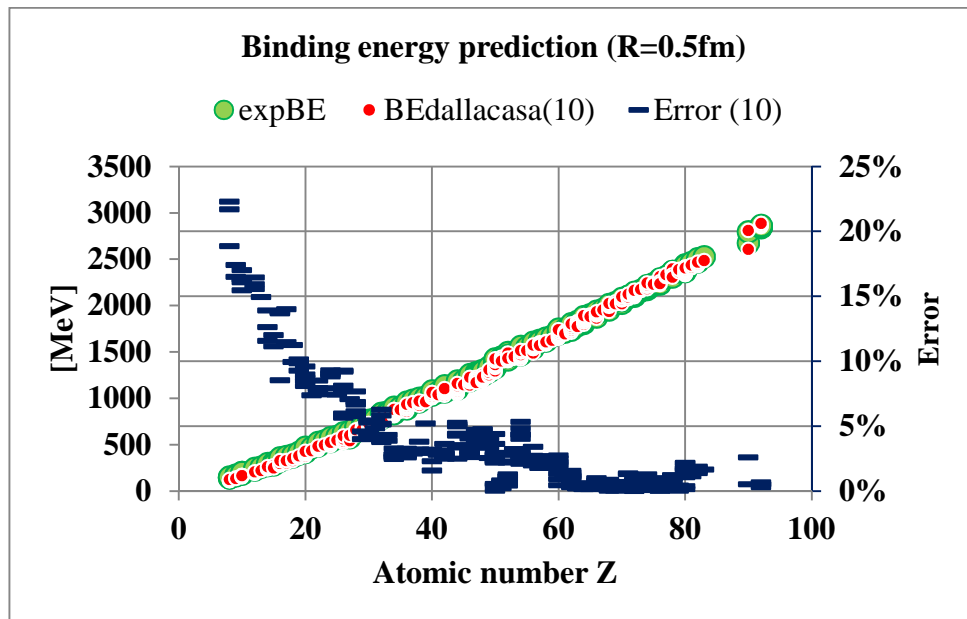
Figure 60 Binding energy estimates with respect to the atomic number.

The 10-factors prediction provided a better estimate of the nuclear binding energy since the error was averagely half of that showed in Figure 59. Although lower than before, the error was still over 25% of the experimental value. In detail, looking at the light nuclei (Z<10), the figures showed overall predictions that overestimated by 20-30% the experimental value. Although, the 10-factors estimate for medium nuclei was generally better with an average error lower than 20%, the graphs showed an increasing trend of the predicted energy for heavier nuclei (Z>60) leading to values above 20% higher than the reference ones.

In order to reduce the error a new prediction was calculated. Assuming a bigger nucleon radius **R**, the coulomb repulsion contribution would have produced a smaller effect for the heavier nuclei, thus the predicted energies would have been slightly lower. In Figure 61 the estimate of the 10 factors energies is reported with respect to the corresponding atomic number of associated nuclei. In detail, the 10 factors energy prediction was calculated increasing **R** from 0.5 to 0.55 fm.

Figure 61 Binding energy predictions with respect to the atomic number.

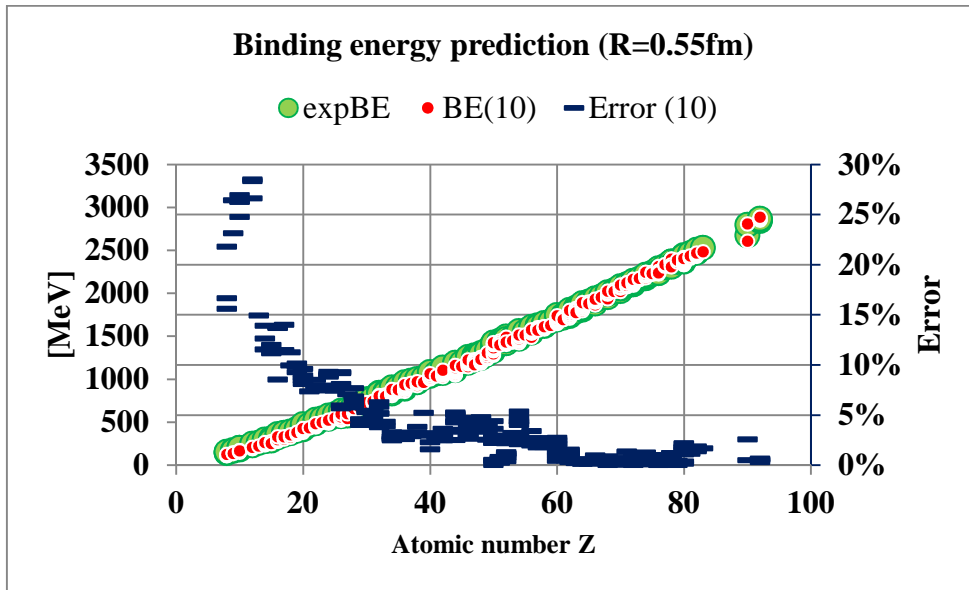The error trend in the graph of Figure 61 showed an improvement on the estimate. The binding energy prediction was more accurate as the atomic number Z increased. For small Z the average error of the prediction was still around 25% or slightly above. Supposedly, the three factors related to the first neighbour bonds played a more substantial role in accounting the binding energy of light nuclear lattice structures. In fact, the number of second and third neighbours bonds was lower in such nuclei. In addition, the structures of small nuclei ($Z<10$) tended to be quite compact and their nucleons did not have the possibility to be distributed along one direction or another. For these reasons, the calculated estimate maintained a constant average error of about 25% the experimental energy. However, the medium and heavy nuclei had lattice structures with a higher number of bond types, thus the 10-factors assumptions better fit the lattice model geometry and provided better energy predictions for such nuclei.

The optimization of the 10 factors accounting for the binding energy described above allowed to work with a better version of the QND software than it was before. Hence, new simulations were carried out. In particular, the fission of a new series of nuclear structures was investigated according to the lattice model, that is,

iron, nickel and palladium. A description and commentary of the simulation is dealt in the following part of this section. The first element modelled was iron, thus four isotopes were investigated, that is iron 54, 56, 57 and 58, their natural abundances are 5.85%, 91.75%, 2.12% and 0.29% respectively [3] [68].

Table 13 lists the significant elements resulted from the fission simulation of iron nuclei. The amount of significant elements estimated to result as fission fragments simulated by the QND is reported in terms of relative percentage, where 100% represents the total sum of prediction results of all isotopes investigated.

Table 13 Significant results of the fission of iron isotopes.

Iron fission overview	
C	2.2%
Mg	1.9%
Al	6.7%
Si	10.3%
Ca	35.8%
Total	56.9%

It is important to emphasize that only stable natural isotopes were considered. As it was already stated in previous studies described in this same chapter in previous section, the fission simulation estimated 17 cases of fission of a given nuclear lattice structure. Each case was relevant to the geometrical fission of the lattice across a different crystallographic plane, and produced two fragments. It is necessary to state that the cause of the fission was not investigated and it was assumed that, whatever the cause was, an energy equal to or larger than the fission energy was always provided for the reaction to occur. The characteristics of the fission fragments were assessed by the QND software and provided as an output. For what concerns the four iron isotopes only about 57% of the results were significant (Table 13). It is important to emphasize that the ratio (about 1.8) of the sum of Mg and Si (Table 13) to the amount of Al, estimated from the fission of iron isotopes, is quite close to the ratio (about 1.7) of Mg and Si increase to the increase in Al according to the Earth's crust evolution. This observation confirmed similar results obtained with the previous version of the QND software, thus contributes to support Professor Carpinteri experimental research on piezonuclear

reactions, along with the geological findings on the Earth's crust compositional evolution.

As mentioned above, the fission of other elements was investigated. An overview of the estimated fission fragments is reported in Table 14. In the table, the significant elements resulting from the fission of different isotopes are displayed. Their relative percentage abundance was calculated with respect to all possible resulting fragments estimated. As it can be noticed, the sum of the percentages is not 100% as some predictions were inconclusive and did not lead to any identifiable fragment, thus they were excluded.

Table 14 Overall prediction results of the fission of nickel and palladium isotopes

Nickel fission overview		Palladium fission overview	
C	4.5%	Si	3.2%
N	3.6%	P	2.4%
O	0.3%	S	1.8%
Ne	10.9%	Ar	6.9%
Na	1.2%	Ca	5.1%
Mg	0.2%	Ti	6.6%
Si	22.6%	Cr	8.6%
P	0.1%	Mn	2.8%
S	0.6%	Fe	4.1%
Cl	7.9%	Ni	7.5%
Ar	5.4%	Cu	3.9%
K	2.5%	Zn	8.5%
Ca	6.8%	Ge	6.2%
Sc	10.4%	As	4.8%

Ti	14.0%	**Se**	9.2%
Cr	1.6%	**Br**	1.6%
		Kr	6.2%
Total	92.8%	**Total**	89.5%

Five nickel isotopes were modelled, that is nickel 58, 60, 61, 62 and 64. Their natural abundances are respectively 68.02%, 26.22%, 1.14%, 3.63% and 0.93% [68]. Six palladium isotopes were also investigated: palladium 102, 104, 105, 106, 108 and 110. As it was done for the other cases, each fission fragments prediction was weighed according to each isotopic abundance, that is 1.02%, 11.14%, 22.33%, 27.33% and 26.46%, respectively, for each of the six palladium isotopes mentioned above [68]. Traces of Be, B and Al were also estimated as fission fragments of nickel, however, they were not displayed since their percentage is lower than 0.1%. it was noticed that about 90% of the fission fragments of both nickel and palladium were stable or semi-stable elements, while the remaining percentage (not displayed) was constituted by unstable fragments. The figures showed a larger variety of significant elements coming from nickel and palladium fission; interesting were also the predictions related to the iron. In further works, it might be worth comparing such predictions, reported in Table 14, to the compositional variations on the surfaces of the electrodes, recently observed by the author and Carpinteri *et al*. studying hydrogen embrittlement effects on Pd electrodes used in experiments of electrolysis [60].

Elements such as titanium and silicon seemed to have a particular relevance in the fission prediction of nickel. Analogously, titanium, chromium, copper and nickel seemed relevant in the palladium fission prediction. Interesting compositional changes involving titanium, chromium, copper and nickel were also observed by the author, Prof. Carpinteri and his research team in experimental campaigns of which results were presented in international conferences [59] [60].

Conclusions

6 FINAL REMARKS AND CONCLUSIONS

For what concerns the experimental campaign with the cobalt-chromium cathode and nickel-iron anode, the results were very interesting. First of all, considering the energy emission, NE up to one order of magnitude higher than the background level was detected. Different peaks were measured throughout the electrolysis process, 200, 650, 1200 and 1500 minutes after the beginning of the experiment. The alpha particle emission level during the electrolysis was twice the background level measured in the laboratory environment before the experiment. The results of the EDX measures conducted in three consecutive phases, before, during and at the end of the experiment, showed interesting variations of the chemical composition of the electrodes. The most interesting feature regarding the Ni-Fe electrode was that the decrease of the average Ni concentration (-8.6%) was comparable to the sum of the variations in Si (+3.9%) and Mg (+4.7%). Such variations appeared to be connected to the hypothesis of reactions 3.1 and 3.2. With regards of the Co-Cr cathode, the decrease in Fe (-3.2%) was comparable to the increase in Cr (+3.0%). A plausible contribution to such variation might come from reaction 3.3. However, the influence of the electrolytic process might be accounted also when considering chemical variations related to the concentration of K.

Considering the second experimental campaign related to the use of nickel-titanium alloy anode and palladium cathode, analogous remarkable results were found. The NE monitored throughout the electrolysis process showed two notable peaks 545 and 1200 minutes after the beginning of the process. The composition analyses conducted showed remarkable variations on the surfaces of both electrodes occurred during the electrochemical processes. A process starting from Palladium non-symmetric fission and implying different piezonuclear reactions was revealed. This appeared to provide a plausible explanation to most of the changes of the composition of the electrodes. In particular, it was possible to explain the appearance of concentrations of elements such as Fe (+2.0%), O (+18.5%), Mg (+1.0%), Si (+1.1%), Al (+0.4%) and Ca (+0.2%) through three conceptual steps considering the depletion of Pd concentration measured (-28.6%)

on the Palladium electrode.

Among all the experimental results, the detection of NE peaks during the process of electrolysis and the micro-cracks identified on the surface of the electrodes after such process caught the interest of the experimentalists. As mentioned in the introduction to this work, they represent common features of an important connection between the crushing tests conducted on solid materials by Carpinteri et al., the experiments of electrochemistry carried out through the research of this thesis and also the data collected concerning the evolution of the composition of the Earth's crust.

The results reported in this thesis showed that specific and non-ordinary nuclear reactions may occur in the condensed matter triggered by phenomena such as the formation and propagation of fractures. Immersed in a liquid solution, the metal surface of electrodes is exposed to the formation of gaseous hydrogen due the decomposition of water molecules caused by the current passage (electrolysis). The high current density favors the formation and penetration of hydrogen into the metal cracks. The presence of hydrogen in the host matrix of the metal is imputed to favor the crack propagation according to the hydrogen embrittlement effect. Hence, a way to explain the nuclear evidence is to consider the fracture as a trigger for piezonuclear reactions causing neutron emission and isotopic changes.

It is true that the full comprehension of the mechanisms is yet to be achieved. However, the approach investigated in collaboration with Professor Cook of the Kansai University (Osaka, Japan) proved to be of great support to the research. The lattice model simulating the rupture of the atomic nucleus through specific planes provided useful insights and data. Numerical simulations on Fe, Ni and Pd showed that it is possible to get fission fragments corresponding to elements involved in the interpretation of both the Earth's crust compositional evolution and the electrolysis experimental results showed in the previous chapters. Therefore, the model is consistent with the mechanical explanation to the nuclear effects investigated in this thesis.

Further research needs to be undertaken, though. For instance, a dynamic analysis could be added to the model in order to investigate how acoustic emission sources, generated by micro and macro-cracks, affect the nuclear structure and lead to acoustic resonance effects.
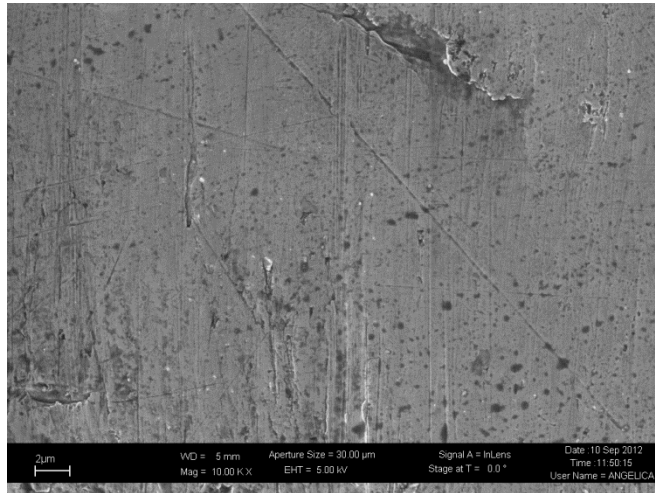
7 APPENDIX

Figure 62 Surface of the Co-Cr electrode (cathode) before electrolysis.
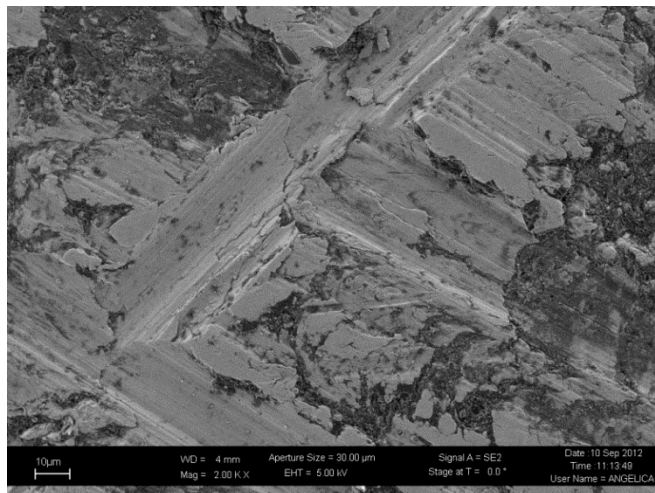
Figure 63 Surface of the Ni-Fe electrode before electrolysis.
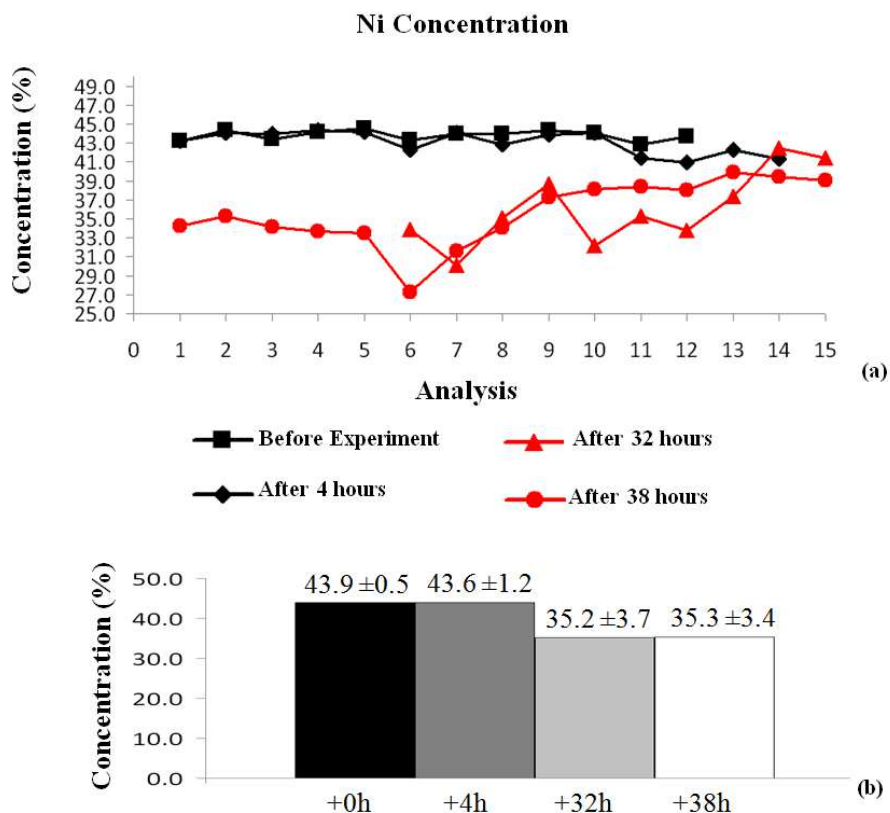
Figure 64 Series of measures of Ni concentration on Ni-Fe electrode.

In Figure 64, details of the EDX composition analyses are reported. Four series of fifteen measures each corresponding to the four steps of measurement are displayed in the top figure (a). The values are expressed in percent mass concentration. Average mass concentration percentages are shown in the bottom figure (b).
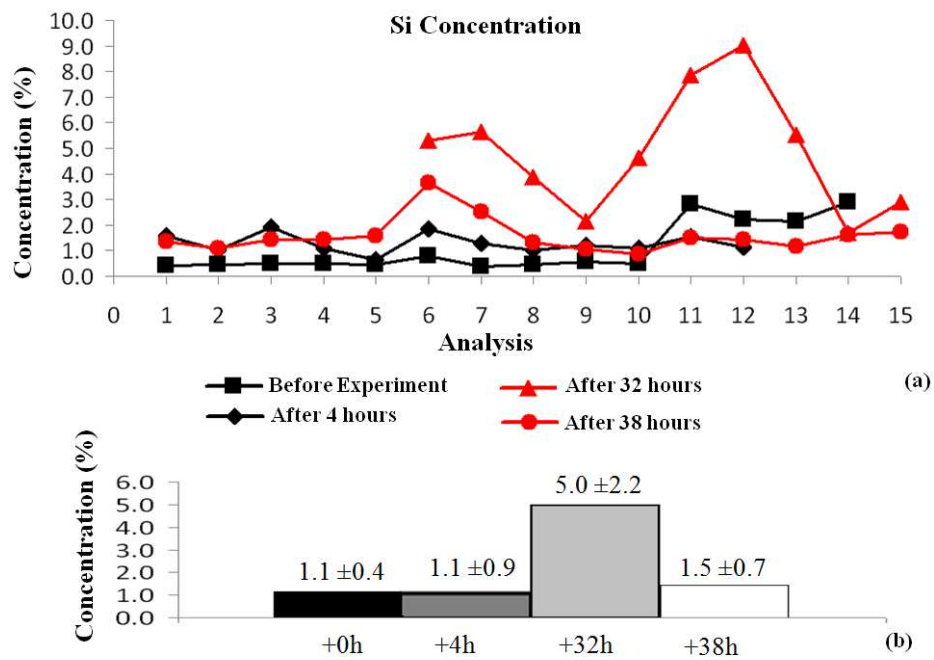
Figure 65 Series of measures of Si concentration Ni-Fe electrode.

Figure 65 shows in the top graph (a) four series of compositional measures corresponding to different stages of the electrolysis experiment. Relevant average mass concentration percentages are displayed in the bottom figure (b).
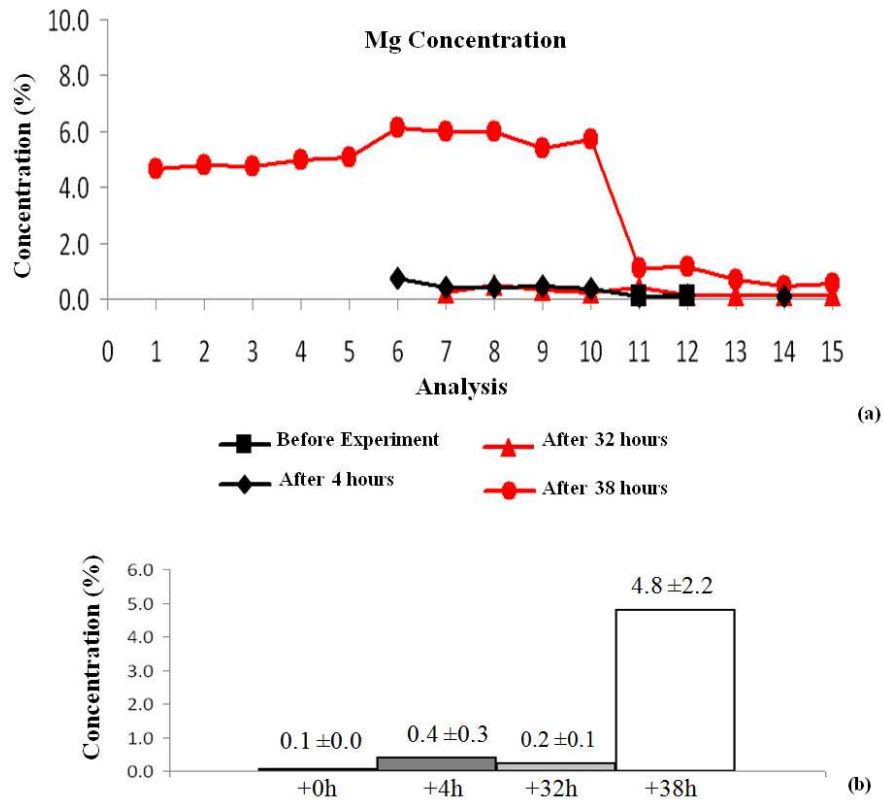
Figure 66 Series of measures of the Mg concentration on the Ni-Fe electrode.

Figure 66 illustrates details of local spots measurement of Mg concentration at different stages of the experiments associated with their average mass concentration percentages shown in the bottom graph (b).
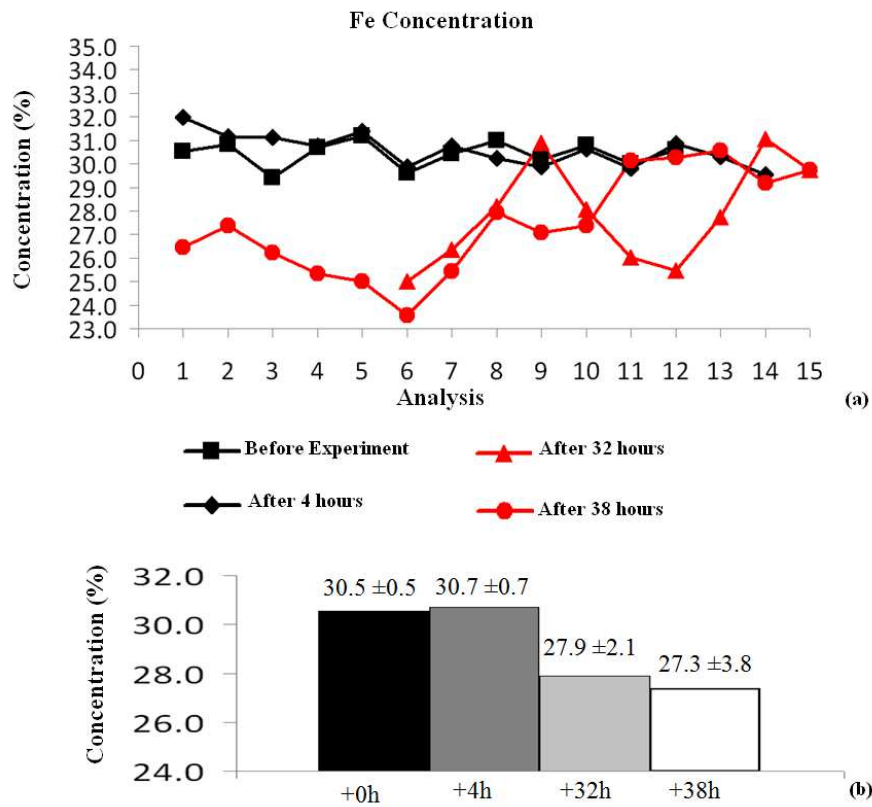
Figure 67 Series of measures of the Fe concentration on Ni-Fe electrode.

In Figure 67, details of the evolution of Fe concentration on the Ni-Fe anode at different stages of the experimental campaign are illustrated in the top graphs. Relative average mass concentration percentages are shown in bottom figure (b).
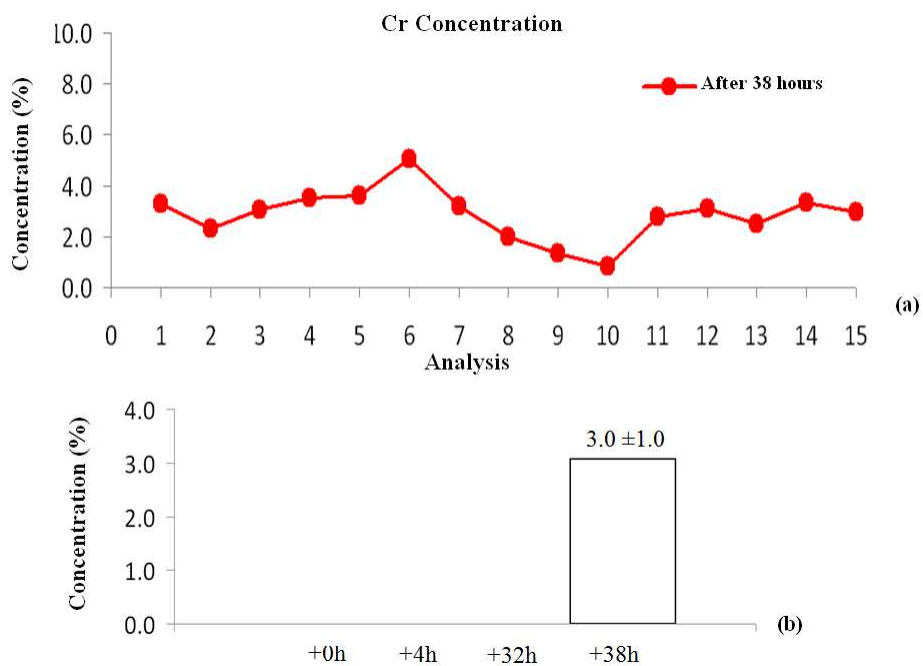
Figure 68 Series of measures of Cr concentration on the Ni-Fe electrode.

Figure 68 illustrates the series of measures of Cr concentration in localized spots across the surface of the Ni-Fe anode. Details show that only the last session of measures at the end of the electrolysis revealed the presence of chromium on the anode.
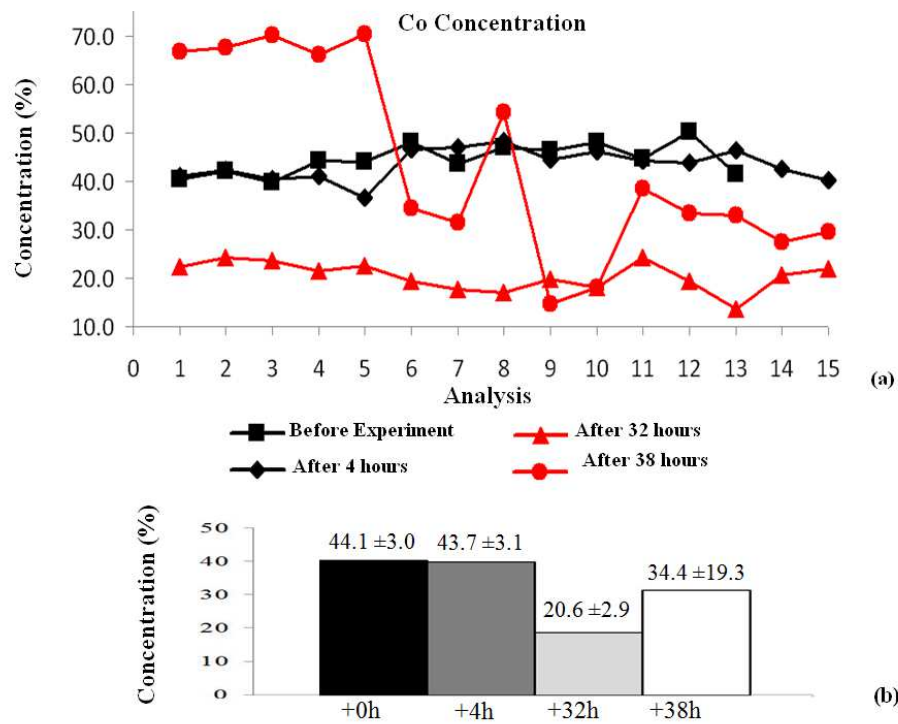
Figure 69 Series of measures of Co concentration in the Co-Cr electrode.

Detailed EDX measures of Co concentration taken over the surface of the cathode were elaborated as displayed in Figure 69. Series of fifteen points corresponding to concentration at different stages of the experiment are reported in figures: before the experiment, after 4, after 32 and 38 hours of electrolysis. The average value of Co concentration changes from a mass percentage of 44.1% at the beginning of the experiment to 20.6% and 34.4% after 32 and 38 hours respectively.
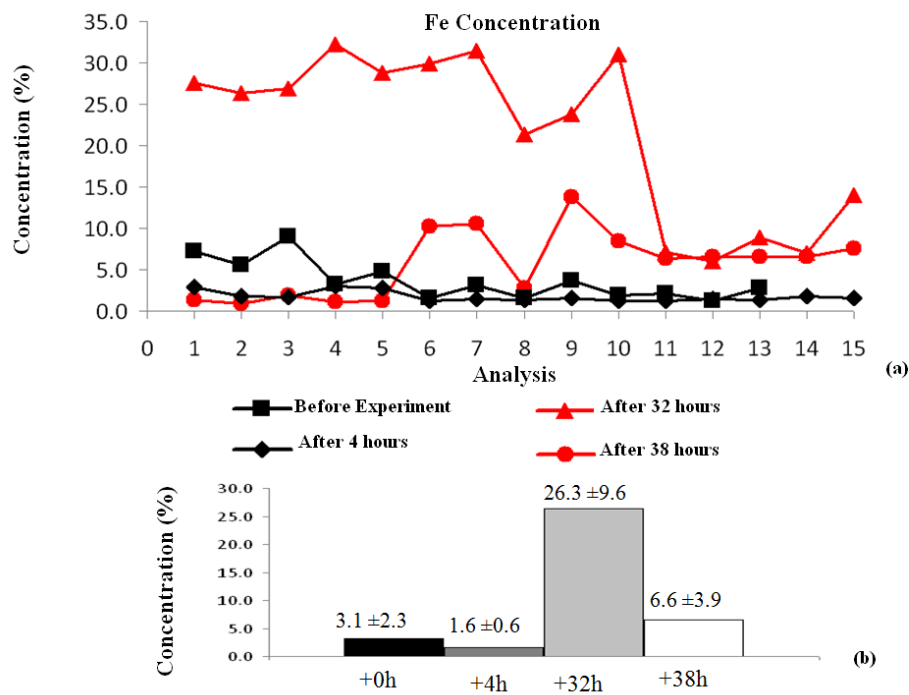
Figure 70 Series of measures of the Fe concentration in the Co-Cr electrode.

In Figure 70, detailed EDX measures of Fe concentration are displayed. They refer to conditions of the Co-Cr cathode before the experiment, after 4, 32 and 38 hours. The average value of Fe concentration changes from a mass percentage of 3.1% at the beginning of the experiment to 26.3% and 6.6% after 32 and 38 hours respectively.
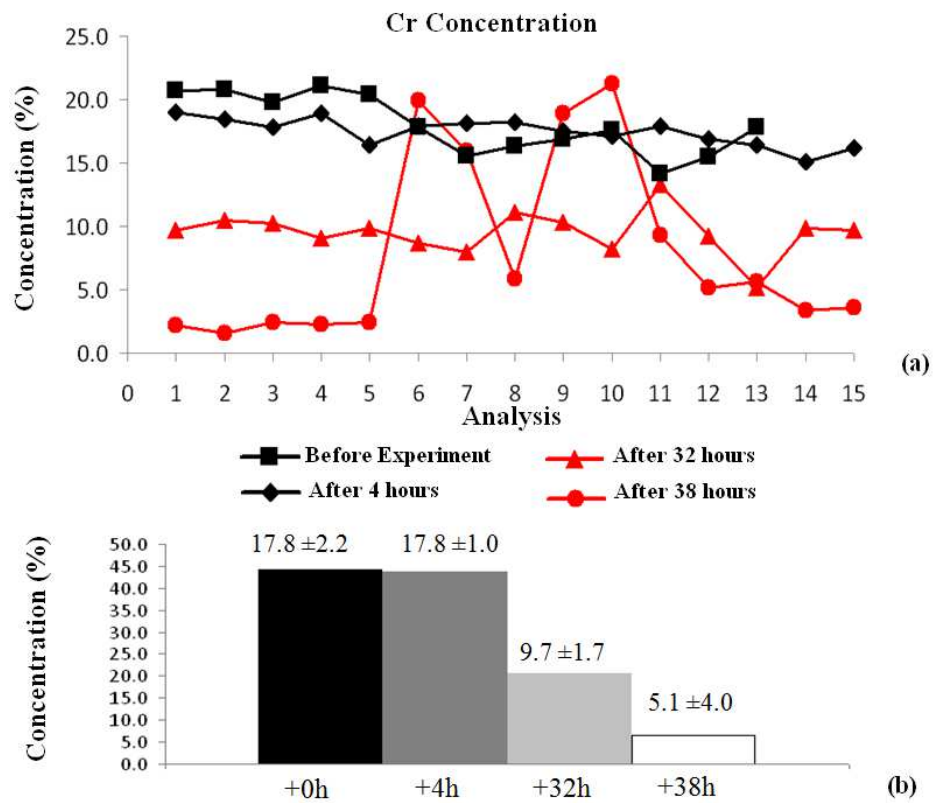
Figure 71 Series of measures of the Cr concentration in the Co-Cr electrode.

Detailed EDX measures of Cr local concentration and its evolution are displayed in Figure 71; they refer to conditions of the Co-Cr cathode before the experiment, after 4, 32 and 38 hours. The average Cr concentration changes from a mass percentage of 17.8% to 9.7% and 5.1% after 32 and 38 h.
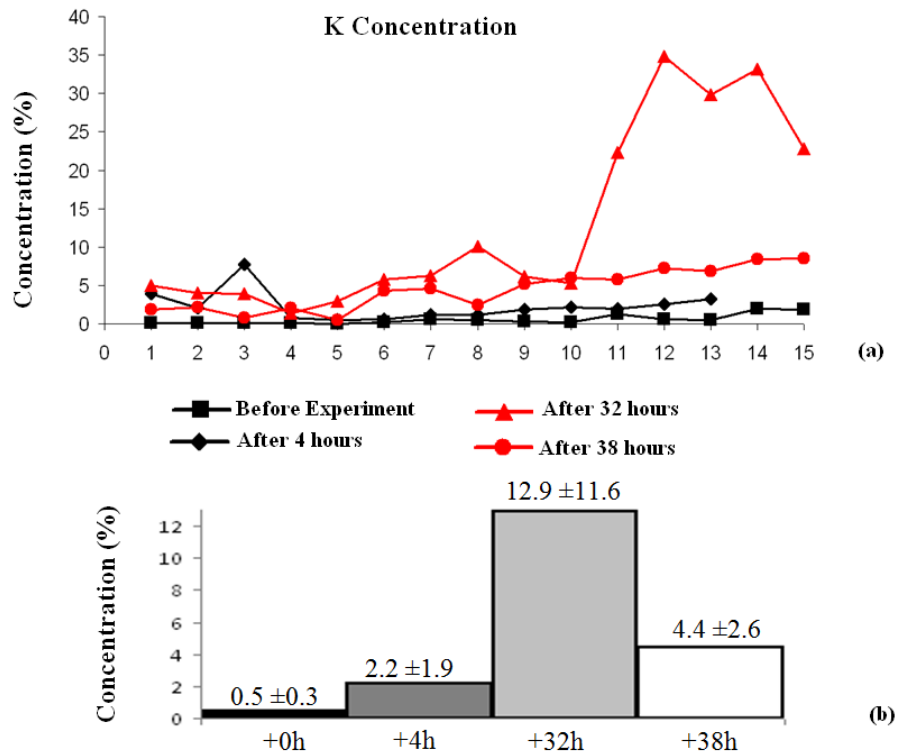
Figure 72 Series of measures of the K concentration in the Co-Cr electrode.

Figure 72 displays the evolution of different series of measures of K concentration on the cathode. They correspond to different stages of the electrolytic experiment: before the experiment, after 4, 32 and 38 hours. The average K concentration changes from 0.5% and 2.2% after 4 hours to 12.9% and 4.4% after 32 and 38 h.

In Table 15, the summary of elaboration of fission simulations is listed. The data concern simulations conducted on piezonuclear reactions. Details of the characteristics of fission fragments predicted by the QND software are also described. The neutron emission column represents the sum of the neutrons released from both fragments derived from each fission plane.

Table 15 Characteristics of fission fragments resulting from QND simulations.

Reaction	Plane	Fragment 1 Z	N	A	Isotope	Decay Time[1]	Fragment 2 Z	N	A	Isotope	Decay Time	Neutron Emission	Fission Probability [%]
(1)[2]	2	13	14	27	Al^{27}	Stable	13	16	29	Al^{27}	6.6 [m]	+2n	23.22
	8	13	14	27	Al^{27}	Stable	13	16	29	Al^{27}	6.6 [m]	+2n	
(2)[2]	14	12	12	24	Mg^{24}	Stable	14	18	32	Si^{28}	172[y]	+4n	40.74
	16	12	12	24	Mg^{24}	Stable	14	18	32	Si^{28}	172[y]	+4n	
(3)[2]	1	6	7	13	C^{12}	Stable	20	23	43	Ca^{40}	Stable	+4n	36.04
	3	20	22	42	Ca^{40}	Stable	6	8	14	C^{12}	5730[y]	+4n	
(4)	2	13	14	27	Al^{27}	Stable	14	18	32	Si^{28}	172 [y]	+4n	100
	8	14	16	30	Si^{28}	Stable	13	16	29	Al^{27}	6.6 [m]	+4n	
(5)[2]	2	14	16	30	Si^{28}	Stable	14	15	29	Si^{28}	Stable	+3n	32.60
(6)[2]	12	11	13	24	Na^{23}	14.95[h]	17	18	35	Cl^{35}	Stable	+n	67.40
(7)[2]	2	6	6	12	C^{12}	Stable	6	6	12	C^{12}	Stable		11.26
(8)[1]	9	11	12	23	Na^{23}	Stable	1	0	1	H^{1}	Stable		31.01
(9)[2]	4	8	12	20	O^{16}	13.5[s]	4	0	4	$4H^{1}$	Stable	+4n	
	6	0	4	4			12	8	20	$O^{16}+4H^{1}$	0.1[s]	+4n	57.73
	7	4	4	8	$4H^{1}$	0.07[fs]	8	8	16	O^{16}	Stable	+4n	
	8	8	9	17	O^{16}	Stable	4	3	7	$4H^{1}$	0.07[fs]	+4n	
(10)[2]	1	2	2	4	He^{4}	Stable	18	18	36	$3C^{12}$	Stable		10.28
(11)[2]	1	1	0	1	H^{1}	Stable	19	20	39	K^{39}	Stable		58.46
(12)	1	4	4	8	$4H^{1}$	0.07[fs]	16	16	32	$2O^{16}$	Stable	+4n	
	3	16	16	32	$2O^{16}$	Stable	4	4	8	$4H^{1}$	0.07[fs]	+4n	31.26
	7	4	4	8	$4H^{1}$	0.07[fs]	16	16	32	$2O^{16}$	Stable	+4n	
	9	16	16	32	$2O^{16}$	Stable	4	4	8	$4H^{1}$	0.07[fs]	+4n	

[1] Decay time of the isotope (half life): zepto-seconds, 10^{-21} (zs); femto-seconds, 10^{-15} (fs); seconds (s); minutes (m); hours (h); days (d); years (y)
[2] Picking Option

BIBLIOGRAPHY

[1]   A. Carpinteri, F. Cardone e G. Lacidogna, «Piezonuclear neutrons from brittle fracture: early results of mechanical compression tests,» *Strain,* vol. 45, pp. 332-339, 2009.

[2]   A. Carpinteri, Meccanica dei Materiali e della Frattura, Bologna: Pitagora, 1992.

[3]   D. Halliday, R. Resnik e K. Krane, Physics Volume 1 and Volume 2, New York: John Wiley & Sons Inc., 2004.

[4]   H. Liebowitz, Fracture an advanced treatise, London: Academic Press New York, San Francisco, 1971.

[5]   J. Petit e P. Scott, «Volume 6, Environmentally-assisted fracture, Chapter 6.02,» in *Comprehensive Structural Integrity: fracture of materials from nano to macro*, Elsevier, 2003.

[6]   R. Jones e S. Bruemmer, «Environment induced crack growth processes in nicle-based alloys,» in *First international conference on Environment- Induced Cracking of Metals*, Kohler, Wisconsin, USA, 1990.

[7]   P. Hicks e C. Altstetter, «Hydrogen-enhanced cracking of superalloys,» *Metall Trans. A, 23,* pp. 237-249, 1992.

[8]   N. Moody, M. Perra e S. Robinson, «Hydrogen pressure and crack tip stress effects on slow crack growth thresholds in an iron-based superalloy,» *Scripta Metallurgica 22,* pp. 1261-1266, 1988.

[9]   D. M. Symons, «A comparison of internal hydrogen embrittlement and hydrogen environment embrittlement of X-750,» *Engineering Fracture Mechanics 68,* pp. 751-771, 2001.

[10]   G. Pressouyre, «A classification of hydrogen traps in steel,» *Metall. Trans. A 10,* pp. 1571-1573, 1979.

[11]   J. Hirth, «Effects of hydrogen on the properties of iron and steel,»

Metall. Trans. A 11, pp. 861-890, 1980.

[12]   P. Tyler, M. Levy e L. Raymond, «Investigation of the conditions for crack propagation and arrest under cathode polarization by rising step load bend testing,» *Corrosion 47,* pp. 82-87, 1991.

[13]   F. Cardone, A. Carpinteri e G. Lacidogna, «Piezonuclear neutrons from fracturing of inert solids,» *Physics Letters A 373,* pp. 4158-4163, 2009.

[14]   A. Carpinteri, F. Cardone e G. Lacidogna, «Energy emissions from failure phenomena: mechanical, electromagnetic, nuclear,» *Experimental Mechanics 50,* pp. 1235-1243, 2010.

[15]   A. Manuello Bertetto, Tesi di dottorato di ricerca in Ingengeria delle strutture: Acoustic Emission Characterization of Critical Phenomena in Damaged Structures, Torino: Politecnico di Torino, 2007.

[16]   A. Carpinteri, G. Lacidogna e N. Pugno, «Time-scale effects during damage evolution: a fractal approach based on acoustic emission,» *Strength, Fracture and Complexity 3,* pp. 127-135, 2005.

[17]   A. Carpinteri, G. Lacidogna e N. Pugno, «Structural damage diagnosis and life-time assessment by acoustic emission monitoring,» *Engineering Fracture Mechanics 74,* pp. 273-286, 2007.

[18]   A. Carpinteri, «Cusp catastrophe interpretation of fracture instability,» *J. Mech Phys Solids,* vol. 37, pp. 567-582, 1989.

[19]   A. Carpinteri, «A catastrophe theory approach to fracture mechanics,» *Int J Fract,* vol. 44, pp. 57-69, 1990.

[20]   F. Cardone, G. Cherubini e A. Petrucci, «Piezonuclear neutrons,» *Phys Lett A,* vol. 373, pp. 862-866, 2009.

[21]   A. Carpinteri, G. Lacidogna, A. Manuello e O. Borla, «Energy emissions from brittle fracture: Neutron measurements and geological evidences of piezonuclear reactions,» *Strength, Fracture and Complexity,* vol. 7, pp. 13-31, 2011.

[22]   Bubble Technology Industries, Instruction manual for Bubble detector,

Chalk River, Ontario, Canada, 1992.

[23]   «NCRP Report 38,» National Council on Radiation Protection and
         Measurements Protection Against Neutron Radiation, 1971.

[24]   A. Carpinteri, G. Lacidogna, A. Manuello e O. Borla, «Piezonuclear
         fission reactions from earthquakes and brittle rocks failure: evience
         of neutron emission and nonradioactive product elements,»
         Experimental Mechanics, vol. 53, n. 3, pp. 345-365, 2013.

[25]   A. Carpinteri e M. Corrado, «An extended (fractal) overlapping crack
         model to describe crushing size-scale effects in compression,» *Eng.
         Failure Analysis,* vol. 16, pp. 2530-2540, 2009.

[26]   A. Carpinteri, A. Chiodoni e S. R. Manuello A, «Compositional and
         Microchemical Evidence of Piezonuclear Fission Reactions in Rock
         Specimens Subjected to Compression Tests,» *Strain,* vol. 47, n.
         Supplement s2, pp. 282-292, 2011.

[27]   A. Carpinteri e A. Manuello, «Geochemical and Geomechanical
         Evidence of Piezonuclear Fission Reactions in the Earth's Crust,»
         Strain, vol. 47, n. Supplement s2, pp. 267-281, 2011.

[28]   L. Negri, Tesi di laurea magistrale in Ingegneria delle strutture:
         L'emissione di energia dalla frattura fragile: reazioni nucleari
         anomale e implicazioni in geologia e astronomia, Torino:
         Politecnico di Torino, 2012.

[29]   A. Carpinteri, G. Lacidogna, A. Manuello e O. Borla, «Piezonuclear
         Fission Reactions in Rocks: Evidences from Microchemical
         Analysis, Neutron Emission, and Geological Transformation,» *Rock
         Mechanics and Rock Engineering,* vol. 45, n. 4, pp. 445-459, 2012.

[30]   C. J. Hawkesworth e A. I. S. Kemp, «Evolution of the continental
         crust,» *Nature ,* vol. 443, pp. 811-817, 2006.

[31]   A. A. Yaroshevsky, «Abundances of chemical elements in the Earth's
         crust,» *Geochem. Int.,* vol. 44, pp. 54-62, 2006.

[32]   A. Carpinteri e A. Manuello, «An indirect evidence of piezonuclear
         fission reactions: Geomechanical and geochemical evolution in the

Earth's crust,» *Physical Mesomechanics,* vol. 15, pp. 37-46, 2012.

[33] M. Knapmeyer, J. Oberst, E. Hauber, M. Waehlisch, C. Deuchler e R. Wagner, «Working Models for Spatial Distribution and Level of Mars' Seismicity,» *Journal of Geophysical Research,* vol. 111, 2006.

[34] W. Boynton, G. Taylor, L. Evans, R. reedy, R. Starr, D. Janes, K. Kerry, D. Drake, K. Kim, R. Williams, M. Crombie, J. Dohm, V. Baker, A. Metzger, S. Karunatillake, J. Keller, H. Newsome, J. Arnold e e. al, «Concentration of H, Si, Cl, K, Fe and Th in the low- and mid-latitude regions of Mars,» *Journal of Geophysical Research,* vol. 112, 2007.

[35] I. Mitrofanov, D. Anfimov, A. Kozyrev, M. Litvak, A. Sanin, V. Tret'yakov, A. Krylov, V. Shvetsov, W. Boynton, C. Shinohara, D. Hamara e R. Saunders, «Maps of Subsurface Hydrogen from the High Energy Neutron Detector, Mars Odyssey,» *Science,* vol. 297, pp. 78-81, 2002.

[36] E. Storms, The Science of low enegy nuclear reaction. A Comprehensive Compilation of Evidence and Explanations about Cold Fucion, Singapore: World Scientific Publishing Co. Pte. Ltd., 2007.

[37] M. Fleischmann e S. Pons, «Electrochemically induced nuclear fusion of deuterium,» *Journal of Electroanalytical Chemistry. Vol. 263,* p. 301, 1989.

[38] R. Germano, FUSIONE FREDDA Moderna storia d'inquisizione e alchimia, Napoli: Bibliopolis, edizioni di filosofia e scienze, 2003.

[39] K. S. Krane, Introductory Nuclear Physics, Wiley, 1987.

[40] S. Kaliski, «Critical masses of miniexplosion in fission-fusion hybrid systems,» *Journal of Technical Physics,* vol. 17, pp. 99-108, 1976.

[41] S. Kaliski, «Bi-conical system of concentric explosive compression of D-T,» *Journal of Technical Physics,* vol. 19, pp. 283-289, 1978.

[42] F. Winterberg, «Autocatalytic fusion-fission implosions,» *Atomenergie*

Kerntechnik, vol. 44, p. 146, 1984.

[43]   Y. Arata e Y. Ahang, «Achievement of Solid-State Plasma Fusion (Cold Fusion),» *Proc. Jpn. Acad.,* vol. 71, n. Ser. B, pp. 304-309, 1995.

[44]   Y. Arata, H. Fujita e Y. Zhang, «Intense deuterium nuclear fusion of pycnodeuterium-lumps coagulated locally within highly deuterated atom clusters,» *Pro. Jpn. Acad.,* vol. 78, n. Ser. B, p. 201, 2002.

[45]   R. P. Taleyarkhan, C. D. West, J. S. Cho, R. T. Lathey Jr, R. I. Nigmatulin e R. C. Block, «Evidence for Nuclear Emissions During Acoustic Cavitation,» *Science,* vol. 295, p. 1868, 2002.

[46]   T. Mizuno, T. Ohmori e E. Michio, «Isotopic changes of the reaction products induced by cathodic electrolysis in Pd,» *J. New Energy,* vol. 1, p. 31, 1996.

[47]   T. Mizuno, Nuclear Transmutation: The Reality of Cold Fusion, Infinite Energy Press, 1998.

[48]   T. Mizuno, D. Y. Chung, F. Sesftel e Y. Aoki, «Generation of Heat and Products During Plasma Electrolysis,» in *Eleventh International Conference on Condensed Matter Nuclear Science*, Marseille, France, 2004.

[49]   P. Kanarev e T. Mizuno, «Cold Fusion by Plasma Electrolysis of Water,» 2002. [Online]. Available: http://guns.connect.fi/innoplaza/energy/story/Kanarev/coldfusion/.

[50]   P. A. Mosier-Boss, S. Szpak, F. E. Gordon e L. P. G. Forsley, «Use of CR-39 in Pd/D co-deposition experiments,» *Eur. Phys. J. Appl. Phys.,* vol. 40, pp. 293-303, 2007.

[51]   P. A. Mosier-Boss, J. Y. Dea, L. P. G. Forsley, M. S. Morey, J. P. Tinsley, J. P. Hurley e F. E. Gordon, «Comparizon of Pd/D co-deposition and DT neutron generated triple tracks observed in CR-39 detectors,» *Eur. Phys. J. Appl. Phys.,* vol. 51, p. 20901, 2010.

[52]   D. Veneziano, O. Borla, A. Goi, A. Manuello e A. Carpinteri, «Mechanical conjectures based on hydrogen embrittlement

explaining cold nuclear fusion,» in *Congresso Nazionale di Meccanica Teorica ed Applicata (AIMETA)*, Torino, 2013.

[53]   C. D. W. Van Siclen e S. E. Jones, «Piezonuclear fusion in isotopic hydrogen molecules,» *J. Phys. G: Nucl. Phys.,* vol. 12, pp. 213-221, 1986.

[54]   G. Preparata, «Fractofusion revisited,» in *AIP Proceedings*, Provo, Utah (USA), 1990.

[55]   E. Storms, «Cold Fusion from a Chemist's point of View,» 2013. [Online]. Available: http://lenr-canr.org/acrobat/StormsEcoldfusionf.pdf.

[56]   A. Widom, J. Swain e Y. N. Srivastava, «Photo-Disintegration of the Iron Nucleus in Fractured Magnetite ROcks with Magnetostriction,» arXiv:1306.6286, 2013.

[57]   A. Widom, J. Swain e Y. N. Srivastava, «Neutron production from the fracture of piezoelectric rocks,» *J. Phys. G: Nucl. Part. Phys.,* vol. 40, 2013.

[58]   N. D. Cook, Models of the Atomic Nucleus: Unification Through a Lattice of Nucleons, Springer, 2010.

[59]   A. Carpinteri, O. Borla, A. Goi, A. Manuello e D. Veneziano, «Mechanical conjectures explaining cold nuclear fusion,» in *Conference and Exposition on Experimental and Applied Mechanics (SEM)*, Lombard, Illinois, USA, 2013.

[60]   A. Carpinteri, O. Borla, A. Goi, A. Manuello e D. Veneziano, «Hydrogen embrittlement and "cold fusion" effects in palladium during electrolysis experiments,» in *Conference & Exposition on Experimental and Applied Mechanics (SEM)*, Greenville, South Carolina, USA, 2014.

[61]   «AUTOMESS Automation und Messtechnik GMBH,» 2015. [Online]. Available: http://www.automess.de/Download/Prospekt_AD17k_E.pdf.

[62]   N. D. Cook, «A unified theory of atomic and nuclear shell structure,»

Experientia, vol. 34, pp. 419-552, 1978.

[63] N. D. Cook e V. Dallacasa, «Face-centered-cubic solid-phase theory of the nucleus,» *Physical Review C,* 1987.

[64] E. Feenberg e E. Wigner, «On the Structure of the Nuclei Between Helium and Oxygen,» *Physical Review,* vol. 51, 1937.

[65] E. Wigner, «On the consequence of the Symmetry of the Nuclear Hamiltonian on the Spectroscopy of Nuclei,» *Physical Review,* vol. 51, p. 106, 1937.

[66] N. D. Cook, «Toward an Explanation of Transmutation Products on Palladium Cathodes,» in *14th International conference on Condensed Matter Nuclear Science*, Washington DC, 2008.

[67] N. D. Cook, «Simulation of the Nuclear Transmutation Effects in LENR,» in *18th International Conference on cold fusion*, Columbia, MO, USA, 2013.

[68] «Interactive Chart of Nuclides,» National Nuclear Data Center, Brookhaven National Laboratory, [Online]. Available: http://www.nndc.bnl.gov/chart/.

[69] E. Storms, «A Student's Guide to Cold Fusion,» 2012. [Online]. Available: http://lenr-canr.org/acrobat/StormsEastudentsg.pdf.